A Numerical Study On The Origin Of Cluster Magnetic Fields

Julius Donnert

November 8, 2007

Contents

List of Tables

1 Introduction

Galaxy clusters are the largest virialized structures in the universe, measuring 10th of millions of lightyears in size. They are formed by the non-linear process of structure formation, when all matter clumps to form a web like structure with clusters at its junctions. Naturally these objects are subject to research for cosmologists, who are interested in the universe properties. There is a wealth of observations covering a wide range of wavelengths. Optical surveys show clusters containing thousands of galaxies moving in their gravitational potential. X-Ray satellites find gas at the bottom of the potential. It consists mostly of Hydrogen and Helium, the lightest elements, forming a plasma of a temperature of millions of Kelvin. Radio telescopes observe, that some clusters show diffuse, non thermal emission in cm wavelengths. The underlying physical models suggest, that the source of radiation is a population of relativistic particles, moving on spiral trajectories in a magnetic field.

Although the origin of galaxy clusters is well understood, the formation of their inherent magnetic fields is unclear. In this work we investigate, if outflows from the first galaxies can provide sufficient field strength, so structure formation is able to amplify the field to observed values. We use computer simulations to follow structure formation from early times up to today. Our tree/SPH code GADGET-2 uses ideal magnetohydrodynamics to follow the magnetic field evolution troughout structure formation, starting at redshift 10. Unfortunately up to today it is not possible to selfconsistently simulate galactic outflows, cooling and magnetic fields. We therefore use a semianalytic model for galactic outflows.

At redshift 6 the universe contains a large population of small (dwarf) galaxies. During the formation of the cosmic web, galaxy mergers lead to gravitational interaction between those galaxies.Tidal forces similar to those a giant planet like jupiter imposes on a close moon, lead to elevated star formation in molecular clouds, called a starburst. The universe after reionisation at $z \approx 10$ is therefore populated by large number of starbursting, small galaxies. Their star forming activity triggers a high number of stellar explosions from short living stars, called supernovas. These explosions eject vast amounts of magnetised plasma isotropically into the interstellar medium.
If a starburst in the early universe is strong enough to overcome the galaxies potential, the large number of supernova ejecta can form a galaxy wide superbubble, moving away from its center. This superwind can overcome the potential wall of the dwarf galaxy and pollutes the intergalactic medium with metals and magnetic field. Hydrodynamic effects

like shear flows in these winds amplify the field in addition to the adiabatic compression and magnetohydrodynamic amplification induced by structure formation.

Our model estimates the size and energy of these winds, based on properties of the host galaxy and its halo. Assuming a certain structer, we seed (=implant) a magnetic field once in every small halo at a redshift of about $z = 4.1$. After that, the simulation is restarted and evolved up to today. The results allow us to test seed models for magnetic fields in clusters of galaxies, by comparing their evolved fields with observations. The following questions arise:

- Can the evolved field strength from galactic seeds compare with observations in clusters ? I.e. can galactic outflows seed enough fields, to match observations of strength and correlation length ?
- Can a prediction be made for fields in voids and filaments, where observations are unclear at the moment ?

For a constant cosmological seed field this was done successfully by [DGST05]. Their results show that seed field of $B_0 = 0.2 \cdot 10^{-11}$ G produces cluster fields, which compare well with rotation measurement and radio halo observations.

1.1 Abstract

blabla

1.2 Überblick

1.3 Acknowledgements

2 Basics

2.1 Cosmology

With the term Cosmology, we mean the part of physics, that describes global properties of the universe. As of the size of the examined object, cosmologists are interested in structures above scales of galaxies and look at properties on scales of clusters of galaxies or Mpc. The dominating force on cosmological scales is gravitation, acting on the fluid like matter content. Section 2.1.1 deals with the general relativistic model that describes the time evolution of the universe. The observations that lead to todays cosmological paradigm, the λCDM model[1], are described in the second section 2.1.2. They observe an expanding universe, that is homogeneous and isotropic on the largest scales. It's visible content is made mostly of hydrogen and helium in stars and gas, while discrepancies between models and observations suggest that in fact most matter is invisible. Other observations suggest a dark energy, that accelerates the expansion of the universe. We will briefly describe how observed rotation curves of galaxies, galaxy cluster temperature and mass, type SN1a supernovas etc lead to the concepts of dark matter and dark energy. They form the backbone of the λCDM model.
Parts 2.2 and 2.5 scetch out the two basic physical theories used later in our simulations: Newtonian gravity and Magnetohydrodynamics. The former one describes the evolution of dark matter and baryons well enough for our simulations. The latter one affects only Baryons and is far more complicated.
We close with a description of the current picture on magnetic fields in the universe on scale of galaxies and above.

2.1.1 Time Evolution Of The Universe

On distances as large as millions of lightyears, the dynamics of large objects is dominated by gravitation. From the four fundamental forces known to physics today, gravity is the weakest, but with the largest range. The most precise theory to handle gravity is General Relativity, where it is described by curvature of the 4 dimensional space-time. Curvature is expressed by a tensor field (the metric $g_{\mu\nu}$) and generated by the energy momentum tensor $T_{\mu\nu}$, which contains for a perfect, isotropic fluid just pressure p as spatial and

[1] All GADGET simulations in the work are based on a the λ CDM model

(energy)density ρ as time component. With $R_{\mu\nu}$ the Ricci tensor of curvature, R the Ricci scalar and G Newtons gravitational constant, the basic equation of GR is :

$$G_{\mu\nu} \equiv R_{\mu\nu} + \frac{R}{2} \cdot g_{\mu\nu} + \Lambda g_{\mu\nu} = 8\pi G \cdot T_{\mu\nu} \tag{2.1}$$

From observations it becomes clear, that the universe is very homogeneous and isotropic on scales of Gpc. A solution of the equations 2.1 under these conditions is the Robertson-Walker Metric :

$$ds^2 = c^2 dt^2 - a^2(t) \left(\frac{dr^2}{1 - kr^2} + r^2 \left(d\theta + \sin^2 \theta d\phi^2 \right) \right) \tag{2.2}$$

with spherical coordinates (r, θ, ϕ), curvature k and expansion factor $a(t)$. Note that it is essentially the metric of an expanding sphere in 4 dimensions (if $k > 0$), where $a(t)$ describes the relative expansion between two times. Often $a(t_0) = 1$ is set for today, so that r becomes dimensional.
Combine 2.1 and 2.2 to obtain the Friedmann equations :

$$\begin{array}{rcl} \frac{\dot{a}}{a} + \frac{k}{a^2} - \frac{\Lambda}{3} & = & \frac{8\pi G}{3}\rho \\ 2\frac{\ddot{a}}{a} + \frac{\dot{a}}{a} - \frac{k}{a^2} - \Lambda & = & -8\pi G p \end{array} \quad \Longleftrightarrow \quad \begin{array}{rcl} \dot{\rho} & = & -3\frac{\dot{a}}{a}(p + \rho) \\ \frac{\ddot{a}}{a} & = & -4\pi G \left(\frac{1}{3}\rho + p \right) + \frac{\Lambda}{3} \end{array} \tag{2.3}$$

where k serves as constant of integration. The density $\rho = \rho_R + \rho_M$ is the summed radiation and matter density. The same is valid for the pressure p, which is connected to the density via the equation of state.

The equations on the right side of 2.3 show:

1. The change in density is solely from expansion of space, this means energy conservation, assuming adiabatic expansion.
2. The decceleration of space is driven by its matter/energy content $\left(-4\pi G \left(\frac{1}{3}\rho + p \right) < 0\right)$
3. The acceleration of space is parametrized by a positive cosmological constant Λ

If we consider the left pair of equations, setting $\Lambda = 0$ and $k = 0$ defines a critical density $\rho_c = \frac{3H_0}{8\pi G}$. Here we set $\frac{\dot{a}}{a} = H$ and $\frac{\dot{a}}{a_0} = H_0$ corresponding to the Hubble law (see 2.1.2, first paragraph). The first Friedmann equation can rewritten in terms of density parameter $\Omega_i = \rho_i \ \rho_{i,c}$ and gaussian curvature $K = k/H_0$:

$$\frac{H^2}{H_0} = \Omega_\Lambda + \Omega_0 - \frac{K}{a^2} \tag{2.4}$$

$$= \Omega_\Lambda + \frac{\Omega_R}{a^4} + \frac{\Omega_M}{a^3} - \frac{K}{a^2} \tag{2.5}$$

Curvature of the universe today ($H = H_0$) is therefore determined by the density parameters of matter and cosmological constant. Figure 2.1 shows the resulting 2 dimensional analogue with a total overdensity Ω_0 with $\Omega_\Lambda = 0$. It determines time evolution of $a(t)$ when solving equations 2.4 for the scale parameter. Assuming $\Lambda = 0$ and $K > 0$ it recollapses and the geometry of space is closed, for $K < 0$ an open universe will expand forever and for $K = 0$ the expansion of flat spacetime slows down and stops at infinity. For a non zero cosmological constant, and flat spacetime, the universe expansion accelerates, as soon as Λ dominates. How mass and cosmological constant determine the geometry and time evolution of space time is shown in 2.3. Newest WMAP data indicates that the universe is flat to high accuracy.

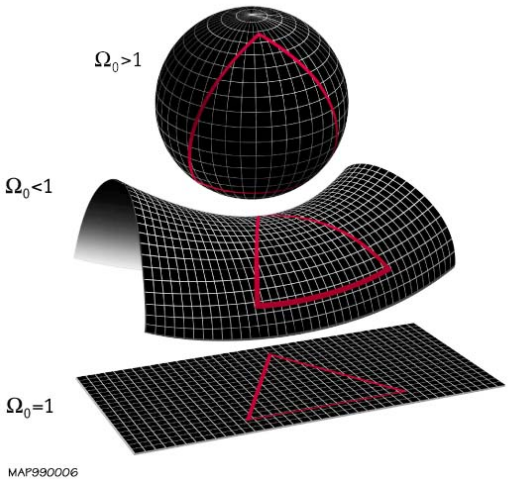

Figure 2.1: Geometry of space is determined by curvature [Wik07b]

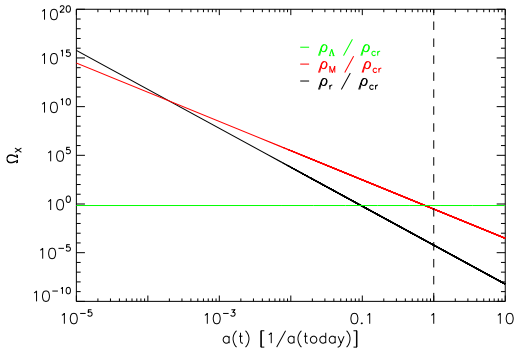

Figure 2.2: Evolution of radiation (black), matter (red) and cosmological constant (green) density over the scale parameter, assuming a cosmological constant

The time evolution of matter and energy is decribed by the equation of state:

$$\rho = a^{-3(1+w)} \tag{2.6}$$

$$w = \frac{p}{\rho} \tag{2.7}$$

where w is call the equation of state paramater. As the thermal speed of matter is much smaller than the sound speed $w_M = 0$. From Bose-Einstein statistics follows $w_r = \frac{1}{3}$ for radiation, and as Dark Energy might be constant over time ($\Lambda(t) = const$), 2.3 can be integrated to show $w_\Lambda = -1$. The contribution to the overall energy density of the universe can be computed by integrating the third equation in 2.3 using the equation of state. We can express the Friedmann equations in terms of matter, radiation and Λ, as done in equation 2.5.

If we plot the contributions of matter, radiation and dark energy to the overall density (figure 2.2), it becomes clear, that at early times, density and therefore gravity was

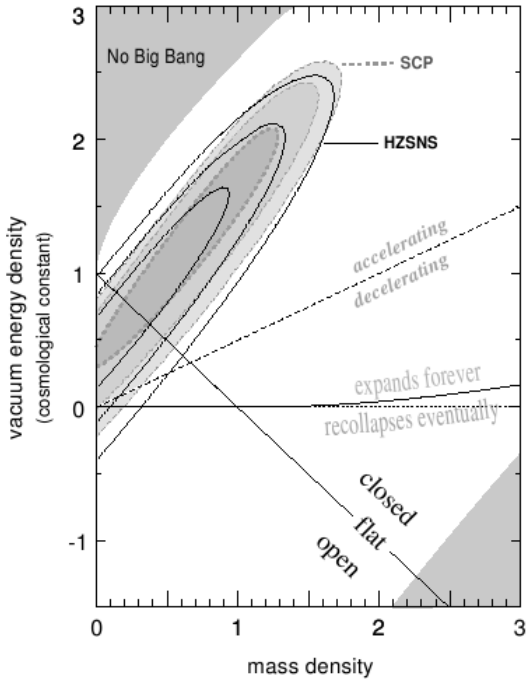

Figure 2.3: Fate of $a(t)$ over Ω_Λ and Ω_M [PS03]

dominated by radiation. At the time/redshift of equality ($1 + z_* = 2.4 \cdot 10^4\,\Omega_\mathrm{m}\mathrm{h}^2$) matter started to determine the universe's evolution. It is important to note, that today dark energy is just about to start dominating.If this was not the case, we were not able to observe it.

The solution to the Friedman equation gives the evolution of the scale factor over time. Figure 2.3 shows, how mass density and a cosmological constant influence the evolution. The conture linies show the constrains of two independent SN1a measurements on Ω_M and Ω_Λ up to a 3σ confidence. Other measurements (CMB) predict a flat universe, so todays picture emerges as an accelerated expansion.

2.1.2 Key Experiments And Their Interpretation

Observations of extragalactic objects detect, that the Milkyway is only one of many galaxies, containing as stars, dust and gas as well. A shift in the spectral lines of galaxies is observed, called the *redshift*. It is defined as :

$$z = \frac{\lambda_{observed} - \lambda_{emitted}}{\lambda_{observed}} \tag{2.8}$$

and can be interpreted as a doppler shift[2], which then corresponds to a receding velocity, with $z \approx \frac{v}{c}$ for low redshifts. Combined with distance measurements like Cepheids variability, SN1a lightcurve calibration and parallax methods a correlation between redshift and distance is found.

The Hubble Diagram illustrates this by plotting velocity of a galaxy over distance. Figure 2.4 shows the original hubble diagram. It leads to the historic definition of the hubble parameter: $c \cdot z = H_0 \cdot d$, todays common value is $H_0 \approx 72$ [SVP+03]. As the relation is independent of direction, it follows, that the universe is expanding isotropically.

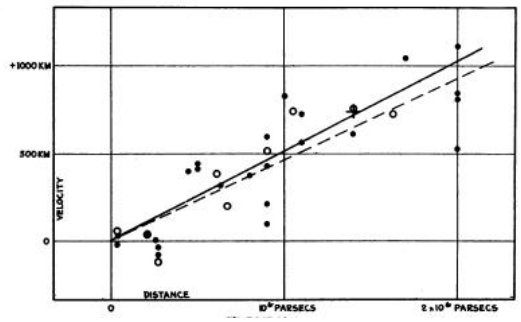

Figure 2.4: The first hubble diagram [Hub29]

The redshift - distance relation is found for every object on cosmological scales, e.g. that is not gravitationally bound to us. In general it is isotropic and nonlinear for large distances, depending on the energy and matter content of the universe.

In modern Hubble Diagrams to redshifts $z > 1$ the distance estimation is done by supernova type 1a lightcurves. Here the calibration is done by an empirical relation between luminocity and the shape of the lightcurve. A naive extrapolation backwards in time, leads to a finite age of the universe and a dense and hot inital state, called the Big Bang. $\frac{1}{H_0}$ gives a rough estimate for the age of the universe, $t_{Universe} \approx 1.3 \cdot 10^{10}\,\mathrm{yr}$.

Element abundances The universe consists mostly of hydrogen and helium, only a small percentage of the baryonic mass is in heavier elements. This is commonly explained by the way baryonic matter is formed. Only light elements (up to Li) are thought to be primordial of origin, i.e. produced by the big bang, while heavier nucleii are formed in stars through burning processes (up to Fe) and by supernovas during phases of high neutron flux densities.
The process of nucleosynthesis takes place, when the temperature in the universe drops below $T \leq 1\,\mathrm{MeV}$ and proton neutron interconversion, due to weak interaction, is not in equillibrium anymore. The freeze-out produces an proton-neutron ratio of $\frac{n}{p} = \frac{1}{6}$, which is then slowly falling, because of free neutron decay. Although the binding energy of

[2] But it shouldn't, as this leads to velocities greater than c. It is more helpful to see this as a parametrisation of the scale factor a in the metric, which is related to the age of the universe. The redshift can then be explained as a general relativistic effect, similar to the gravitational reddening of an escaping photon from a gravitational potential

Deuterium is well above the temperature at this time, the high photon number prevents the formation of Deuterium. It is not until $T \leq 80\,\mathrm{keV}$ or $\frac{n}{p} \approx \frac{1}{7}$ that Deuterium can be formed and immediately processes all left over neutrons to ^{4}He with high efficiency. This leads to the observed ^{4}He mass fraction of 0.25. The only relevant parameter to this process is the proton to neutron ratio: $\eta = 10^{-10}\eta_{10} = 273\,\Omega_\mathrm{B}\mathrm{h}^2$. The left over neutrons are bound in Deuterium, ^{3}He and ^{7}Li. With Deuterium being most sensitive to the abundance ratio, it is the ideal "Baryometer". As it is not formed in considerable amounts in after recombination, only destroyed in stars, it sets an upper bound on η.

By observing Lyman-α absorbtion lines from high redshift quasars it is possible to measure the Deuterium abundance, relative to the Hydrogen abundance with high accuracy: $(D/H)_P = 2.310^{-5}$ [TFB96]. Combined with measurements of Lithium-7 from Pop II halo stars and Helium-4 from low metallicity, HII regions, this constraines $\eta_{10} = 4.2 - 6.3$ and therefore the baryon density.

The Cosmic Microwave Background was found in 1964 by Penzias and Wilson and is interpreted as the redshifted radiation still present from that epoch of matter and radiation decoupling. Modern measurements by the COBE and WMAP satellites, show unifrom, isotropic radiation, following the blackbody / Planck spectrum at $2,726 \pm 0,010\,\mathrm{K}$ [MCC$^+$94].

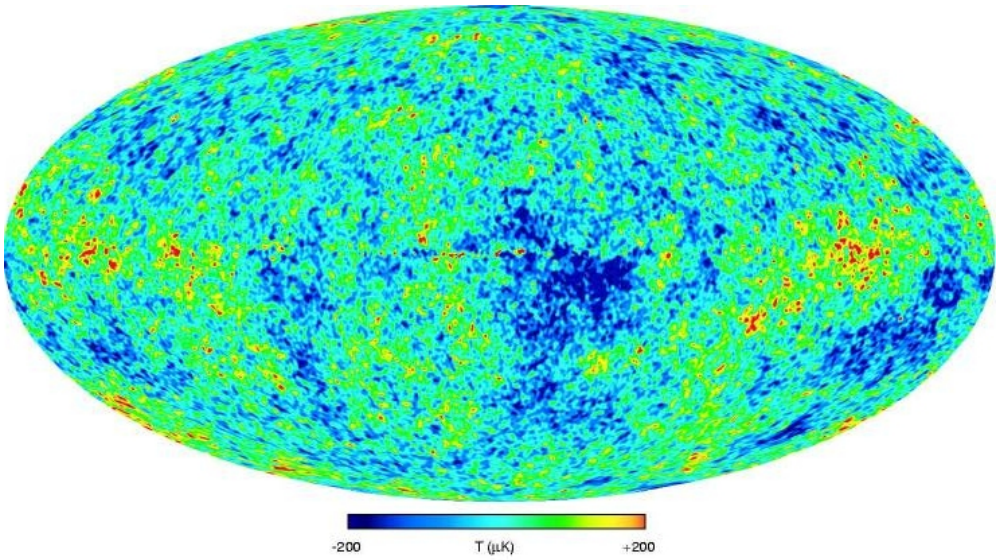

Figure 2.5: All sky map of the temperature fluctuations from WMAP [BHH$^+$03]

An analysis of the deviations from that fit, shows besides a dipole component, that results from the satellites relative movement with respect to the CMB, a characteristic size of the residuals. The analysis is done, by fitting spherical harmonics / multipoles

to "patches on the sky". Assuming the fluctuations are Gaussian of type, their power spectrum is given by:

$$\langle \Theta^*_{lm} \Theta_{l'm'} \rangle = \delta_{ll'} \delta_{mm'} C_l \qquad \Theta_{lm} = \int d\vec{n}\, Y^*_{lm}(\vec{n})\, \Theta(\vec{n}) \tag{2.9}$$

with the observed spectrum shown in figure 2.6.The temperature fluctuations translate into density inhomogeneities of length λ on the electron coupled photon-baryon-plasma at the time of recombination ($z = 1000$) parametrised by the angular diameter distance. For a flat universe ($\Omega_{tot} = 1$): $\Theta \approx \lambda / D$

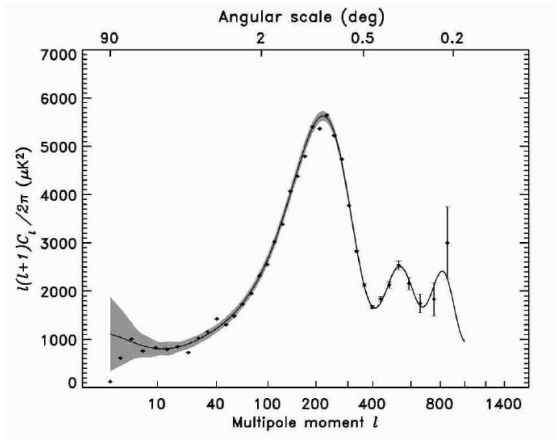

Figure 2.6: CMB Powerspectrum [BHH+03]

The inhomogeneities themselves are believed to be a result of fluctuations in the inflaton field (see **??**). A large variety of effects contribute to the shape of the power spectrum shown in 2.6. The temperature fluctuations of the fluid are decribed by Euler and continuity equation in fourier space; taking into account several interactions between the components present in the universe at that time: dark matter, radiation and baryons.

Because the radiation field is interacting with the gravitational potential of baryons and dark matter, the seen temperature fluctuations are described by an effective temperature $\Theta + \Psi$. Here Ψ is represents fluctuations in the gravitational potential. The equations describe a damped oscillator.

The shape of the spectrum can be understood, when considering that with time, larger scales of the initial temperature fluctuation spectrum enter the sound horizon, i.e. become causally connected to each other:

- Scales larger than the sound horizon have not had time to interact, the primordial spectrum is therefore frozen into the plasma. This describes the slope of the spectrum for small k / large angles, where CMB photons have to overcome the gravitational potential and are redshifted by general relativistic reddening. This is the Sachs-Wolfe effect, which can be used to estimate Ω_Λ using the slope of the spectrum[3].

- On scales smaller than the sound horizon at recombination the effective temperature oscillates driven by the radiation field at early times and is damped on small

[3]Note that for low k the errors of the spectrum become huge, because of cosmic variance. As k grows, the patches of the celestial sphere, used for fitting, grow. Therefore the statistic ensemble shrinks, until for the monopol only a sample of one remains.

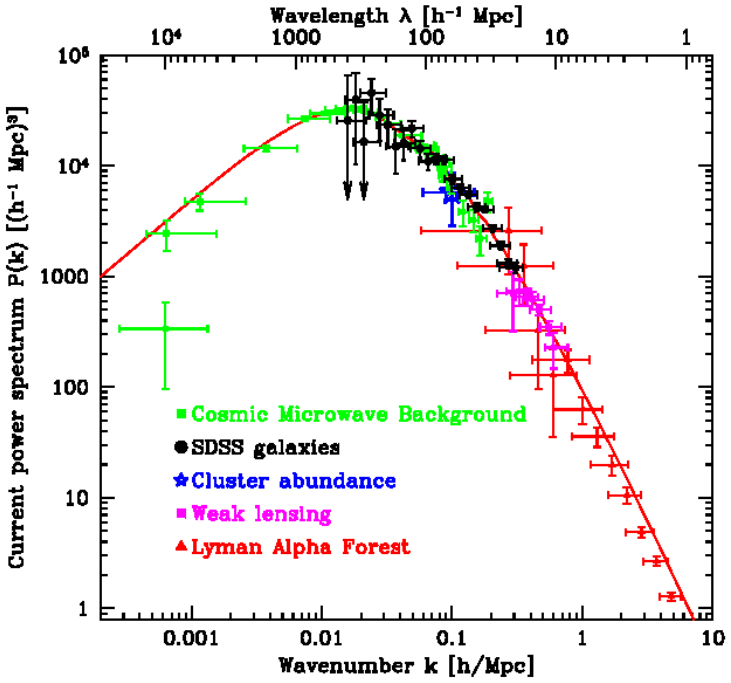

Figure 2.7: Current powerspectrum of galaxies from SDSS and other surveys[TBS+04]

scales by the fuild viscosity, when the universe becomes matter dominated. Before turn over radiation dominates the gravitational potential, driving the oscillations. When matter takes over its viscosity generates a quadrupole moment in the temperature, which damps the oscillations and generates polarisation patterns. At recombination the mean free path of electrons, that couple baryons and radiation, increases. This allows the photons to diffuse out to overdense regions, smoothing fluctuations on those scales (Silk Damping).

- At the time of recombination, the mode with a wavelength equal to the sound horizon and its harmonics are able to resonate, forming standing waves and the peaks observed.

Simplified it can be stated, that the mode of the first peak determines Ω_{tot}, the slope of the spectrum from low k Ω_Λ, the relative amplitude of the peaks to each other $\Omega_b h^2$ and the absolute amplitude of the peaks $\Omega_m h^2$. See [HD02] for a detailed discussion.

Large Scale Structure Another way to test cosmological models is by looking at the large scale structure of visible matter in the universe. Figure 2.7 shows the Fourier

transform of the matter distribution in the universe. It combines measurements from the CMB on large scales (small wavenumber), the galaxy and quasar distribution in the Sloan Digital Sky Survey[4], the distribution of galaxy clusters[5], weak lensing[6] and the Lyman alpha forest[7]. Most of these observations measure the distribution of *baryonic* matter in the universe, which is unfortunately dominated by the dark matter potential. A linear bias is usually invoked to get the dark matter distribution on large scales. Simulations show, that the bias is scale dependent. The shape of the initial spectrum is modified by structure formation, commonly modelled by the transfer function.

During structure formation, fluctuations become larger than their Jeans length. i.e. are gravitational unstable and collapse to denser structures. As the universe evolves, increasingly larger modes enter the hubble horizon, where, before matter domination, the pressure support by the radiation field dominates over the gravitational potential, stopping the contraction. When after turn-over matter dominates the kinematics, the radiation field prevents the baryons from flowing into the Dark Matter potential. Meanwhile Dark Matter starts to clump on those scales. When the plasma becomes opaque at recombination, the interaction of the photon field with the baryons stops, the baryonic matter falls into the dark matter potentials.
It follows, that the powerspectrum should mimic the primordial power spectrum on large scales/small k, as fluctuations of that size were never causally connected to each other and contract if they are below their Jeans length. Fluctuations on small scales/large wavenumber, were inside the hubble horizon even before matter domination, when dark and baryonic matter evolution was frozen by radiation driving. After matter-radiation equality Dark Matter decoupled, after recombination baryonic matter, so the powerspectrum is described by the transfer function. The point of turnover from one scale to the other is determined by the horizon scale at matter-radiation equality. It must be determined observationally.

The normalisation of the spectrum is measured either by comparing the CMB temperature fluctuations or by number counts of hot X-Ray emitting clusters in the local universe. It is then related to σ_8, the averaged overdensity value in a 8 Mpc sphere[8].

Dark Matter And Dark Energy There is evidence for dark matter not only in CMB data and large scale structure, but also on very different scales. Zwicky proposed non-seen matter back in 1933 [Zwi33], where he found anormalous velocity dispersion of satellite galaxies in galaxy clusters. Today X-Ray observations show hot gas in the center of clusters. Its mass is still not sufficient to explain the potential inferred from

[4] the Sloan Digital Sky Survey, aims at mapping 25% of the sky, observing $\approx 10^8$ objects to redshifts of up to $z = 0.4$ for galaxies and $z = 5$ for quasars.
[5] This is done via a number count per volume
[6] General relativistic distortion of resolved high redshift objects, induced by structure
[7] Absorbtion lines in the spectra of quasars from hydrogen gas clouds in the line of sight.
[8] The value comes from the historical count of galaxies, that resulted in $\sigma = 1$ in 8 Mpc spheres.

the velocities of sourrounding galaxies. In contrast the temperature of the gas is in good agreement with the potential implied by the Kepler law.

Other evidence comes from gravitational lensing measurements. This method analyses the average elongation of background galaxies in spatial bins of the clusters on the sky. Statistically it should vanish, so measured elongation must be due to relativistic light bending, by mass in front. For this certain assumptions about the structure of the cluster have to be made, which is a possible source for errors. Still the mass found by gravitational lensing is too large compared to the visible contents. Recently apparent seperation of luminious matter from gravitational potential was detected. The so called bullet cluster [CBG+06] shows two seperated mass centers (from lensing) and two of center shockfronts from hot gas in the X-Rays. This interpreted as a merger of two clusters, where the Dark Matter haloes, being collisionless, interpenetrate, while the gas collides, resulting in two show fronts seen with Chandra.

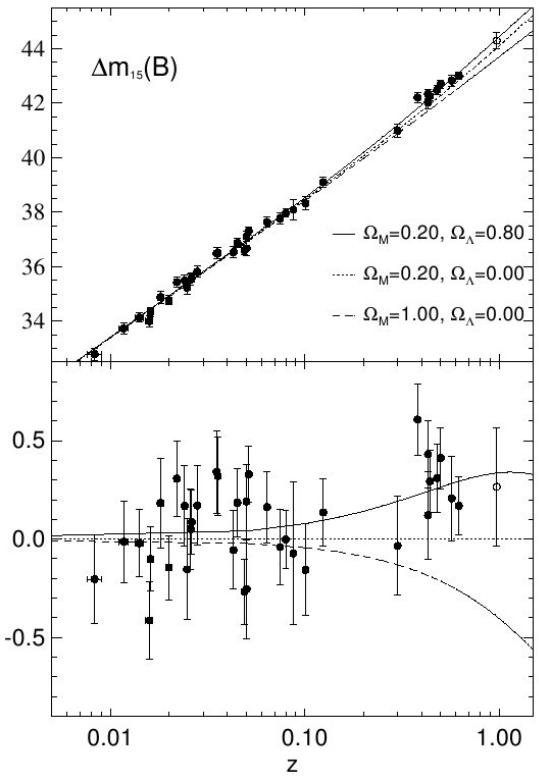

Figure 2.8: Modern Hubble diagram with residuals [RFC+98]

Dark matter is detected in galaxies as well. Observations[9] of 21 cm line emission of gas clouds can be used to determine their rotation velocity over radius. For large radii, most of the mass should be inside the clouds trajectory, so the rotation curve should flatten out. This is not observed, leaving the conclusion that there is still significant non radiative mass at large radii. The mass is identified with dark matter and its profile can be modelled elegantly using the NFW profile [NFW96].

On cosmological scales, modern hubble diagrams up to redshift $z > 1$, are established using type 1A supernovae as distance indicators. They are calibrated by a luminocity - lightcurve relation. Figure 2.8 shows a modern hubble diagram, indicating an accelerating universe.

Due to the Sachs-Wolfe effect the shape of the CMB powerspectrum at small wavenumbers is modified. The acceleration of the expansion changes the depth of gravitational potential. A photon is blueshifted, when it enters a potential well and redshifted, when

[9] e.g. [RW75] in M31.

Parameter	Mean and 1σ Error
Amplitude of fluctuations,A	$0.836^{+0.09}_{-0.08}$
Spectral index @ $k = 0.05\,{}^{1}/_{\mathrm{Mpc}}$,$n_s$	0.93 ± 0.03
Derivative of spectral index, $\mathrm{d}n_s/\mathrm{d}\ln k$	$-0.031^{+0.016}_{-0.018}$
Hubble constant, h	$0.17^{+0.04}_{-0.03}$
Baryon density, $\Omega_b h^2$	0.0224 ± 0.0009
Matter density, $\Omega_m h^2$	$0.135^{+0.008}_{-0.009}$
Optical depth at reionisation, τ	0.17 ± 0.06

Table 2.1: ΛCDM parameters from a fit to WMAP, 2dFGRS, Lyα forest, CBI and ACBAR measurements [SVP+03]

it leaves the potential. See [BHH+03] for more details on the spectrum. The equation of state of Dark Energy is still under debate. The simplest choice is the addition of a cosmological constant Λ in 2.1, similar to a vacuum energy of space, a source of negative pressure. Problems with Λ arise when its estimates from quantum field theory are compared to the values found by e.g. WMAP. The results differ by about 120 orders of magnitude!
When looking at the time evolution of Dark Energy, which is just starting to dominate the universes dynamics today, a cosmological constant (with $w = -1$ in the equation of state and constant time evolution) needs to be fine tuned very accurately at Planck times, to dominate just today. As $\rho_m \propto a^{-3}$ and $\rho_r \propto a^{-4}$, the currently estimated value $\rho_\Lambda = \Lambda/8\pi G \approx 10^{-47}\,\mathrm{GeV}^4$ leads to $\rho_\Lambda/\rho_r \approx 10^{-55}$ at time of electroweak phase transition. This can be solved by invoking dynamical models like Quintessence, which couples a time evolving scalar field to gravity. Still CMB, large scale structure and SN1a observations constrain the equation of state parameter to be $w < -0.82$ with 95% confidence [Sah05].

2.1.3 The λ CDM model

To conclude this section, we will briefly summarize the parameters used by the ΛCDM model, which is the basis of our simulations. The basic parameter describing the cosmological concordance model and their values are shown in Table 2.1. It is assumed that the universe is flat (i.e. $K = 1$ in 2.5). Fluctuation amplitude, spectral index and its derivative describe the shape of the initial spectrum of fluctuations, which leads to CMB anisotropies and the matter powerspectrum observed by galaxy surveys. The hubble constant parametrises the expansion rate today and approximates the age of the universe. Baryon and matter density combined with the assumption of flatness lead to a dark matter density (Eqn. 2.5). The optical depth at reionisation parametrises the time, when the first stars reionised the baryons in the universe. It describes the formation of population III stars.

2.2 Gravitation

On large scales matter interacts solely by the gravitational force. The universe contains collisionless dark matter and dissipative baryonic matter, both following gravitation. Two valid theories describing gravitation exist: Newtons force laws and Einsteins theory of general relativity. While a proper description of the behaviour of the whole universe requires full general relativity, structure formation on scales of our simulations, does not. We therefore use the classical approach.

Then the gravitational potential follows Poisson equation, which describes how the potential ϕ is generated by mass density ρ_m:

$$\nabla^2\Phi(\vec{x}) = 4\pi G\rho_m \tag{2.10}$$

$$\vec{F_i} = -m_i\nabla\Phi_j \tag{2.11}$$

$$\tag{2.12}$$

where $G \approx 6.6 \cdot 10^{-11}\,{}^{\mathrm{m}^3}/_{\mathrm{kgs}^2}$ is the gravitational constant. The force can then be found by the gradient of the potential. Gravitation is purely attractive and the measure of this force is mass. To treat dark matter it is sufficiently accurate to model it as a collisionless fluid interacting with its own Newtonian potential.

2.3 (Magneto-) Hydrodynamics

In statistical mechanics, the time evolution of a system of particles is described by the Bolzmann equation. If we would want to describe all matter in the universe with this, we'd have to consider that every gramm contains around 10^{29} particles. A rough estimate for all particles in the unverse gives around 10^{84}, leaving us with an impossible task. If we are not interested in the trajectory of every particle, but only in macroscopic quantities like density and bulk velocity, we can forget about this impossible large number of particles. We use a contiuum approximation that masks uninteresting information, but probably important physics as well. In the first section we describe the statistical basis of Hydrodynamics as a Lagrangian theory.

Most gaseous matter in the universe is found to be a plasma, which consists of charged particles, but carries no net charge. Dealing with magnetic fields, requires Hydrodynamics to be modified by Maxwell's theory of electrodynamics, leading to Magnetohydrodynamics. From this theory we achieve a description, how a flow generates and dissipates magnetic fields (2.3.2). It becomes important later, that weak magnetc fields are frozen into a plasma (2.3.3). This leads to the $\alpha-\Omega$ dynamo (2.5.1) and enables us to build our wind model in simple terms. Magnetohydrodynamics and Gravitation form the basis for the GADGET simulation we present. For simplicity we don't mention multi-fluid theory here.

2.3.1 Distribution Function and Boltzmann Equation

To find a usefull description for the particles that form a plasma, it is usefull to define a distribution function[10] $f(\vec{r}, \vec{w}, t)$, that describes the collective behaviour of all particles in phase space by:

$$\Delta^6 N(\vec{r}, \vec{w}, t) = f(\vec{r}, \vec{w}, t)\, \Delta^3\vec{r}\Delta^3\vec{w} \tag{2.13}$$

where $N(\vec{r}, \vec{v}, t)$ is the number of particles in a volume element of phase space $\Delta^3\vec{r}\Delta^3\vec{v}$. The moments of the distribution function contain the macroscopic quantities we are interested in:

$$\rho(\vec{r}, t) = m \int f(\vec{r}, \vec{w}, t)\, d^3\vec{w} \qquad \vec{v}(\vec{r}, t) = \frac{m}{\rho(\vec{r}, t)} \int \vec{w} f(\vec{r}, \vec{w}, t)\, d^3\vec{w}$$
$$Q(\vec{r}, t) = q\frac{m}{\rho(\vec{r}, t)} \qquad \vec{j}(\vec{r}, t) = Q(\vec{r}, t)\vec{v}(\vec{r}, t)$$

The mass density $\rho(\vec{r}, t)$ in configuration space follows as the integral over all velocites times the particle mass. The flow velocity $\vec{v}(\vec{r}, t)$ computes as the weighted mean of the velocities of the particles. Then random velocities can be defined, whos mean gives thermal velocity v_T and therefore kinetic temperature by : $v_T^2 = \frac{k_B T}{m}$. It is equal to thermodynamic temperature in the case of thermal equillibrium. For MHD we need to define the charge of a flow element $Q(\vec{r}, t)$ and its current density $\vec{j}$

The time evolution of distribution function, and therefore of all macroscopic quantities, is described by the Boltzmann equation[11]:

$$\left(\frac{\partial f}{\partial t}\right)_{coll} = \frac{\partial f}{\partial t} + \vec{w} \cdot \nabla_x f(\vec{r}, \vec{w}, t) + \frac{1}{m}\nabla_x \psi \cdot \nabla_w f(\vec{r}, \vec{w}, t) \tag{2.14}$$

Here ψ denotes a potential, i.e. an external force like gravitation defined by Newtons law. The collision term on the left side of 2.14 includes all interparticle force. It has to be defined seperately and depends heavily on microphysics like the scattering crossection of the involved particle species. Combined with an equation of state (e.g. for an ideal gas) and the equations for gravitational potential (ψ) these equations form a closed system.

Solutions to Boltzmanns equation are not easily found. While the microscopic orbits of particles are driven on scales of crossections and scattering times, global quantities like density and average velocity change in macroscopic scales. Hydrodynamics solves this problem by focussing on the collective behaviour of the particles. A close look at 2.14 reveals, that its complexity lies in the degrees of freedom (7 variables) and the collision term. As all macroscopic quantities are found by integration over velocity space, one uses

[10] For simplicity we assume one species of point like particles

[11] We don't derive it here. See [Goo03] for an intuitive and [HM05] for a stricter derivation

the moments of 2.14 corresponding to those quantities to find solutions. This simplifies the theory a lot, so we loose information about the system. Only a infinite number of moments builds a complete set of equations. The collision term can be dealt with, by considering only collisional invariant quantities. Then elastic collisions give a set of conservation laws: Particle, momentum and energy conservation. The average collision frequency determines many properties of the plasma. Collisionless plasmas have a very low resistivity, while collisional domination symmetrizes the distribution function.

2.3.2 Ideal and resistive MHD

We don't want to show how the first, second and third order velocity and first order charge moments of the Boltzmann equation lead to the MHD equations, see [Goo03] for the derivation.
From the Boltzmann equation follow 4 conservation laws:

$$\begin{aligned}
\text{mass} \qquad & \frac{d\rho}{dt} + \rho\nabla\cdot\vec{v} = 0 \\
\text{electric charge} \qquad & \frac{\partial Q}{\partial t} + \nabla\cdot\vec{j} = 0 \\
\text{momentum} \qquad & \rho\frac{d\vec{v}}{dt} + \nabla\cdot P - \rho\vec{g} - Q\vec{E} - \vec{j}\times\vec{B} = 0 \\
\text{internal energy} \qquad & \frac{dp}{dt} - \frac{\gamma p}{\rho}\frac{d\rho}{dt} = (\gamma-1)\left[-\nabla\cdot\phi + \vec{E}^*\cdot\vec{j}^* - \sum_{l=1}^{3}\sum_{k=1}^{3}\Pi_{kl}\frac{\partial v_l}{\partial x_k}\right]
\end{aligned}$$

with ρ,$\vec{v}$,Q,$\vec{j}$ macroscopic density, velocity, charge and current density as defined above. Further $P_{kl} = p\delta_{kl} + \Pi_{kl}$ the pressure tensor with isotropic pressure p and anisotropic part Π_{kl} , $\vec{g}$ is the gravitational force vector as defined by Newton's law and $\vec{E}$ and $\vec{B}$ electric and magnetic field from Maxwell's equation. Note that we switched to a Lagrangian description for the fluid, by introducing convective derivative $\frac{d}{dt} = \frac{\partial}{\partial t} + \vec{v}\cdot\nabla$. The conductive current density $\vec{j}^*$ and convective electric field[12] $\vec{E}^*$ are the "Lagrangian version" of the fields defined by electrodynamics. $\gamma = (f+2)/f$ connects to the internal degrees of freedom of the particle (f). ϕ is the heat flux.

The first two equations state that the total time change of density and charge in a volume must be minus the flow of these quantities in resp. out of this volume. In the third equation momentum change (force) in a volume results from a change in pressure or from gravitation acting on mass, electric field acting on charge or magnetic field acting on current density. The change in internal energy of a volume ($\gamma p/\rho$) is generated by heat flux, Ohmic heating or anisotropic stress, which are all a result of the collision term in 2.14.

[12] The electric field seen by an Lorentz transformed observer, that follows the fluid

Induction Equation The 4 equations do not represent a closed system as the current density is not linked to the hydrodynamic quantities. Closure is achieved by the generalized Ohm's law, which derives as first charge moment from the Boltzmann equation (see [Goo03] for the details). It connects the electromagnetic fields $\vec{E}$ and $\vec{B}$, and the current density $\vec{j}$, $\dot{\vec{j}}$ with fluid quantities like electron pressure p_e and velocity $\vec{v}$:

$$\vec{E} = -\underbrace{\left(\vec{v}\times\vec{B}\right)}_{\text{Induction term}} + \underbrace{\frac{\vec{j}}{\sigma}}_{\text{Ohmic term}} + \underbrace{\frac{1}{en_e}\left(\vec{j}\times\vec{B}\right)}_{\text{Hall term}} - \underbrace{\frac{1}{en_e}\nabla p_e}_{\text{Battery term}} \tag{2.15}$$

where σ is the electrical conductivity, n_e the electron number density and e the electron charge.

Doing a scale analysis with typical values found in astrophysics[13], one can show that the induction term dominates ([Goo03], page 99), which leads to *ideal MHD*. Considering the Ohmic therm as well gives *resistive MHD*.

Ideal and Resistive MHD With this preamble the equations for ideal and resistive MHD follow, with non relativistic Maxwell equations, i.e. without electromagnetic radiation:

$$\frac{\partial\rho}{\partial t} = -\nabla\cdot(\rho\vec{v}) \tag{2.16}$$

$$\rho\frac{d\vec{v}}{dt} = -\nabla p + \rho\vec{g} + \frac{1}{\mu}\left(\nabla\times\vec{B}\right)\times\vec{B} \tag{2.17}$$

$$\frac{dp}{dt} = -\gamma p\nabla\cdot\vec{v} + \underline{(\gamma-1)\frac{\left|\nabla\times\vec{B}\right|^2}{\mu^2\sigma}} \tag{2.18}$$

$$\frac{\partial\vec{B}}{\partial t} = \nabla\times\left(\vec{v}\times\vec{B}\right) + \underline{\eta\nabla^2\vec{B}} \tag{2.19}$$

$$0 = \nabla\cdot\vec{B} \tag{2.20}$$

the underlined parts represent resistive MHD. Note that equation 2.19 can not generate magnetic fields, only amplification is possible. This poses a crucial problem on the fields found in the universe.

2.3.3 Scope and Limits of ideal Magnetohydrodynamics

We don't want to deal with the errors introduced from numerical resolution here, see 5.3 for details. Focussing on MHD as a model for plasma physics, simplifications on different length, time and energy scales limit the validity of the model:

[13] Meaning large Reynolds Numbers, where : $R_m = \frac{Lv}{\eta}$ with a typical length scale L, a velocity v and the magnetic diffusivity η. In astrophysics the L dominates.

1. Quantum mechanical effects are neglected. From this $\int f(\vec{r},\vec{w})\, d^3x\, d^3p \gg N_{part} \cdot (2\pi\hbar)^3$ is assumed, so the Boltzmann equation can be used.

2. (General) Relativistic effects are neglected. This means for the fluid velocity: $v_f \ll c$, for Maxwells equations: no displacement current $d\vec{E}/dt = 0$ in Maxwells equations and no electromagnetic radiation.

3. MHD is a single fluid theory, it can not be valid for frequency and length scales, where ions and electrons behave differently. The distribution function of all particle species is then the sum over their distribution functions.

4. Only elastic collisions take place in short enough time scales so that the collision term is energy and momentum conserving. It follows that, there is no anisotropic stress[14]. A common temperature of all components in a fluid cell can be defined, which requires the equilibration time τ_{eq} to be much smaller than the system timescale $L/V_{t,i}$. Then the global distribution function is Maxwellian, i.e. isotropic. Thus thermal conduction is impossible, which is equivalent to :

$$\frac{m_i}{m_e}\frac{\tau_{e,i} v_{T,i}}{L} \ll 1$$

   where $\tau_{e,i}$ is the electron-ion collision timescale.

5. Particle effects don't play a role in MHD, the average particle distance $r_{L,i}$ is negligible compared to the system length scale L. The same accounts for the collision frequency scale ω so:

$$\frac{r_{L,i}}{L} \ll 1 \qquad\qquad \frac{\omega}{\omega_{c,i}} \ll 1$$

6. Using the Boltzmann equation assumes that only short range forces act on the flow. This does not impose a problem in the case of electromagnetism, if we neglect electrostatic forces, because of Debye shielding (quasi neutrality over scales larger than the debye length) and assume non radiativity. Gravitation has to be introduced as an external potential, which has to be smooth enough on scales of a fluid cell.

7. Ideal MHD requires the Reynolds number to be much larger than one, which is mostly the case in cosmology. The reason for this are the huge dimensions of the system, not an infinite conductivity, which is unphysical.

Magnetohydrodynamics will fail when time and length scales of the processes considered fall below those defined above. This is the case for example in shocks.

[14] From this, we can write the energy momentum tensor stated in 2.1 for Baryons.

Concerning the application of MHD for the ICM, [Jon07] estimates the collisional mean free path as $l_{c,p,e} \approx 22\,\mathrm{pc}$, if only Coulomb interaction is considered. This contradicts high collisionality mentioned above. He concludes that plasma processes and magnetic fields might lead to higher effective collision rates, via e.g. two stream instability or confinement of the particle motion perpendicular to the field lines.

They find large magnetic Reynolds numbers and negligible Ohmic heating in clusters. Assuming Spitzer conduction results in nearly no heat conduction. This might not hold when small scale turbulence tangles field lines on smaller scales than the Coulomb scattering length. Still, observed cold fronts require locally small conductivity.

Frozen Fields The most important result of MHD for us, is the freezing of magnetic field lines into the plasma.
It follows from flux conservation through a surface moving with the flow at $\vec{u}$. The time change of a vector field in this surface is given by the divergence of the field minus the rotation generated. Considering 2.20 and 2.19:

$$\frac{d\Phi_B}{dt} = \frac{d}{dt}\int \vec{B}\cdot\vec{n}\,dS \tag{2.21}$$

$$= \int \left(\frac{\partial \vec{B}}{\partial t} - \nabla\times\left(\vec{u}\times\vec{B}\right) + \vec{u}\nabla\cdot\vec{B}\right)\cdot\vec{n}\,dS \tag{2.22}$$

$$= 0 \tag{2.23}$$

The magnetic flux through a surface, that follows the flow is constant. The field is *frozen* into the flow or other way around. If the motion perpendicular to the field lines is dominated by either one of them, is determined by the ratio of plasma to magnetic pressure:

$$\beta = \frac{p}{B^2 2\mu} \tag{2.24}$$

This behaviour is a basic property of ideal MHD, deviations from perfect field dragging occur in resistive MHD.

2.4 Observing Magnetic Fields

Measuring galactic or even cosmic magnetic fields is not an easy task. There exist several methods to estimate the field strength and direction on different scales. In the following section, we explain about 4 of them. In the context of galaxy clusters Synchrotron emission and Faraday rotation are most important. Afterwards we take a look at the observed field strengths in galaxies and clusters.

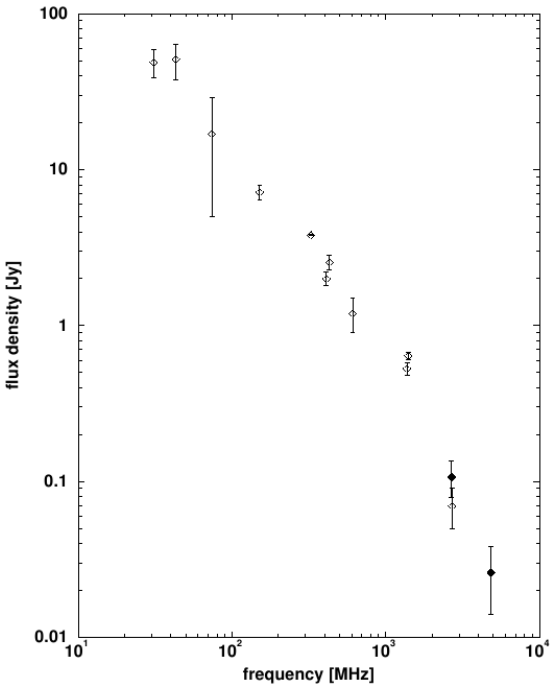

Figure 2.9: Spectrum of the diffuse radio halo in Coma C. For a constant field, the inferred electron spectrum has the shape of a powerlaw. [TKW03]

2.4.1 Synchrotron Emission from Electrons

In a plasma containing a magnetic field, electrons move in spiral trajectories along the field lines, emitting elliptical polarised radiation. Taken into account an ensemble of electrons, one can show, that the resulting averaged radiation is linearly polarised. The particle motion normal to the plane of the electric and the magnetic field is randomly distributed; the field amplitude cancels out by destructive interference (see [GS65], 3.2).

To get an quantitative description [Wid02], one must estimate the energy distribution between cosmic rays and magnetic field. The total energy density is written as : $\varepsilon_k = (1+k)\,\varepsilon_{re} + \varepsilon_B$ where $k \approx 100$ is constant and ε is the total, relativistic electron or magnetic field energy density, respectively.

$$\varepsilon_{re} = \int n\,(E)\,E dE \tag{2.25}$$

$$\varepsilon_B = \frac{1}{8\pi} B^2 \tag{2.26}$$

The energy spektrum of the electrons is commonly modeled by a power law (see figure

2.4.1), with a spektral index $\gamma \cong 2.6 - 3.0$ and the electron energy distribution $n_e(E)$.:

$$n_e(E)\,dE = n_{e0}\left(\frac{E}{E_0}\right)^{-\gamma} dE \tag{2.27}$$

To get the cosmic ray electron density from observable quantities the synchrotron emissivity for all energy bands and for one electron are calculated from:

$$j_\nu = \int J(\nu, E)\, n_e(E)\, dE \tag{2.28}$$

$$J(\nu, E) \propto B_\perp \left(\frac{\nu}{\nu_c}\right)^{\frac{1}{3}} f\left(\frac{\nu}{\nu_c}\right) \tag{2.29}$$

with a cut off function f, so that: $f(x \to 0) \to 1$ and $f(x \gg 1) \to 0$,$\nu_c = \nu_L(E/mc^2)$ the critical frequency and $\nu_L = (eB_\perp/2\pi mc)$ the Lamor frequency. The frequency dependence emerges from a lengthy calculation using the retarded potential. From 2.28 follows, that the emission at a certain frequency is mostly from an energy band E_0 around the critical frequency. We can therefore approximate the emissivity by: $J(\nu, E) \approx B_\perp \nu_c \delta(\nu - \nu_c)$ and write the electron distribution in terms of frequency: $n(\nu_c) = n_e(E)dE/d\nu_c \propto j_{\nu_c}/\nu_c B_\perp$. For the cosmic ray electron density follows then:

$$\varepsilon_{re} = \int_{\nu_L}^{\nu_U} En(\nu_c)\, d\nu_c \tag{2.30}$$

$$\propto B^{-\frac{3}{2}} \Theta^2 S_\nu(\nu_0) \tag{2.31}$$

with the observables : $S_\nu(\nu_0)$ – total flux density, Θ – the angular size of the source and ν_0 the charakteristic frequency inside the oberservers bandwidth.

Usually one assumes *equipartition*, e.g. equal distribution between ray and field energy : $(1+k)\,\varepsilon_{re} = \varepsilon_B$ or chooses the field, so that the total energy density is minimised (*minimum energy method*). This leads to an expression for the magnetic field:

$$B_{eq} \propto S_\nu^{\frac{2}{7}} \Theta^{-\frac{4}{7}} \tag{2.32}$$

The equipartition assumption is under discussion [BK05], as doesn't hold in certain extreme condition such as supernovas and strong shocks, where a redistribution of the magnetic energy takes place. Though, good agreement is found in our galaxy.

The direction of the IGM magnetic field can be estimated by the polarisation of the synchrotron radiation. As mentioned above, ensembles of electrons radiate linear polarised light. For a regular magnetic field, the polarisation is determined from the spectral index γ by:

$$p_H = \frac{\gamma + 1}{\gamma + \frac{7}{3}} \tag{2.33}$$

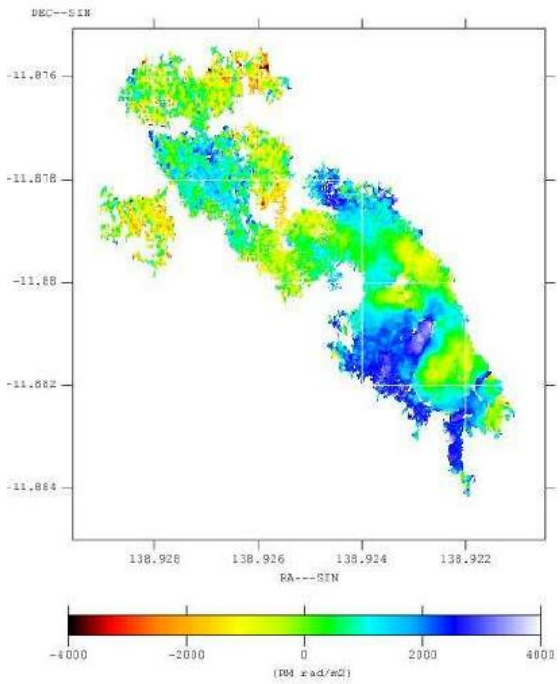

Figure 2.10: Faraday Rotation Map of Hydra A [VE05]

A population of relativistic electron in the gas at the center of galaxy clusters will interact with background photons, mostly from the CMB. They are up scattered by inverse Compton scattering to the X-ray regime. By comparing synchrotron luminocity and non thermal X-ray luminocity, one finds the field to be

$$B = 1.7(1+z)^2 \left(\frac{S_r \nu_r}{S_x \nu_x} \right)^{0.5}$$

if the electron energy density follows a power law with an photon index $\alpha = -1$. Here S_r denotes radio flux density and νx observed X-ray frequency.

2.4.2 Faraday Rotation

Another way to measure magnetic fields in astronomy is the magneto-optic effect of Faraday Rotation. A medium containing free charges, such as electrons, and a magnetic field, changes the dispersion relation for electromagnetic waves passing along the field lines. As a linear polarised wave is described as a superposition of to circular polarised waves, this results in a turn of the field vector, when the wave propagates through the medium. The over all rotation angle depends on λ^2 and is proportional to the line of

sight integral over electron density and the field parallel to the observers view[15] :

$$\phi = \frac{e^2\lambda^2}{2\pi m_e^2 c^4} \int_0^{l_s} n_e(l) B_{\parallel}(l)\, dl + \phi_0 \tag{2.34}$$

$$= RM\lambda^2 + \phi_0 \tag{2.35}$$

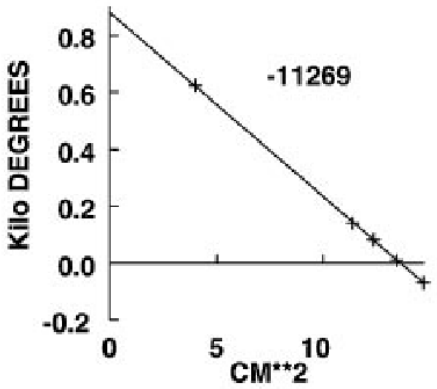

Figure 2.11: Measurement of RM over λ^2 in Hydra A (see fig. 2.10) [CT02]

The observation of polarised emission from giant synchrotron haloes, radio lobes of galaxies and in situ point sources like pulsars gives a handle on magnetic fields on that scales. Figure 2.4.2 shows a typical observation of the synchrotron emission in Hydra A. The magnetic field is here correlated to the inclination of the best linear fit through the data points by the integral above. The rotation measurement is degenerate in $n\pi$: i.e. every observation is not a point, but a series of points on a vertical line with the distance π in figure 2.4.2. It is a priori not clear which points of the lines to use. To find the best fit the RM is often observed several times for slightly different wavelengths (as seen on the right side of fig. 2.4.2). Additional observations at much different wavelengths are then used to obtain a line fit. Note that 2.4.2 is a rather perfect example with small errorbars. Often errors are large and the possible fit is not unambigous.

More advanced techniques try to get a handle on the correlation length / characteristic size of field reversals. A map of RM observations like figure 2.10 is binned and the dispersion from the average of the Faraday rotation of each bin is calculated. Assuming a random walk of the radiation through cells of a typical size but differently oriented magnetic field, the dispersion is proptional to the square root of the number of cells along the line of sight. With an assumption on the size of the object, the cell size follows then.

Possible errors result from the finite beamsize [16] as well as its wavelength dependence. Small structures will be seen avergaged, if they are smaller than the beamsize. Furthermore a RM value is obtained from different observed frequencies, for which the telescope resolution changes. Therefore the averaged out regions on the sky, differ for every band, complicating the data reduction even more.

[15] A more detailed derivation can be found in Appendix C.2

[16] The beamsize, corresponding to the PSF in optical Astronomy, is defined as the best possible resolution a telescope can achieve, even with perfect reflecting surfaces. This is basically determined by the fourier transform of the aperture.

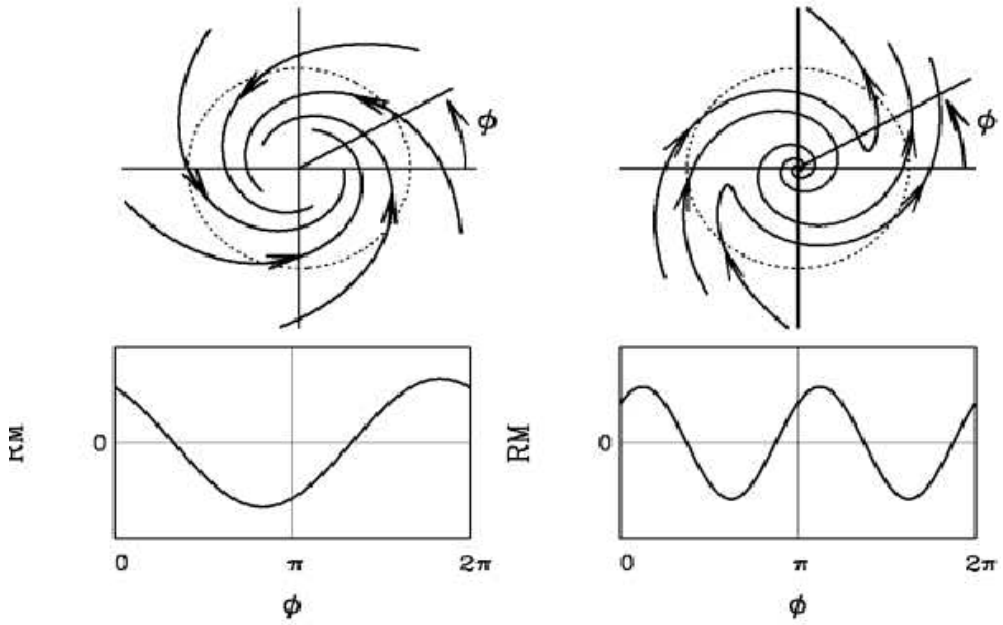

Figure 2.12: Axis- and bisymmetric field structure patterns in the disc. The two graphs below show the rotation measurement over angle at a fixed radial distance. [Wid02]

2.4.3 Observational Status Quo

Galaxies & The Milky Way

In our own galaxy, total local fields strengths around $|B| \sim 6\,\mu$G with a regular component of $|B| \sim 4\,\mu$G have been found [Bec02]. Other galaxies inhibit similar to larger values. [FA93] derived an average field of $< B_{eq} > \approx 11 \pm 4\,\mu$G from a sample of 146 late type galaxies. They use the minimum energy condition for synchrotron radiation from a plasma (see 2.4.1) and model the galaxy as thin disc scaled to the actual galaxy size. Anormalous galaxies like M82 inhibit higher field strength of up to $\approx 50\,\mu$G, because of turbulent amplification by excessive star formation.
The field structure parallel to the rotation axis out of the disc is referred to as poloidal. It is classified by its reflection symmetry about the plane of the disc. Symmetric/Asymmetric behaviour is marked with Sm or Am respectively. The m denotes the periodicity of the toroidal field. Figures 2.14 and 2.13 shows cross-sections parallel to the axis of rotation for an A0 and S0 field. So far observations do not strongly determine this parameter. Further it is not clear, if the field lines point inward or outward the center of the galaxy. This can be observed be comparing the sign of the RM with the velocity field. Dynamo theory does not favour one direction over the other.

For this work a symmetric field corresponds to seeded dipol, while the quadrupole is an A0 mode. From a statistical point of view, it seems more likely, that symmetric modes dominate for most galaxies (R. Beck, private conversation). We align the seeded quadrupoles with the field lines pointing outward in our simulation. As the analysis of the filling factors will show, the influence of the field geometry on the over all filling factor in a cluster is negligible.

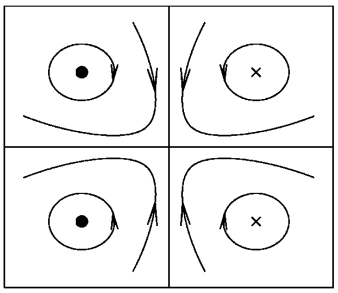

Figure 2.13: Poloidal quadrupole field [Wid02]

Maps of linear polarised synchrotron emission often show a connection of the magnetic field and the spiral structure of galaxies, especially with the low density between two arms. This suggests, that either the material in the arms destroys the field or the dynamo is more efficient in the lower density regions. In barred galaxies, fields are found along the bars. Gas flowing along the direction of the bar, requires the particles to follow highly non-circular orbits. The field would then follow the motion of the gas, which contradicts a generation by dynamo action.

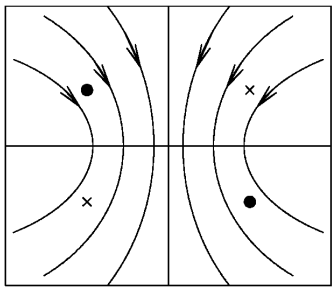

Figure 2.14: Poloidal dipole field [Wid02]

The magnetic field in halos of galaxies is often studied in edge on galaxies like M81. [HBD91] observed NGC 4631 and NGC 891 in the radio regime and found fields of up to $\approx 8\,\mu$G at $5-10\,$kpc. While in the former the field follows prominent radio spurs, in the latter no global structure can be found. The origin of those fields are most likely galactic winds, who escape the galaxies potential well.
A FIR - Radio Continuum Correlation was first found by [DS84]. It is confirmed for a variety of types of galaxies like spirals, irregular and cluster ones. Varified over four orders of magnitude, the mechanism is still not well understood. While FIR radiation is thermal and mostly a result of star formation, the radio continuum is made up of synchrotron radiation from relativistic electrons in a magnetic field. There are several suggestions, why those mechanism are connected, e.g. are both properties dependent on the density could gas clouds. They carry magnetic fields, and are connect to the star formation rate.

Clusters Of Galaxies

In table 2.2 an overview of measured field strengths in clusters can be found [CT02]. We will comment the most important observations in this section.

Line of sight measurements of Faraday rotation of intra clusters sources were first done in Cyg A where anormalous large gradients in the structure of RM were found. This ruled out an galactic origin of the RM, could be explained by an $2-10\,\mu$G cluster field and established RM measurements as a standard tool. Observations suggest that

Method	Strength [μG]	Model Parameter
Synchrotron Halos	0.4 - 1	minimum energy, $k = \eta = 1$, ν band
Faraday RM (embedded)	3 - 40	cell size = 10 kpc
Faraday RM (background)	1 - 10	cell size = 10 kpc
Inverse Compton	0.2 - 1	$\alpha = 1$, $\gamma_{radio} \approx 18000$, $\gamma_{xray} \approx 5000$
Cold Fronts	1 - 10	amplification factor ≈ 3
GZK	> 3	AGN is site of EeV CRs

Table 2.2: Cluster magnetic fields from different methods [CT02]

every source of polarised radio emission in cooling-flow clusters has high RM values. The spatial distribution is mostly found to be patchy on scales of some $5 - 10$ kpc suggesting a field reversal scale of that size. Non-line of sight modelling assumes a random walk of the RM through a number of cell from source to absorber. While the measured RM will be about 0, its dispersion is proportional to the number of cells along the line of sight. Assuming the canonical $\beta-$model for the X-Ray electron density one can calculate the number of cells along the line of sight. The found number of cells is roughly the same in the case of cooling and non-cooling flow cluster. The field strength in contrast is up to 3 times higher in the former case.
Background sources can be used as well to determine fields strengths. They are used to estimate the areal filling factor of the magnetic field. [CKB01] find high filling factors of $\approx 95\,\%$ in 16 low redshift Abell clusters. High redshift sources like radio loud quasars can be used to estimate the field in their environment. Difficulties arise from their small scale, which requires high frequency observations such that only high RM values can be measured.

Some Clusters show diffuse radio emission with a steep spectral index, which excludes thermal origin of the radiation. Typical sizes for the halos are ≈ 1 Mpc with low fractional polarisation ($< 5\,\%$) and low surface brightness well centered on the X-ray emission. Steep correlations between X-ray and radio luminocity and surface brightness have been found (see [CT02] for details). Using the minimum energy assumptions the estimated field strengths assume a frequency band of emission (usually $\nu = [10\,\text{Mhz}, 10\,\text{Ghz}]$), a completely filled volume (filling fraction $\eta = 1$) and equal energy densities of electron and proton component ($k = 1$).
There are indications for a connection between substructure in X-Ray images and the existence of radio haloes. This is pointing to a scenario, where radio haloes are a result of cluster mergers. A problem emerging with the latter model comes from the lifetimes of cosmic rays in clusters (see Appendix C.1). Due to adiabatic expansion, synchrotron losses and inverse Compton scattering, the fading time scale is well below 100 Myr. This is too short, for an eventual host galaxy to move on sufficiently.

2.5 Origin of Magnetic Fields on Large Scales

In this section we discuss the question of the origin of magnetic fields in galaxy cluster. The generator term in the MHD induction equation combined with the turbulent merging process of structure formation leads to an amplification of the frozen-in fields. The canonical $\alpha - \Omega$ Dynamo is described in the first part, which works for axisymmetric systems like a galaxy. Apart from that magnetic fields can be amplified in winds [BWO99] and by the structure formation itself. This happens trough turbulent motions, the merging process of galaxies falling into clusters and adiabatic compression.

As MHD allows only for existing fields to be amplified, the question arrises, where the initial field originated. The high metallicity of the IGM suggest that at least part of the intracluster field originates in cluster galaxies. The outflow mechnism can be modeled by AGN at low redshift, or by superwinds from dwarf galaxies at higher redshifts. This shifts the problem of the initial seed field from the cluster scale to their galaxies, where protogalactic processes like the Biermann battery can produce small seed fields at $10^{-20}\,\mu$G. Because of the high conductivity of the medium, this small fields will not decay and can be amplified.

Apart from that, a primordial origin is still possible. There are strong arguments that any primordial field on a scale smaller than the Hubble horizon at matter-radiation equality cannot survive until the time of recombination, because of magnetic and photon diffusion [BL00]. Thus every field on smaller scales must be produced by the plasma after reionisation. Only large scale fields can have inflationary origin and might influence structure formation. They are not of particular interest for this work.

2.5.1 Amplifying Magnetic Fields

We want to describe, how magnetic fields can be amplified in the universe, especially galaxies. The most important mechanism is the $\alpha - \Omega$ Dynamo. For this work a possible amplification in winds by shear flows is also important. The infall of structures during formation itself amplifies fields by adiabatic compression, as for the magnetic field energy density : $u_B = B^2/8\pi \propto \rho_g^{4/3}$

The $\alpha - \Omega$ Dynamo

The induction equation 2.19 states that amplification happens trough plasma motions perpendicular to field lines. To examine the way, magnetic fields can be amplified, we first consider a differential rotating plasma like a galactic disc of finite thickness. If it inhibits only a poloidal field ($\vec{B} \parallel \vec{\omega}$), it is obvious, that the differential rotation will produce a toroidal ($\vec{B} \perp \vec{\omega}$) component, by dragging the field line along with it. On the other hand a toroidal field, will not able to produce a poloidal field without motion parallel to the axis of rotation.

From the above follows, that axisymmetric motions can only amplify the torodial field. In the galactic context, this means, that turbulent non axisymmetric motions must play an important role. They can be quantified by the kinetic helicity α and turbulent resistivity β :

$$\alpha = -\frac{\tau}{3} < \vec{v} \cdot \nabla \times \vec{v} > \qquad \beta = \frac{\tau}{2} < \vec{v}^2 > \tag{2.36}$$

where the brackets denotes turbulent ensemble averages, and τ is the decorrelation time of turbulent motions. α describes a preferred direction of turbulent motions, that is caused by the Coriolis force acting on rising cells of turbulent motion. The kinetic helicity describes the angular twist of such a cell in one correlation time. β describes the mixing of the particles by their random walk, which smoothes the field and damps the amplification.

To derive an equation for the mean field, we split field and velocity in smooth, coherent and turbulent parts : $\vec{v} = \vec{U} + \delta\vec{v}$ and $\vec{B} = \bar{B} + \delta\vec{B}$. The induction equation of ideal MHD (2.19) can then be solved for the turbulent variables as :

$$\left\langle \delta\vec{v} \times \delta\vec{B} \right\rangle = \alpha\bar{B} - \beta\nabla \times \vec{B} \tag{2.37}$$

$$\frac{\partial \bar{B}}{\partial t} = \nabla \times \left(\vec{U} \times \bar{B}\right) + \nabla\left(\alpha\bar{B}\right) + \beta\nabla^2\bar{B} \tag{2.38}$$

the last equation is called the mean field dynamo equation. This can be applied to a thin (thickness h) disc by introducing cylindrical coordinates and assuming vacuum boundary conditions[17], i.e. a large β. The resulting two equations state an eigenvalue problem for a growing mode, that amplifies the field. Assuming an explicit form for $\alpha = a_0 z/h$ the eigenvalues are classified by the dimensionless number

$$D = -\frac{\Omega\alpha_0 h^3}{\beta^2} \tag{2.39}$$

called the dynamo number. For a given disc configuration, the number $D_c > D$ characterises exponentially growing modes on time scales of β/h^2 if the eigenvalue is equal to 1. Reasonable values[18] give growth times around $5 \cdot 10^8\,\mathrm{yr}$. The solutions to the eigenvalue equations are symmetric in z, so the field components above or below the disc are either both odd or both even. This corresponds to a quadrupole and a dipole mode. The observed parities agree best with the parity solution [KZ07].

[17] The vacuum boundary conditions impose problems on the dynamo. They remove a lot of magnetic flux from the disc.

[18] e.g. $\delta v \approx 10\,\mathrm{km/s}$, $\delta v\tau \approx 100\,\mathrm{pc}$, $\Rightarrow \beta \approx 1.5 \cdot 10^{26}\,\mathrm{cm^2/s}$

The assumed on axis turbulence is a result of supernova explosions, forming bubbles [Fer92]. 2.5.1 shows the way of operation. A poloidal pertubation is induced by a supernova wind, which blows out a bubble, dragging apart plasma and field lines in its outer shell (b). The field lines of the bubble are then dragged out/inwards. The moment of inertia of the bubble increases and its rotation slows down. It is twisted by the Coriolis force out of the initial plane, producing a toroidal component (α) effect (c). As the disc show differential rotation, i.e. is rotation faster for lower radii, line A is streched parallel to B (d), while they are still connected by the bubble forming a loop. This connection is then broken as the bubble radius expands to large distances, removing all flux associated with it.

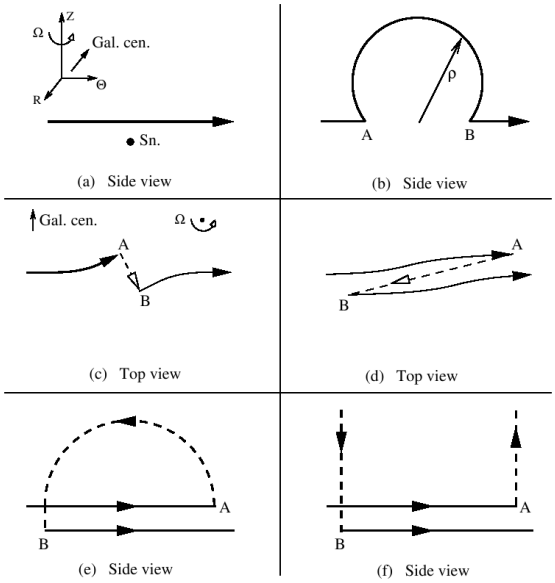

Figure 2.15: The $\alpha - \Omega$ dynamo in action [KZ07]

This theory allows the calculation of the α tensor from the spatial distribution and frequency of supernova explosions in a galaxy. Other important parameters are β and the escape velocity v_{esc}, which can be calculated as well.

Halo Fields

In starburst galaxies, which are of special interest for this work, X-Ray and galactic radio haloes indicate strong magnetic fields, driven by winds, not collimated AGN jets. These fields are considerably larger than one would suggest from the disc field, e.g. $50\,\mu$G [KWM88] in the halo compared to $10\,\mu$G in the disc. [BWO99] suggest an amplification mechanism for magnetic fields in winds, based on the Kelvin-Helmholtz fluid instability. This occurs at a boundary layer of two fluids, streaming at different velocities, when a disturbance mode becomes unstable. This depends on the density and the field in both fluids. The stability condition for the most stable geometry reads:

$$v_{rel}^2 \geq \frac{\rho^{(-)} + \rho^{(+)}}{4\pi\rho^{(-)}\rho^{(+)}} \left(B^{(-)2} + B^{(+)2} \right)$$

with (-) and (+) denoting the fluid, ρ the density, B the field and V_{rel} the relative velocity. [BWO99] show from the stability criterion, that for typical values in a starburst galaxy, KH instability must be expected. This is supported by numerical simulations. They find that the amplification depends on the ratio of magnetic to kinetic energy in fluid

and might contribute significantly to the cluster magnetic field by seeding in primeval dwarf galaxies [BWLK00].

2.5.2 Fields in Galaxies

A seed field might be generated by the Biermann battery effect on scales of galaxies or clusters. To understand how it works, we consider 2.15 and drop Ohmic and Hall term. For an absent magnetic field and a homogeneous electron density a pertubation in electron pressure then leads to an electric field. It is counterbalancing the force imposed by the pressure pertubation and static. An inhomogeneous electron density will lead to a current along the induced potential drop, as the electric field is not necessarily curl free anymore. The current will be tiny, so ion velocity and electron velocity are comparable $v_e = v_i$. The electron temperature will not differ much from the overall temperature : $p_e/n_e = p/n(1+\chi) = Mp/\rho(1+\chi)$, when the plasma is partially ionised, with χ is the degree of ionisation. The curl of 2.15 combined with the above relation, then leads an equation that is similar to generator equation for vorticity:

$$\frac{\partial \vec{B}}{\partial t} = \nabla\left(\vec{v} \times \vec{B}\right) + \frac{\nabla p \times \nabla \rho}{\rho^2} \frac{Mc}{e\,(1+\chi)}$$

As $e\vec{B}/Mc$ and $1(1+\chi)\omega$ satisfy the same equation and we can assume the same zero initial conditions, it follows, that vorticity and small magnetic fields are generated at the same time. These fields are in the order of $10^{-20}\,\mu$G.

Alternatively seed fields might be produced by nonhelical small-scale turbulence [19] in protogalaxies [KCOR97] or in first stars, which "pollute" their environment.

[19] One has to be careful combining turbulence and structure formation. Strictly speaking Kolmogorov turbulence is only defined in a system, where energy is injected at one scale, then propagates to smaller ones and is dissipated at the smallest. In structure formation, turbulent energy is injected at many different scale. For example, by cluster mergers, galaxy mergers and supernova winds. Therefore a Kolmogorov power law is not compulsory, but often assumed as to be justified by numerical simulations [KCOR97].

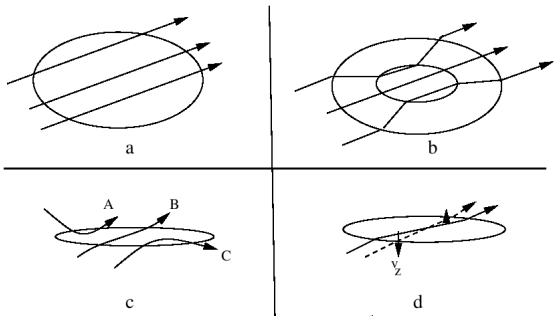

Figure 2.16: The evolution of a primordial field [HK97]

Primordial seed fields might produce similar fields, prior to the formation of first galaxies. Their formation process can then amplify the field: After seperating from Hubble expansion 2.5.2 (a) shows a uniform field in a protogalactic sphere [HK97]. When the sphere collapses, the field lines follow to a size of several 10s of kpc, but are still connected with the environment (b). The shrinking process leads to a disc field amplification of around 100. When the sphere collapses to the thin disc (c), another amplification factor of 100 is proposed. Components parallel to the disc are amplified by 10^4, perpendicular ones only by 100. (c) shows lines, that are entering and leaving the disc on the same side (A and C) and one (B) that is puncturing the disc. Because of flux freezing, only the former type of line can leave the disc. The latter field lines, are bound by clouds to the disc and can be amplified by the canonical dynamo.

As a conclusion we state, that initial seed fields must be provided by either inflation, Biermann battery or stars. These are then moderately amplified through turbulence in structure formation to microgauss range and correlation length around 1 kpc in the disc, where they can (but don't have to [KCOR97]) be sustained and amplified by the the $\alpha - \Omega$ Dynamo.

2.5.3 Fields in Clusters

In clusters the magnetic fields can either be a result of pollution by galactic outflows or be of primordial origin. For the latter class of theories, models include effects from symmetry breaking in the early universe and turbulence in a protogalactic environment. We will concentrate on the former models here, as the there is definite proof for a galaxy to cluster interaction, through metallicity observations in the Lyα forest of early clouds. We will describe in the next 2 sections, how the interaction of galactic outflows is modelled.

AGN Seeding

An *A*ctive *G*alactic *N*ucleus means an accreting compact object (most probably a massive black hole) in the center of a galaxy. AGN's are the most luminious objects in the universe and often show radio jets. These jets blow magnetised plasma into the cluster and therefore act similar to superwinds from galaxies. We present some aspects of their nature here, because AGNs may contribute significantly to the outflows from galaxies into clusters. The radio luminocity of the jet is connected to the magnetic energy in

a jet induced bubble. In a model by [FL01] the accretion with a black hole mass as a fraction of the halo mass and an universal lifetime at which the accretion emits radiation at the Eddington limit[20]. Then the luminocity in the B band is connected to the kinetic luminocity, which is known to be comparable the radio luminocity. After the quasar becomes dormand, its assumed, that the outflow material becomes more or less isotropic, forming a magnetised bubble of overdense, hot material. As the behaviour of magnetic fields in jets is not well understood, the magnetic energy in the bubble is assumed to be a fraction of the thermal energy This is proportional to luminocity and quasar activity $E_B = \epsilon E_K = L_k \tau_q$. The field geometry is highly unknown as well, so the field is assumed highly tangled and only its isotropic pressure is important. The equation of motion for the shell of the bubble consists then of pressure inside (thermal and magnetic) and outside the shell. Further gravity from Dark matter, shell and galaxy, dark energy and the drag force from the sweeping process. The thermal evolution includes radiative cooling, dissipation by inelastic collisions from shell and swept up medium, inverse Compton cooling and ionisation. 2 phases are considered: adiabatic evolution, if the bubble age is smaller than its cooling time, and radiative evolution if not. For the first one, dissipation is neglected, the latter one kinetic energy is converted to heat with a fraction of 0.8. The resulting maximum radius of the bubble depends only weakly on the enclosed energy $E_0 = \epsilon_k (1 + \epsilon_B) \tau_b M_h$.

The model predicts a cellular structure of the IGM, with highly magnetised bubbles from old quasar outflows. Radio Loud Quasars fill 20 % of the space before and 20 % after $z = 4$, while Radio Quiet BAL quasars might account for lower fields[21]. This process is not sensitive to the quasar lifetime. The filling at $z > 4$ results in much lower field strengths. There is only an upper limit imposed on the coherence length of the fields, as the model doesn't follow the field structure inside the bubbles. So the contraint on the upper limit is imposed by the bubble size. A typical bubble in the IGM is characterised by $B \approx 10^{-9}\,\mathrm{G}$, $R \approx 1\,\mathrm{Mpc}$, which results in very weak RM $\approx 3 \cdot 10^{-4}\,\mathrm{rad/m^2}$, even for a coherent field along the line of sight.

Superwind Seeding at high redshift

Another model to magnetise the IGM is based on outflows by galactic winds (e.g. [KLH99]). From the hierarchy in bottom-up structure formation follows, that the universe was populated by a large number of dwarf galaxies for redshifts $z \leq 8$. Because of their small potential well and the high rate of mergers / interactions at that time, these dwarf galaxies will often be starbursting. The resulting galactic winds from short living low metallicity stars can form galactic superwinds, which become large enough to transport magnetic fields into the IGM. Faraday RM oberservations of quasars up

[20] The Eddington is the flux, when radiation pressure equals gravitation, and defines the upper limit for gravitational induced radiative processes.

[21] Note that neither high redshift RLQ's nor BAL's are observed well up to today.

to $z = 2.5$ indicate an upper limit of $B_{IGM} \leq 10^{-9}$ G for Mpc scales. Good examples in the local universe for starbursting dwarfs are M82, NGC 1569 and NGC 4666. In M82 an X-Ray and radio halos together with wind velocities of several 1000 km/s and ordered magnetic fields of $B \geq 10\,\mu$G are observed. These are expelled by the galaxy in starburst events, which happen every 100 Myr, lasting for several 10 Myr. The outflow theory is supported by the absence of a correlation of galaxy mass to starburst intensity (galaxy rotation speed to bolometric IR luminocity). It follows, that about every galaxy has undergone a phase of starburst activity, including strong mass loss by winds.

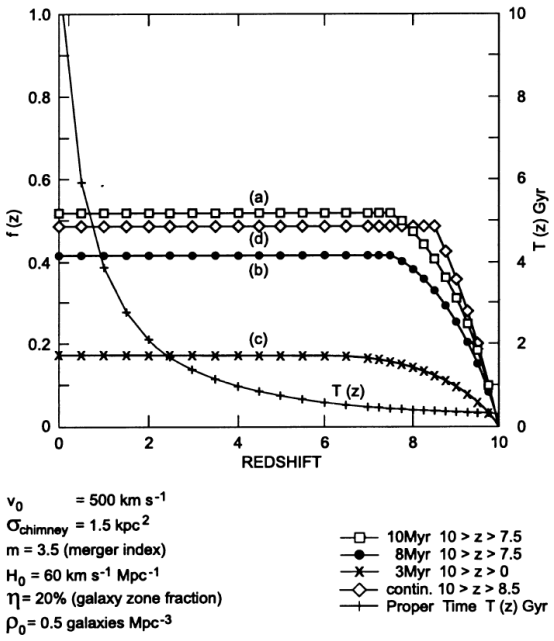

Figure 2.17: Fraction of IGM filled by superwinds over redshift. [KLH99]

The model in [KLH99] is based on seeding by spheriodal and elliptical(dSph, dE) dwarfs. These are more abundant than heavier, irregular dwarf galaxies in the early universe. [Gre97] find old and medium age stellar populations in all LG dwarf galaxies. They deduce a phase of high star formation 10 Gyrs ago. The density of small dwarfs in the early universe must be incomplete in surveys, as they lie at low brighness end. This is corrected by combining several near complete surveys of the local group. To obtain a smoothed out local number density of dwarf galaxies, they group dwarfs around large galaxies, assume spherical symmetry and calculate an average radius. To this, the average number of dwarf galaxies between groups is added. The best fit is the 0.75 dwarfs per Mpc^{-3}.

The outflow volume is modeled by assigning a comoving, spherical volume to each galaxy. Its radius is then half the distance to the next galaxy. When 2 galaxies merge, their spheres merge as well; the merger rate is assumed to depend on redshift as $(1+z)^{3.5\pm1}$. The sum of all spheres (V_A) is the available volume for filling. With the outflow volume (V_F) the filled fraction of the IGM becomes: $f(z) = V_F/VA$. The wind outflow is parametrised by cross section σ, velocity v_0 and time τ: $V_F = v_0\sigma\tau$. Figure 2.17 shows f(z) over redshift for different conservative outflow lengths and frequencies. The fractions show, that the IGM can be filled with fields by an variety of models. Further the models suggest, that seeding before $z \approx 7$ is most effective.

3 Numerics and Code

How does the universe fit into a computer ? Classically speaking every particle in the universe follows the Boltzmann equation coupled to the various fields like gravitation and electromagnetism. As allready stated in chapter 2.3 it is not feasible to compute its solution. The fluid approximation reduces this problem to the computation of macroscopic quantities of flowing matter.
Limited resources force us to discretise the flow in either mass or space. This corresponds to either, solving the fluid equations on a grid or using particles. The code uses the latter way, which is described in the first chapter.

The second chapter gives a brief overview of the postprocessing software used. Here we have to define what a Dark Matter halo or a galaxy is in our simulation and how observable quantities are represented in the computer.

The last chapter documents the IDL code used to modify the simulations, by implementing the seed model.

3.1 Methods In GADGET-2

The Code used for our cosmological simulations is GADGET-2 [Spr05], SVN build 2022, which is public available. GADGET-2 describes a flow by a set of randomly distributed particles, similar to a Monte Carlo sampling of the phase space of the Boltzmann equation. It uses a combination of techniques to compute the gravitational force and solve the MHD equations. Resembling the two "kinds" of matter in the universe, collisional and non-collisional, its uses two types of particles to follow the Dark Matter / gas flow respectively.

In this section we describe characteric features of the code: How the gravitational force is computed for Dark Matter particles. Magnetohydrodynamics is followed for the gas particles using an entropy conserving SPH method. The time stepping is done using a symplectic[1] leap-frog scheme. We describe the MHD implementation, especially how it deals with the divergence of the field. At last, we show results from a test run of a MHD shock tube and the setup of initial conditions.

Many people extended GADGET-2, so that it is capable of modeling e.g. star formation, Dark Energy and cooling as well. We don't use these capabilities, but concentrate

[1] phase-space conserving

on a MHD gas flow and a non collisional, gravitational interacting Dark Matter flow.

3.1.1 Gravitation

In cosmological simulations, gravitation is dominated by the representation of Dark Matter. GADGET-2 is a N-body code, i.e. it discretises mass so the flow is represented by a number of particles. These particles follow a Hamiltonian governing Newtons gravitational potential. Through the interaction potential ϕ it is coupled to the Poisson equation:

$$H = \sum_i \frac{\vec{p}_i^2}{2m_i a(t)^2} + \frac{1}{2}\sum_{ij} \frac{m_i m_j \phi(\vec{x}_i - \vec{x}_j)}{a(t)} \tag{3.1}$$

$$\nabla^2\phi(\vec{x}) = 4\pi G\left(-\frac{1}{L^3} + \sum_n \bar{\delta}(\vec{x} - \vec{n}L)\right) \tag{3.2}$$

with $\vec{p}_i = a^2 m_i \dot{\vec{x}}_i$ the canonical momenta to the comoving coordinate vectors $\vec{x}$, $a(t)$ the expansion factor of a box with length L and periodical boundary conditions. $\bar{\delta}$ is the dirac δ-function convolved with the spline SPH kernel (see 3.1.3), with a softening length of ϵ.

For a naive solution of the problem, the computational cost scales as N^2, when N is the number of particles, because, gravitation affects every particle.

GADGET uses 2 different methods to compute the gravitational force on a particle. This reduces the computational cost trastically, without affecting accuracy too much.

The PM method calculates the gravitational potential in every point of a grid. The force is then found by $\vec{F} = \nabla\phi(\vec{x})$.
The first step after defining a grid (cellsize h^3), is to map all particles to it, i.e. assigning a density to every gridpoint. In the simplest case, every particle contributes to the closest gridpoint. This has the disadvantage of a discontinous force: When the particle is shifted from one gridpoint to another during time evolution, the resulting force "jumps" as the particle crosses the midpoint of the cell. For a better approximation the particles a smoothed out over two cells. The density can then be written as:

$$\rho_m = \frac{1}{h^3}\sum_i m_i W(\vec{x}_i - x_m)$$

where $W(x_m - x_i)$ is the weighting function at a gridpoint x_m and a particle coordinate x_i.
The solution of the Poisson equation can be found using Greens functions ($g(\vec{x} - \vec{x}_i)$), In fourier space this corresponds to a multiplication, therefore the potential is found after

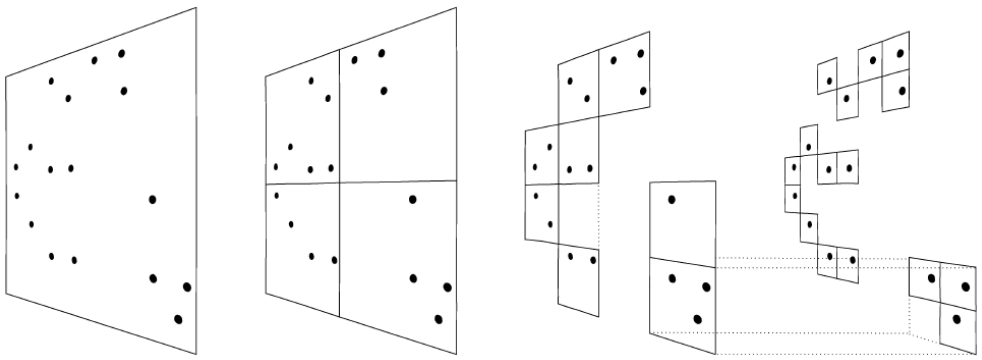

Figure 3.1: Recursive subdivision of space into nodes [SYW01]

a discrete FFT:

$$\vec{\phi}(\vec{x}) = \int g(\vec{x} - \vec{x}')\rho(\vec{x})\, d\vec{x}' \qquad \hat{\phi}(\vec{k}) = \hat{g}(\vec{k}) \cdot \hat{\rho}(\vec{k}) \tag{3.3}$$

The gravitational potential on the grid is then transformed into coordinate space, where the force at the gridpoints can be found from finite difference methods. The force at the particle position is back interpolated by the weighting function:

$$f^{(x)}_{i,j,k} = -\frac{\phi_{i+1,j,k} - \phi_{i-1,j,k}}{2h} \qquad \vec{f}(\vec{x_i}) = \sum_m W(\vec{x}_i - x_m)$$

This method scales with $N + N_{grid}\log(N_{grid})$ with N, N_{grid} the number of particles or grid points respectively. It is very fast, as it relies of Fourier transforms, but its resolution is limited by the number of gridpoints to be stored in memory. Using adaptive mesh refinement schemes it is possible to extend the range of covered resolutions without using too much memory. In cosmological simulations, where a very high resolution is needed in objects like clusters, but not feaseble in voids Particle Mesh is often used for the long range part of the potential. GADGET-2 splits it in fourier space $\phi_{\vec{k}} = \phi^{long}_{\vec{k}} + \phi^{short}_{\vec{k}}$, characterising the split by a spatial scale r_s so that:

$$\phi^{long}_{\vec{k}} = \phi_{\vec{k}} \exp\left(-\vec{k}^2 r_s^2\right) \qquad \phi^{short}(\vec{x}) = -G\sum_i \frac{m_i}{r_i}\left(\frac{r_i}{2r_s}\right) \tag{3.4}$$

the short range potential is given by the second equation above. It is calculated by a more accurate method.

The Tree Algorithm corresponds to a hierarchical multipol expansion of the gravitational force. Space is split into 8 cubes as shown in 3.1.1. This is done recursively, until

every cube contains only one particle. For every cube in every hierarchy, the volume and the number of contained particles is known, so that its average density can easily be calculated. The force on one particle can be obtained by "walking" the tree. Starting from the root node for every node on every hierarchy a criterium decides if the force from the particular node is accurate enough to be used. If this is not the case, the node is opened and the criterium is applied to the 8 daughter nodes until it is matched. The force is the calculated as the sum over all cubes treated as monopoles.

The opening criterium controls the accuracy of the force, and is mostly an angle argument: If the node is far away and small enough, its solid angle is small, so the force of all particles contained in the node is accurately described by its monopole. For a closer node the angle becomes larger, and the node has to be opened / subdevided to make the monopole approximation accurate enough.

The tree algorithm scales roughly as $N \log(N)$ and has the advantage of being unsensitive to clustering of particles. GADGET uses its for the short range potential and a PM algorithm for the longe range. The force decomposition is show in 3.2.

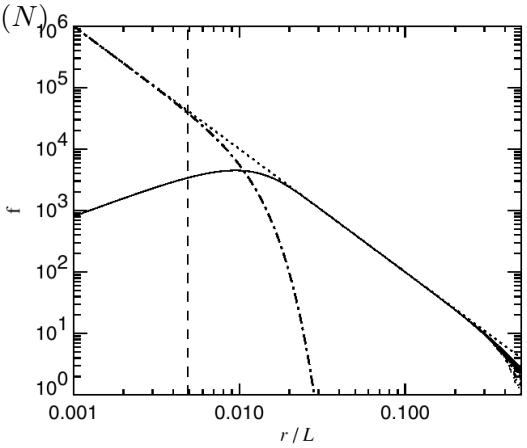

Figure 3.2: Force decomposition in GADGET-2 [Spr05]

Further more GADGET-2 parametrises the particle position not by a 2 dimensional vector, but a coordinate on a Peano-Hilbert curve. These "space filling[2]" curves, similar to a fractal curve. This has the advantage of arranging the particle data in the cache memory ordered by distance. It allows a high amount of cache-hits, when walking the tree, as close nodes are in the cache. The CPU does not need to fetch data from the slower main memory of the system.

3.1.2 Time Stepping

To integrate 3.1 over time, GADGET-2 uses a leapfrog technique, with adaptive timesteps. For a given force $\vec{F}(\vec{x})$, this scheme calculates the new particle position for a finite

[2] That means, they can be refined recursively to "touch" every point in space. Here the curve is refined, until it touches every leaf of the tree.

timestep Δt from velocities obtain between the positions:

$$\vec{v}_{n+1/2} = \vec{v}_n + \vec{F}(\vec{x}_n)\Delta t/2$$
$$\vec{x}_{n+1/2} = \vec{x}_n + \vec{v}_{n+1/2})\Delta t/2$$
$$\vec{v}_{n+1} = \vec{x}_{n+1/2} + \vec{F}(\vec{x}_n)\Delta t/2$$

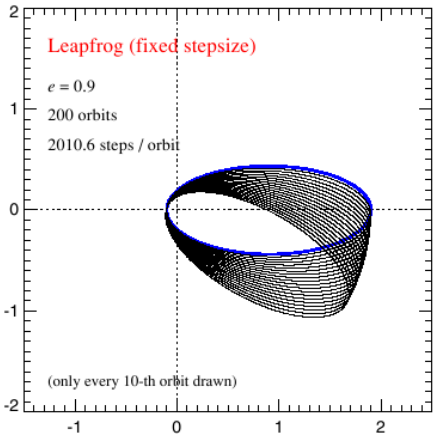

Figure 3.3: Symplectic leapfrog scheme [Spr05]

The leapfrog method has the advantage of being *symplectic*. It conserves the symplectic 2-From in the phase space of the Hamiltonian of the system 3.1. What does that mean ?
Similar to quantum mechanics, the time evolution of $H = H_{kin} + H_{pot}$ can be described by the time evolution operator $U(\Delta t)$, which evolves the system in time, when it acts on the Hamiltonian. A "step" in time, i.e. applying $U(\Delta t)$, imposes a canonical transformation of the particle coordinates in phase space. The volume in phase space is conserved during this, the transformation is called symplectic. Taking only the first (kinetic) or the second (potential) part of the Hamiltonian above, $U(\Delta t)$ is easily computed analytically [Spr05]. The time evolution is then equal to a "Drift": $H = H_{kin} \Rightarrow U(\Delta t) = D_t(\Delta t)$ or a "Kick": $H = H_{pot} \Rightarrow U(\Delta t) = K_t(\Delta t)$. A numerical integration scheme, approximates the time evolution, and therefore approximates the time evolution operator $U(\Delta t)$. It can be shown, that the leapfrog integrator above approximates the time evolution as:

$$\bar{U}(\Delta t) = K\left(\frac{\Delta t}{2}\right) D\left(\Delta t\right) K\left(\frac{\Delta t}{2}\right)$$

This is important, because this integrator does not perturb the Hamiltonian and manifestly conserves energy using only a single force evaluation. The introduced error is not a result of a forbidden transformation of the system, but the associated Hamiltonian, that differs from the physical one by the order of Δt^4. The figures 3.3 and 3.4 show the Kepler problem integrated by the leapfrog and the 4th order Runge-Kutta scheme. The latter one gives much worse results: it is not energy conserving, as the ellipse gets smaller, while the former method keeps the area constant. Its long term evolution is more stable, at lower computational cost.

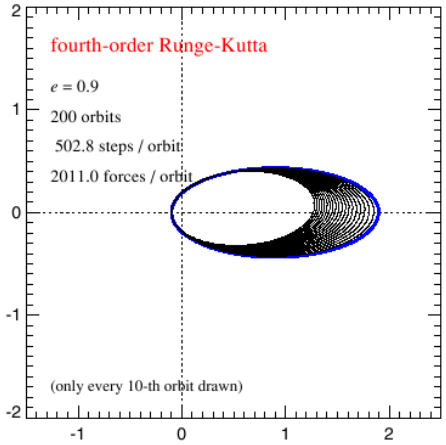

Figure 3.4: 4th order Runge Kutta [Spr05]

In cosmological simulations high spatial differences in density are found in voids compared to clusters. It requires the use of individual and adaptive timesteps for every particle, as it is done in GADGET-2. This breaks the symplectic properties of the integrator, as the gravitational potential is a two particle force. I.e. it is not possible to "kick" only some particles, "drift" others with a canonical transformation. GADGET-2 approximates the force by splitting the potential in a short-range and a long-range part (see 3.1.1) and subcycling over short range force, while the long range potential is kept constant (Figure 3.1.2). It can then be argued, that the resulting force accuracy is comparable to a symplectic integration scheme, because in voids, two particle interactions are negligible and the particles move in a collective potential.
The variable timesteps for different particles introduces a time variable error in the Hamiltonian 3.1 and therefore long time stability of the algorithm is lost. An investigation of the Kepler problem with variable timesteps shows, that the DKD scheme performs much worse the KDK scheme. This is because the time asymmetry is twice as large in the former case. The criterium to choose the length of a timestep, is closely related to the speed information can be transfered with. For collisionless particles, GADGET-2 uses the former in:

$$\delta t_{grav} = min\left(\Delta t_{max}, \sqrt{\frac{2\eta\epsilon}{|a|}}\right) \qquad \Delta t_i^{\text{hyd}} = \frac{C_{Courant} h_i}{max\left(v_{ij}^{sig}\right)} \tag{3.5}$$

The latter case in 3.5 is used for collisional SPH particles and is closely related to the fastes magnetic wave, and the viscosity of the fluid.

3.1.3 MHD In SPH

To treat the dynamics of the Baryons, our version of GADGET-2 features an implentation of Magnetohydrodynamics using the SPH[3] formalism. SPH uses a particle aproach to sample the flow in phase space similar to a Monte Carlo method. It is then possible to approximate the MHD differential equations by a set of coupled equations.

The SPH Principle is to use local averages to assign physical properties to randomly distributed particles. If $A(\vec{r})$ is a property of an MHD flow then we can expand a delta

[3] Smooth Particle Hydrodynamics [GM77]

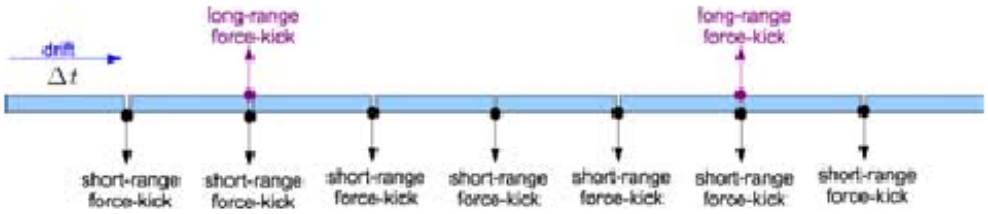

Figure 3.5: Principle of the DKD time evolution scheme, with adaptive timesteps. The whole systems is drifted every time. Short range kicks are done in highly dynamical regions like clusters and correspond to the tree force. Long range kicks are computed by the PM algorithm and correspond to voids in the cosmological density field. [Spr05]

function to write its local average as:

$$A(\vec{r}) = \int d^3r' A(\vec{r}')\,\delta(\vec{r}-\vec{r}') \qquad \langle A(\vec{r})\rangle = \int d^3r' A(\vec{r}')\,W(\vec{r}-\vec{r}',h)$$

The expanded δ-function $W(\vec{r}-\vec{r}',h)$ is called "kernel" and of central importance. h is called the *smoothing length*, defining the typical length scale on which the $A(\vec{r})$ is averaged over, or smoothed out. Often instead of h, the number of neighbours n is defined, which define a physical quantity by averaging. Note that while the first equation is always true, the latter one requires the kernel to fullfill the properties of the delta function :

$$\int d^3r' W(\vec{r}-\vec{r}',h) = 1 \qquad \lim_{h\to 0}(\vec{r}-\vec{r}',h) = \delta(\vec{r}-\vec{r}')$$

The kernel used in GADGET-2 is a kubic spline, see [Spr05] for the exact form.

Using a kernel function constitutes a big simplification, because only the kernel carries a spatial coordinate. Therefore every gradient in the MHD equations acts only on the kernel, whose derivative is known. This transforms the MHD equations 2.16 into a system of coupled equations, easier to solve.

SPH derivatives are formulated symmetric. A quick look at the naive derivative:

$$\nabla\langle A_i\rangle = \sum_j \frac{m_j}{\rho_j} A_j \nabla_i W(\vec{x}_i - \vec{x}_j, h)$$

reveals, that it is not symmetric under particle switch, because, the density ρ is particle dependent[4]. But a non symmetric derivative will manifestly break the conservation laws

[4] Setting $A_i = \rho_i$ gives: $\langle\rho_i\rangle = \sum_j m_j W(\vec{x}_i - \vec{x}_j, h)$

in the MHD equations. There are several ways to define symmetric derivatives through vector identities:

$$(\rho\nabla)\cdot A = \nabla(\rho\cdot A) - \rho\cdot(\nabla A) \quad \Longrightarrow \quad \nabla\langle A_i\rangle = \frac{1}{\rho_i}\sum_i m_j (A_j - A_i)\nabla_i W_{ij,h}$$

$$\frac{\nabla A}{\rho} = \nabla\left(\frac{A}{\rho}\right) + \frac{A}{\rho^2}\nabla\rho \quad \Longrightarrow \quad \nabla\langle A_i\rangle = \rho_i \sum_j m_j \left(\frac{A_j}{\rho_j^2} + \frac{A_i}{\rho_i^2}\right)\nabla_i W_{ij,h}$$

which one is used, depends on the SPH equation to symmetrise.

Similar to the derivatives, for an variable smoothing length h_i the SPH kernel interaction must be symmetrised as well. This is either done by averaging both smoothing lengths or the kernel themselves. The latter version implemented, because it appears more stable: $\bar{W}_{ij} = 0.5(W(|r_{ij}|, h_i) + W(|r_{ij}|, h_j))$

The GADGET Implentation of MHD-SPH can be understood in terms of the ideal MHD equations 2.16 using the symmetrised derivatives mentioned above. It helps to consider:

1. As SPH is a Lagrangian scheme, the continuity equation is manifestly fullfilled.

2. Gravity is calculated using the TreePM method. Therefore the gravity term in the force equation of 2.16 is not considered.

3. The assumption of an equation of state of an ideal gas, renders the internal energy equation obsolete. The pressure is then given by : $P_i = A_i\rho_i^\gamma$ where A_i is the entropic function. The internal energy can by recovered by: $u_i = \frac{A_i}{\gamma-1}\rho_i^{\gamma-1}$. The adiabatix index is $\gamma = 5/3$.

4. Shocks are treated via an artificial viscosity Π_{ij}, that convertes kinetic energy into entropy (heat). It is defined[5] as

$$\Pi_{ij} = \frac{-0.5\alpha v_{ij}^{sig}\mu_{ij}}{\rho_{ij}} f_{ij}^{shear}$$

   for $\vec{r}_{ij}\cdot\vec{v}_{ij} \leq 0$ and $\Pi_{ij} = 0$ otherwise. I.e. is only active for particles approaching each other.

5. GADGET-2 uses an entropy conserving formulation of SPH. This is motivated by the fact, that for a given number of neighbours, the smoothing length is not well

[5] Using $\mu_{ij} = \vec{v}_{ij}\cdot\vec{r}_{ij}/r_{ij}$ the relative velocity along the seperation vector, $v_{ij}^{sig} = c_i + c_j - 3\mu_{ij}$ the signal velocity, $c_i = \sqrt{_i/\rho_i}$ the sound velocity and f_{ij}^{shear} the shear viscosity delimiter, that supresses viscosity in strong shear flows

defined. This corresponds to an additional degree of freedom in Lagrangian of the fluid [SH02]. Constraining the Lagrangian, so that the kernel volume contains a constant mass:

$$\phi_i(\vec{q}) = \frac{4\pi}{3} h_i^3 \rho_i - n m_i = 0$$

unambigously defines an individual smoothing length h_i for every number of neighbours n.

From the Euler-Lagrange equations with the Lagrange multiplicator defined above, the first term in the force equation 2.17 follows as:

$$\left(\frac{\mathrm{d}\vec{v}_i}{\mathrm{d}t}\right)_{\mathrm{P}} = -\sum_{j=1}^{N} m_j \left[f_i^{co} \frac{P_i}{\rho_i^2} \vec{\nabla}_i W_{ij}(h_i) + f_j^{co} \frac{P_j}{\rho_j^2} \vec{\nabla}_i W_{ij}(h_j) \right] \tag{3.6}$$

$$f_i^{co} = \left[1 + \frac{h_i}{3\rho_i} \frac{\partial \rho_i}{\partial h_i} \right]^{-1} \tag{3.7}$$

In addition the viscous force is implemented as:

$$\left(\frac{\mathrm{d}v_i}{\mathrm{d}t}\right)_{\Pi} = -\sum_{j=1}^{N} m_j \Pi_{ij} \nabla_i \bar{W}_{ij} \tag{3.8}$$

The magnetic part of the force equation is written using the Maxwell tensor M_i^{kl}. For this a force corrsponding to magnetic monopoles has to be added, and is later subtracted again. In components, with $u = r/h$:

$$\left(\frac{\mathrm{d}\vec{v}_i^k}{\mathrm{d}t}\right)_{\mathrm{B}} = a^{3\gamma} \frac{1}{\mu_0} \sum_{j=1}^{N} m_j \left[f_i^{co} \frac{M_i^{kl}}{\rho_i^2} + \frac{\partial W_i}{\partial u} \frac{\vec{r}_{ij}^{\,l}}{|\vec{u}_{ij}|} f_j^{co} \frac{M_j^{kl}}{\rho_j^2} \frac{\partial W_j}{\partial u} \frac{\vec{r}_{ij}^{\,l}}{|\vec{r}_{ij}|} \right] \tag{3.9}$$

$$\left(\frac{\mathrm{d}\vec{v}_i^k}{\mathrm{d}t}\right)_{\mathrm{divB}} = a^{3\gamma} \frac{\vec{B}_i^k}{\mu_0} \sum_{j=1}^{N} m_j \left[f_i^{co} \frac{\vec{B}_i^l}{\rho_i^2} \frac{\partial W_i}{\partial u} \frac{\vec{r}_{ij}^{\,l}}{|\vec{r}_{ij}|} + f_j^{co} \frac{\vec{B}_j^l}{\rho_j^2} \frac{\partial W_j}{\partial u} \frac{\vec{r}_{ij}^{\,l}}{|\vec{r}_{ij}|} \right] \tag{3.10}$$

$$M_i^{kl} = \left(\vec{B}_i^k \vec{B}_i^l - \frac{1}{2} |\vec{B}_i|^2 \delta^{kl} \right) \tag{3.11}$$

The force equation is then :

$$\frac{\mathrm{d}\vec{v}}{\mathrm{d}t} = \left(\frac{\mathrm{d}\vec{v}_i}{\mathrm{d}t}\right)_{\mathrm{P}} + \left(\frac{\mathrm{d}\vec{v}_i}{\mathrm{d}t}\right)_{\mathrm{Grav}} + \left(\frac{\mathrm{d}v_i}{\mathrm{d}t}\right)_{\Pi} + \left(\frac{\mathrm{d}\vec{v}_i^k}{\mathrm{d}t}\right)_{\mathrm{B}} - \left(\frac{\mathrm{d}\vec{v}_i^k}{\mathrm{d}t}\right)_{\mathrm{divB}}$$

As written above, for an ideal gas, the internal energy equation is not needed. Still we have to evolve the entropic function A_i in time, to capture shocks properly:

$$\frac{\mathrm{d}A_i}{\mathrm{d}t} = \frac{1}{2} \frac{\gamma - 1}{\rho_i^{\gamma - 1}} \sum_{j=1}^{N} m_j \Pi_{ij} \vec{v}_{ij} \cdot \nabla_i \bar{W}_{ij} \tag{3.12}$$

The last equation to consider is the induction equation, which can be written, using a vector identity, as:

$$\frac{\mathrm{d}B_i^k}{\mathrm{d}t} = \frac{1}{Ha^2}\frac{f_i^{co}}{\rho_i}\left[\sum_{j=1}^{N} m_j(v_{ij}^k B_i^l - B_i^k v_{ij}^l)\frac{\partial W_i}{\partial u}\frac{\vec{r}_{ij}^{\,l}}{|\vec{r}_{ij}|}\right] - 2\vec{B}_i \tag{3.13}$$

For every timestep, the code loops over every particle, takes the neighbours into account and calculates the individual forces.

Smoothing

Shock tube tests of the SPH codes modelling MHD show relatively high numerical noise in the vicinity of disontinuities, i.e. shocks. The noise corresponds to fields reversals on the smallest scales, e.g. two particles close to each other with opposite field vectors. It is common, to use a smoothing technique to reduce the noise near shocks. As its used only on scales of the kernel, below the effective resolution of the simulation, no useful information is removed. Still the magnetic energy associated with the field get lost, so energy conservation is violated. This is not critical in our case, as the fields are far too small, so the magnetic energy in sub scales does not contribute significantly compared to kinetic energy.

For the smoothing, a new magnetic field is constructed as the linear combination of the old and a smoothed field:

$$\vec{B}_i^{new} = q\left\langle\vec{B}\right\rangle_i + (1-q)\,\vec{B}_i^{old} \tag{3.14}$$

$$\left\langle\vec{B}\right\rangle_i = \frac{\sum_j\left(m_j\vec{B}_j/\rho_j\right)W_{ij}}{\sum_j\left(m_j/\rho_j\right)W_{ij}} \tag{3.15}$$

q is a free parameter here and is set $q = 1$ in our simulations. The field is smoothed every 15 timesteps.

MHD Shock Tube

To demonstrate the numerical validity of the code, we calculated a shock tube. The initial conditions were set up as a periodic box containing 78750 particles, where one half contains 8 times more particles than the other one: $8\cdot\rho_l = \rho_r = 1$, $10\cdot P_l = P_r = 1$, a magnetic field of $B_x^{l,r} = 0.75$, $B_y^r = 1$, $B_y^l = -1$, $\vec{v} = \vec{0}$ and an adiabatic index of 5/3. This setup follows the slow rarefraction test in [RJ95]. At $x = 70$ there is contact discontinuity, from which a shocks evolves into negative x-direction. The turbulent motion of the flow increases the magnetic field, which features several discontinueties moving into both directions.

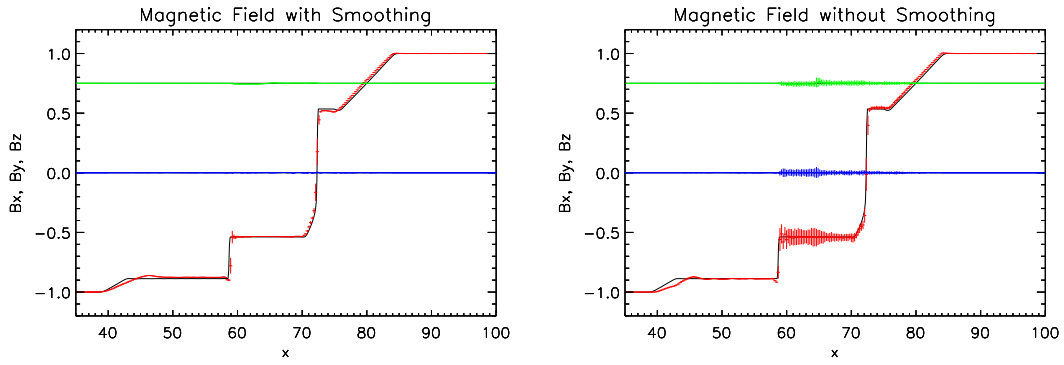

Figure 3.6: Magnetic field ($(B_X, B_Y, B_Z) \leftrightarrow$ (green, red, blue)) in a simulated shock tube with and without smoothing. The particles are binned by 0.5 times the maximum smoothing length. The error bar represent the standard deviations (1σ). The black line are the results of a calculation using the freely available gridcode "ATHENA"

We want to focus here on the effect of magnetic smoothing described above. Figure 3.1.3 shows magnetic field in the shock tube with and without smoothing. It is obvious, that smoothing reduces particle oscillations at discontinuities in the field. The standard deviation at the jumps of the field strength in y direction is vastly reduced. See Appendix A.2.4 for plots of density and velocity.

Initial Conditions

All our runs started at a snapshot[6] from the simulations done by [DGST05]. They start with an constant magnetic field at redshift $z = 10$ using constrained initial conditions. These are modified to resemble the structure of the local universe. As a result, it is possible to identify observed structures like the Virgo and Coma superclusters in their and our simulations.

These initial conditions are based on the IRAS 1.2-Jy survey by [FHS+95]. The survey galaxies within a sphere of 12000 km/s are smoothed by a gaussian with $5\,h^{-1}$Mpc dispersion. Not observed regions can then be interpolated, because of the large smoothing length. The rms overdensity of this field is scaled to the one of the smoothed linear power spectrum today. Using the Zeldovich approximation the field is evolved backwards in time to $z = 50$. From this a new field is constructed from Gaussian fluctuations, whose amplitude follows the former one and is in agreement with the appropiately smoothed theoretical power spectrum.
With this power spectrum, a displacement field on a grid can be constructed from the

[6] outputfile number 8 at $z \approx 4.6$

spectrum. For higher frequencies the theoretical spectrum is used to set up another displacement field. These are interpolated on unpertubed particles of a glass file. For the high resolution regions the sum of both is used, while for lower resolutions, the constrained one is accurate enough. For a more detailed description please refer to [MLS+02]

3.2 Postprocessing

To close this section, we describe how a halo is defined and then found in a simulation. Per definition a (dark matter) halo is locally overdense region, which is gravitationally bound. The postprocessing has then to find the every particle belonging to the overdense region and identify the substructure inside that region, which is the more difficult task. We apply a FoF find first and then use the Subfind algorithm described below, to find substructure. In a final step all haloes of all snapshots/redshifts and their properties are combined in and IDL tree like structure.

The Friend of Friend Algorithm

In dark matter simulations, haloes are usually identified using the Friend-of-Friend algorithm. Particles are belonging together, if their spatial seperation is less than a previously defined linking length $b \approx 0.2$. All particles connected like that, belong to a group. This corresponds to isodensity contours of $\rho \propto 1/b^3$ over the background.

The FoF algorithm works sufficiently reliable and fast, but often connects haloes with thin particle "bridges" and is unable to detect substructure in a halo.

The Subfind Algorithm

On the basis of Friend-of-Friend groups, SUBFIND identifies gravitationally bound particles and substructure within large haloes. By taking only gravitiationally bound particles, the FoF bridges are excluded from the groups.
Substructure is indentified by lowering a density threshold and identifing "saddle point particles", which lie between to local maxima. To do this all particles contained in a halo are sorted according to their density. The distribution is then rebuild, by considering particles in decreasing order. For every particle a those SPH neighbours are selected which have larger density than the particle. The two spatially closest neighbours, lets call their group B, can then be:

- not existing ($B = \emptyset$). It follows the particle is a local maximum and defines a new substructure.
- only one particle ($|B| = 1$). Or are from the same substructure. Then the original particle a is associated with this structure.

- part of two different substructures. Then particle a is resembles a saddle point, and the two subgroups are marked as candidates. They are then joined and the particle is added to the new group.

Using this algorithm every particle is sorted into into a hierachical tree of sub and subsubstructures. These are unbount by deleting all gravitationally not bound particles. A much more detailed description can be found in [SWTK01].

4 Seed Model

The magnetic field in early dwarf galaxies and their winds, was not accurately measured yet. Therefore we need to extrapolate from measurements of starburst galaxies in the local universe, assuming starbursting dwarf galaxies today are sufficiently similar to those at high redshift. Still the wind up to distances much larger than the numerical resolution needs to be modeled, as there are no well established values its magnetic field as well. For most of the model parameters we use M82 as a reference point. The only exception is the field in the galactic disc, which is the most important parameter in the model. We test several values, found by different authors.

In the first section we describe the model used to estimate the magnetic winds in high redshift dwarf galaxies. The following part deals with the parameter values. The last two parts of this chapter describe the dipole and quadrupole field structure implented.

4.1 The Magnetic Fields In Galactic Winds

Starburst galaxies show big outflows of plasma, which are thought to feed the intra cluster medium with metalls and magnetic fields, frozen into the gas. These winds are driven by the star formation processes inside the (dwarf-)galaxy, therefore its velocity and mass are connected to the star formation in the galaxy [SMS05]. During the starburst, the turbulence induced by galaxy-galaxy interaction, accelerates the formation process, producing a large number of heavy O and B stars. Due to their short live time, the resulting supernovas quickly feed galactic winds, with velocities of up to several thousand kilometers per second. The winds drive gas from the disc into the intra cluster medium, filling it with metals and magnetc fields.

The wind model by [BVE06] provides a discription of the time evolution of the magnetic energy E_B contained in a spherical wind bubble centered on a galaxy.
We assume the bubble to be filled with a constant field within a radius R_0 at the beginning, calculating it's energy by:

$$E_0 = \frac{B_w^2}{8\pi}\frac{4\pi}{3}R_0^3$$

For the wind kinematics [BVE06] assume two different phases of wind evolution — Sedov-Taylor and the momentum driven "snowplow" phase —, but treat the magnetic

field the same in both cases. As we are interested in the field only, we don't follow their rather complicated kinematics. Instead, the wind radius, and therefore the wind volume V_w is calculated from the wind velocity v_w [1] :

$$V_w = \frac{4\pi}{3} v_w^3 \cdot t^3 \qquad\qquad v_w = 320\sqrt{2} \cdot \dot{M}_\bigstar^{0.145}\,\mathrm{km/s}$$

This follows [SMS05] with an ISM constant of $K = 0.5$.
As the wind evolves isotropic, it contains an average magnetic field B_w. It is driven by the star formation in the center of the galaxy, $\dot{M}_\bigstar$, which injects magnetic energy at a rate $\dot{E}_{B_{in}}$ into the bubble. Due to adiabatic expansion, the field energy decreases proportional to the change in volume[2]:

$$\frac{d}{dt} E_B = \dot{E}_{b_{in}} - \frac{1}{3}\frac{\dot{V}_w}{V_w} E_B \tag{4.1}$$

$$= \dot{E}_{b_{in}} - \frac{1}{t} E_B \tag{4.2}$$

with $\dot{V}_w$ the change of the wind volume due to expansion. The wind magnetic field is modelled with average magnetic energy $\epsilon_{B_{in}}$ and mass density $\bar{\rho}_{in}$, so for the injection rate $\dot{E}_{b_{in}}$ it follows :

$$\dot{E}_{B_{in}} = \epsilon_{B_{in}} \cdot \dot{V}_{in}$$
$$= \epsilon_{B_{in}} \frac{\dot{M}_w}{\bar{\rho_{in}}}$$

The injected mass rate $\dot{M}_w$ is again estimated through the star formation rate [SMS05]:

$$\dot{M}_w = 2.5 \dot{M}_\bigstar^{0.71}\,\mathrm{M_\odot/yr}$$

With this the average injected mass density, is estimated by the mass blown trough a spherical surface of galactic radius $R_g = \frac{R_{200}}{10}$ at the wind velocity v_w:

$$\bar{\rho}_{in} = \frac{\dot{M}_w}{4\pi R_g^2 v_w}$$

As the halo is often identified as substructure of a parent halo in the simulation, R_200 is not always available. We use a fit of R_Crit200 to M_Crit200 to estimate it as $R_G \approx \exp\left(0.347144 \cdot \ln\left(M_{ISM}\right) + 3.47887\right)$ with $\chi^2 = 347$ due to resolution effects.

[1] It's also possible to scale the wind velocity found in M82 ($\approx 4000\,\mathrm{km/s}$) to the simulation halo, e.g by mass. Still both velocities are large enough to seed the complete halo, i.e. all particles, in reasonable star burst times. We therefore use the more conservative / smaller one, estimated from $\dot{M}_\bigstar$

[2] [BVE06] deduce this by neglecting the shear amplification term in the induction equation, when they consider a magnetic bubble expanding isotropically.

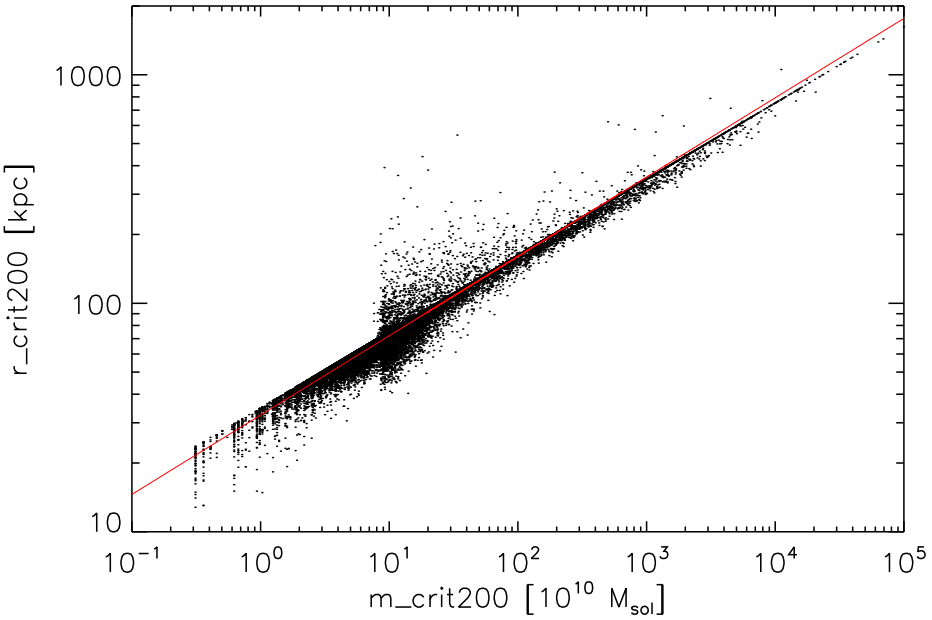

Figure 4.1: R_Crit200 dependence on M_Crit200. The red line represents the best fit: $y = \exp(0.347144 \cdot \ln(x) + 3.47887)$

The energy density of injected magnetic field $\epsilon_{B_{in}}$ is estimated from the galactic magnetic field B_{gal}. When average gas density $\bar{\rho}_{in}$ of the wind material drops below the average density of the ISM $\bar{\rho}_{ISM}$, the frozen-in magnetic field in the plasma dilutes, due to scattering with the denser medium. As the flux through 2 bubbles of different size must be: $\nabla \cdot \vec{B} = 0$, the surface of a bubble scales at $A \propto 1/R^2 \Rightarrow B \propto 1/R^2$, which can be written in terms of the density: $\rho \propto 1/R^3 \Rightarrow B^2 \propto \rho^{\frac{4}{3}}$. The magnetic energy density must therefore dilute as :

$$\epsilon_{B_{in}} = \frac{B_{gal}^2}{8\pi} \left(\frac{\bar{\rho}_{in}}{\bar{\rho}_{ISM}} \right)^{\frac{4}{3}}$$

where the ISM density is just mass over volume: $\bar{\rho}_{ISM} = \frac{3M_{ISM}}{4\pi R_g^3}$

With this we obtain for the injected magnetic energy :

$$\dot{E}_{B_{in}} = \frac{1}{2} B_G R_G^2 v_w \left(\frac{M_w R_G}{3 v_w M_{ISM}} \right)^{\frac{4}{3}} \tag{4.3}$$

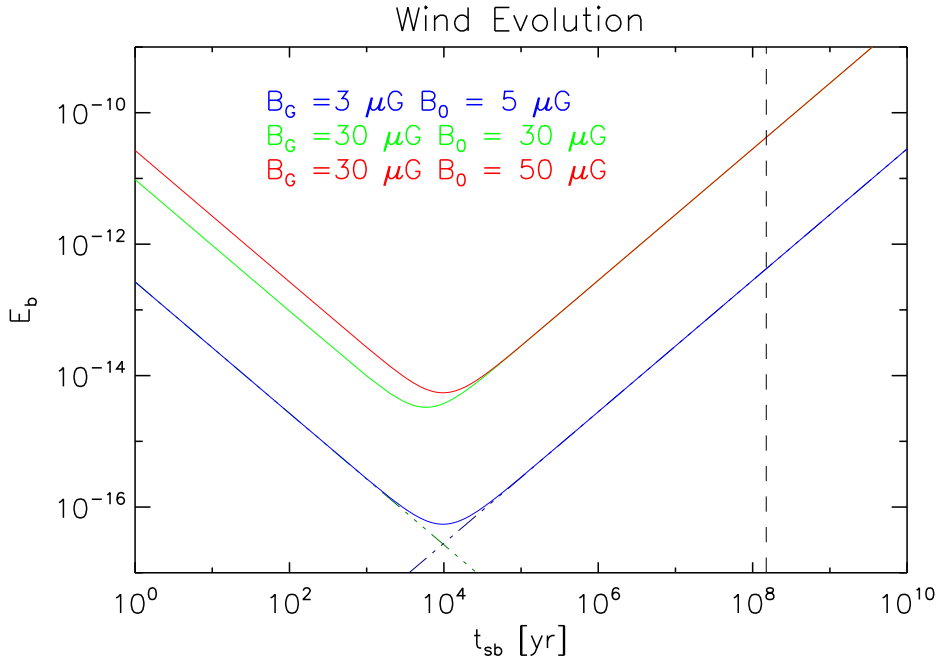

Figure 4.2: Evolution of the magnetic energy of the bubble for different magnetic field in the galactic disc and halo (B_G, B_0). The dashed line of marks the chosen starburst time of 150 Myr, the dot-dashed lines mark the envelopes of the two wind phases

Time evolution The differential equation describing the time evolution (4.1) can be integrated using standard methods:

$$E(t) = E_{B_{in}} \frac{t}{2} + E(0) \cdot \frac{1}{t} \tag{4.4}$$

The time evolution of the magnetic energy in the bubble with different disc field is shown in 4.2. For times $t_{sb} < 10^4$ yr the energy is dominated by the $1/t$ dilution term from adiabatic expansion and the energy descreases from its initial high value. At $t_{sb} = 10^4$ yr the linear term from starburst energy injection takes over and increases the magnetic energy constantly. Note that due to the $1/R^3$ evolution of the volume, the average magnetic field in the bubble is still decreasing.
The matter of seeding frequency, i.e. how often the simulation is stopped, as well as halo selection by mass is discussed in section 5.2.

Parameter	Value	Source
R_0	$(0, 0, 400)^T$ pc	[KWM88]
B_0	$(0, 0, 50)^T$ μG	[KWM88]
B_G	$(0, 0, 12 - 30)^T$ μG	[CB04],[SUB+01]
$\dot{M}_\bigstar$	$10\,\mathrm{M}_\odot/\mathrm{yr}$	[de 01]
t_{sb}	150 Myr	[de 01]

Table 4.1: Summary of initial conditions from M82

4.2 Parameters

As mentioned before, we use results from observations of M82 for our most of the model parameter. The mass of the ISM in the halo is taken from the simulated halo, e.g. L-Subfinds M_Crit200. B_G from observations of several objects is subject to variation in the simulation. The parameter range from the literature is given in table 4.1. B_0 is a somewhat upper limit for the inital field strength in the wind. The value is based on observations done some time ago and may suffer depolarisation effects due to the limited beamsize. We see these values as starting points, and will also run a simulation with lower values for the magnetic fields. B_0 is, compared to what is common for disc galaxies ($5\,\mu$G), quite high. This is expected, from the starburst scenario. We use a starburst time of $t_{sb} = 150\,\mathrm{Myr}$, which corresponds to 3 M81 - M82 like encounters. The magnetic energy depends linearly on time, so that for longer interaction, more magnetic energy is generated. Considering the amount of mergers a clusters sees in cosmological simulations larger values seem reasonable.

4.2.1 M82

The galaxy M82 is an irregular ($I0$) dwarf galaxy at a distance of $3.5 \pm 0.3\,\mathrm{Mpc}$ and an apparent brightness of 9.3 mag [Dat07]. Discovered in 1774 by Bode it's also known as the "Cigar Galaxy", for it's shape on the sky, which implies a near edge on view.

We choose M82 as a reference for wind structure and field strength, as it's not only the archetypal starburst galaxy, but its polidal field structure is well known [RKL+92]. M82 governs a big outflow of plasma with velocities of up to $4000\,\mathrm{km/s}$, on axis away the core [KWM88]. Due to a tidal encounter with M81 in the past, high star formation took place on a timescale of $t_{sb} \approx 50\,\mathrm{Myr}$. The resulting star formation rate is assumed to be in the order of $\dot{M}_\bigstar \approx 10\,\mathrm{M}_\odot/\mathrm{yr}$ [de 01].

Field Topology M82 inherits a poloidal field for distances $z > 0.4\,\mathrm{kpc}$ perpendicular to the disc [RKL+94] in the core, where the magnetic field is carried away by the galactic wind.

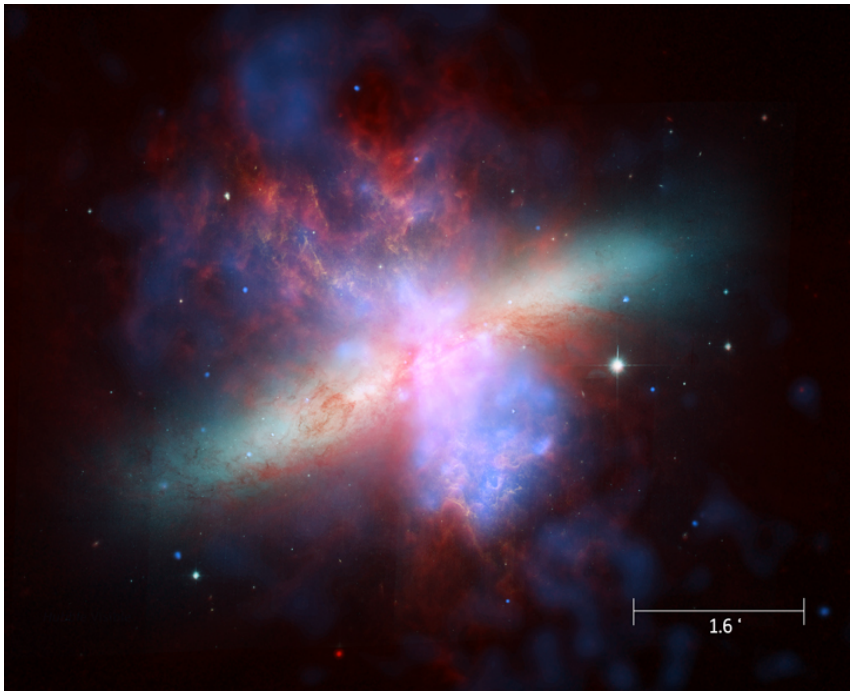

Figure 4.3: Multiwavelength image of M82 (X-ray: NASA/CXC/JHU/D.Strickland; Optical: NASA/ESA/STScI/AURA/The Hubble Heritage Team; IR: NASA/JPL-Caltech/Univ. of AZ/C. Engelbracht)

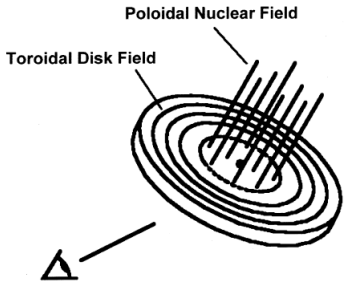

Figure 4.4: Field structure [Jon00]

As our simulations do by far not resolve such small structures as a galactic disc [3] and we are interested on the long range, wind induced effects of the field, perpendicular to the disc, seeding only the poloidal field is reasonable. Still the toroidal field is an important parameter in the model for the wind evolution. An odd configuration of the field in the wind with respect to the poloidal plane is found from M82. This is easy to understand, as the gas is streaming away from the galaxy on both sides, 'dragging' the field lines with it. That implies a quadrupole field geometry to be seeded. Still dipole fields (even symmetry) are found in for example NGC 5775 [TDS+00]. In the simulations we use different configurations, and examine the influence of the seed field topology on the correlation length (see **??**)

[3] The SPH smoothing length is 10 kpc. Seeded haloes contain often less than 10 gas particles

Field Strength in the wind Though M82 is one of the best studied starburst galaxies in the sky, there are no measurements for the magnetic field strength of the wind at large distances. In the core $50\,\mu$G are found within a radius of 0.4 kpc around the center [KWM88]. As this is the region where the wind in M82 originates from, we estimate the value of the magnetic energy in the initial bubble from here. Additional amplification due to shearing processes in the wind are suggested by [BWO99]

4.2.2 Field Strength in the disc

Common field strengths in interacting spiral galaxies are around $12\,\mu$G [Wid02], [SUB+01] in the disc. In the core of starburst galaxies the high star formation rate is induced by fast turbulent motion of the plasma. This results in extraordinarily strong magnetic fields of up to $30\,\mu$G [CB04]. This range of values determines the most important parameter in the wind evolution model. We run our simulations with conservative and more aggressive values, to test our results.

4.3 Dipole Field

To test an even configuration (i.e. A0 dynamo mode) for the large scale structure of the magnetic field, we implemented a dipole:

$$\vec{B} = \frac{\mu_0}{4\pi} \cdot \frac{3\vec{n}\,(\vec{n}\cdot\vec{m}) - \vec{m}}{|\vec{x}|^3 + \epsilon^3} \tag{4.5}$$

with $\vec{n}$ the unit vector in $\vec{x}$ direction, ϵ the softening length and $\vec{m}$ the magnetic moment of the dipole. $\vec{m}$ is obtained by converting the magnetic energy obtained from the wind model to a magnetic dipole moment. Therefore the dipole is parametrised by its strength $\|\vec{m}\|$ and the normed spin vector of the halo $\vec{n}_s = \frac{\vec{s}}{\|\vec{s}\|}$

To avoid the singularity for $\vec{r} \to 0$ we use a softening length of $\epsilon = 10\,$kpc. It resembles the resolution of the simulation, seeding on smaller scales would lack justification. The resulting radial profile, for all angles, is shown in 4.6.

The field energy from the wind model is converted to a dipole moment by :

$$m_z = \sqrt{48\pi^2 E_B \cdot \left(\frac{1}{\epsilon^3} - \frac{1}{R_{max}^3 + \epsilon^3}\right)^{-1}} \tag{4.6}$$

The derivation can be found in the Appendix B.1. For large Rmax this depends on $epsilon^{\frac{3}{2}}$, and diverges for $\epsilon \to 0$ and finite halo sizes. The field strength therefore depends on the resolution of the simulation.

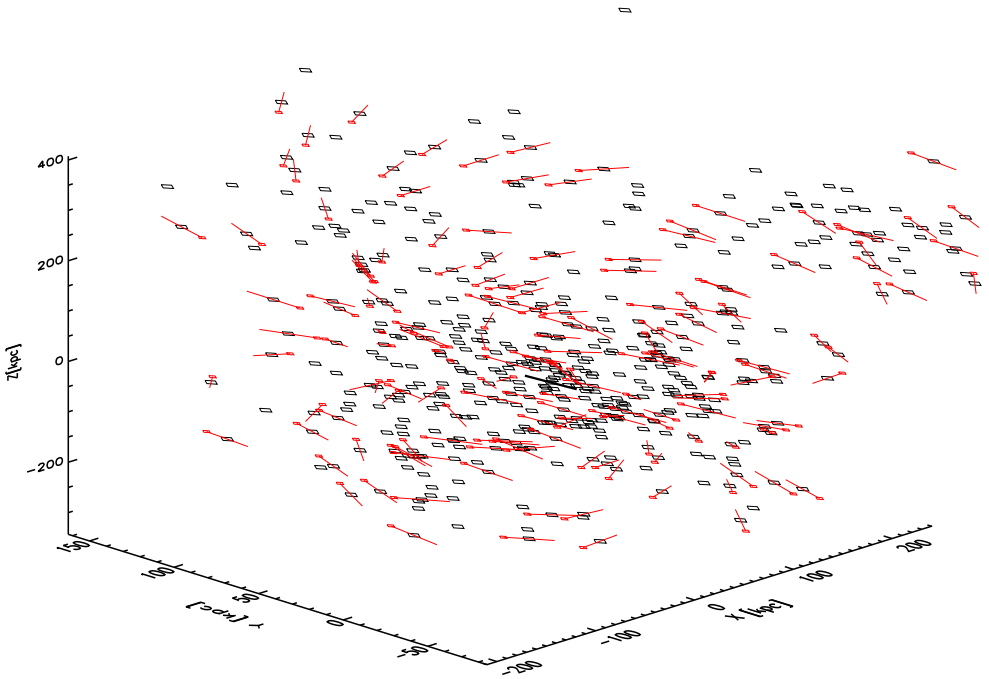

Figure 4.5: Dipole field from the largest seeeded cluster (454 particles) in our first simulation. Only the field topology is shown, Dark matter particles contain no field.

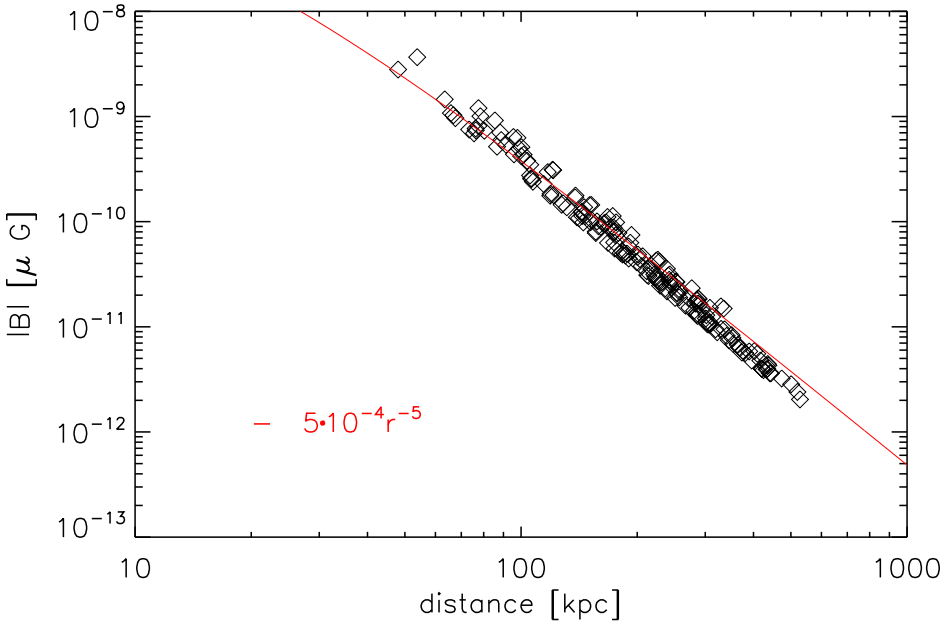

Figure 4.6: Radial profile of the implemented dipole. Deviations from the $5 \cdot 10^{-4} r^{-5}$ function, arise due to the angular dependence on the angle between x-y plane and z axis.

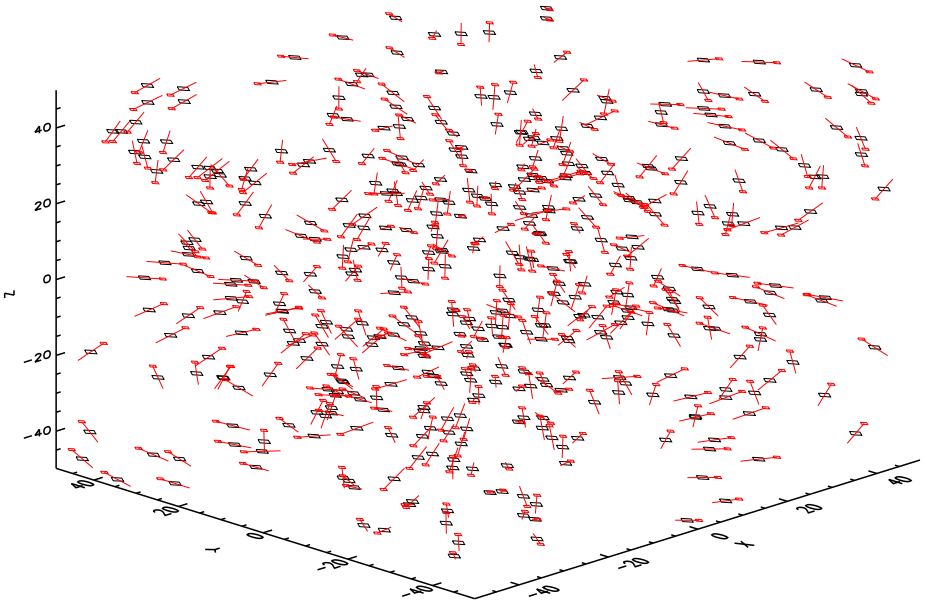

Figure 4.7: Quadrupole Field structure. For better illustration random data, not a simulation is used.

4.4 Quadrupole Field

While more complicated to set up, a quadrupole resembles the symmetric S0 dynamo modes found in most edge on galaxies much better than a dipole. By examining the differences in correlation length, it is used to find out about the influence of seed field topology on the cluster field structure. We modelled the quadrupole field with two magnetic dipoles at a distance d on the rotational axis of the galaxy. The dipole moments carry opposite sign and are smoothed by the parameter ϵ, usually 10 kpc.

$$\vec{B} = \vec{B}_+^{DIP} + \vec{B}_-^{DIP} \tag{4.7}$$

$$= \frac{\mu_0}{4\pi} \cdot \left(\frac{3\vec{n}_+ \left(\vec{n}_+ \cdot \vec{m}_+\right) - \vec{m}_+}{r_+^3 + \epsilon^3} + \frac{3\vec{n}_- \left(\vec{n}_- \cdot \vec{m}_-\right) - \vec{m}_-}{r_-^3 + \epsilon^3} \right) \tag{4.8}$$

with

$$\vec{r}_\pm = \vec{r} \mp \frac{d}{2}\,\vec{s} \qquad r_\pm = |\vec{r}_\pm| \qquad \vec{n}_\pm = \frac{\vec{r}_\pm}{r_\pm} \qquad \vec{m}_\pm = \pm m_z \vec{s}$$

where we defined the distance and normal vectors for the dipoles and $\vec{s}$ the spin vector of the galaxy.

The seeded field shows the expected radial dependence of field strength : $|\vec{B}| \propto \frac{1}{r^5}$. Small deviations occur due to the z dependence of the field strength. This can be seen in 4.8, where the outer particles are located further away from the x-y-plane.

The quadrupole field is zero at the origin. In small haloes with only one bound gas particle, it is often found in the center, leaving its magnetic field zero. As the resolution of the simulation is limited and we don't want to loose many particles from this fact, those zero particles are seeded with a random seed, inside of a tenth the softening radius: $\epsilon = 1\,\mathrm{kpc}$. Observations show large fields in the center of starburst galaxies. Here our model does not fit the observations anyway, as on small scale magnetic fields are generated by dynamo effects in stars, dislocated by winds and entangled by turbulent motion. Therefore it is justified to assume a rather large magnetic field with random direction. The (pseudo-)random seed is generated from the systime in the code

Again the magnetic energy obtained from the wind model needs to be converted back to dipole moments, parametrising the quadrupole. This is done by :

$$m_z = \sqrt{E_B \left[\frac{1}{24\pi^2} \left(\frac{1}{\epsilon^3} - \frac{1}{R_{max}^3 + \epsilon^3} \right) - \frac{1}{16\pi^2}\gamma \right]^{-1}} \tag{4.9}$$

$$\gamma = \frac{1}{4\pi} \cdot \int dV \frac{3\vec{n}_+ \left(\vec{n}_+ \vec{e}_z\right) - \vec{e}_z}{r_+^3 + \epsilon^3} \cdot \frac{3\vec{n}_- \left(\vec{n}_- \vec{e}_z\right) - \vec{e}_z}{r_-^3 + \epsilon^3} \tag{4.10}$$

where γ is the correction integral to the dipole conversion. This determines the influence of the distance parameter d on the moment. Unfortunately γ can only be solved numerically. This is done for several halo sizes (e.g. different bubble radii), and then interpolated by a cubic spline.

Analytically the factor in square brackets in 4.9 tends to infinity for $d \to 0$ and $\epsilon = 0$. for finite values of ϵ it does not. Still for large distances d, the factor becomes equal the dipole value. From this we set $d = 10\,\mathrm{kpc}$. This corresponds to the numerical resolution. A larger d is not observed, smaller values would be arbitrary or maximize the magnetic moment (for $d = 0$) to a value determined by the softening length and therefore the numeric resolution. In reality the field structure on pc scale is not necessarily connected to the one on kpc scale. In the cores of starburst galaxies, the observed coherence lengths are small. The detailed derivation can be found in B.2.

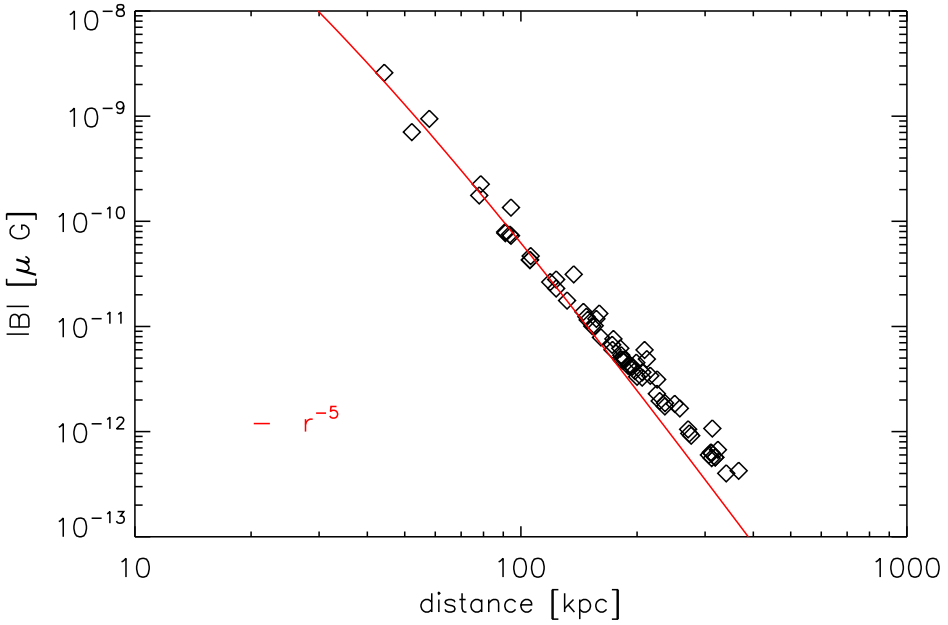

Figure 4.8: Radial profile of the largest cluster in simulation mhd_z

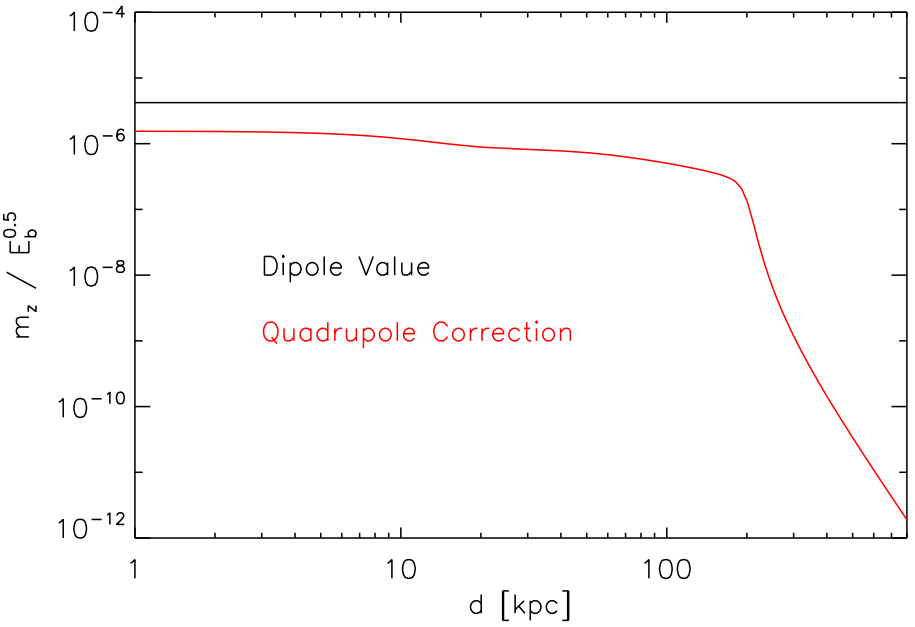

Figure 4.9: γ ,i.e. quadrupole correction over distance of the dipole moments

5 Simulations

To investigate the possible origin of cluster magnetic fields from galactic winds, there were a total of 5 simulations done. We tested 3 configurations using a dipole structure, reducing the strength by a factor of 10 (100) compared to the physical model, obtained from observations. To test the influence of the field symmetry relative to the galactic disc, another simulation was done using a quadrupole structure with the physically motivated field strength parameters. In the fifth run we seeded 5 times[1] at different redshifts with a 10th of the physical field. This was done to investigate the influence of the discrete seeding procedure on the simulations.

To find our seeding strategy, we examine a control run, done before by [DGST05] with a constant cosmological seed field of $|B| \approx 10^{-11}\,\mathrm{G}$. The cosmological evolution before seeding was done using their constant magnetic field to keep the simulations as comparable as possible. In practice that means, that we started with an snapshot from this simulation as initial condition.

5.1 Parameters

From now on we will refer to the simulations in this table as follows: The run with a constant seed field, done by [DGST05] is called "the control run" or run with "constant seed field". The simulations 1, 2 and 3 will be called the "dipole runs", simulation 4 the "quadrupole run" and number 5 the "multiple seed run".

Every run is characterised by two magnetic fields (for disc and halo), a length (distance of the halo field), a starburst time and the field geometry. There is a huge number of specifications aside from that, which either define the GADGET-2 run or go into the wind model. Table 5.1 shows the characteristic parameter. Furthermore we used a starburst time of $t_{sb} = 150\,\mathrm{Myr}$ and a star formation rate of $\dot{M}_\star = 10\,\mathrm{M}_\odot/\mathrm{yr}$. Note that the complete GADGET-2 parameter and Makefiles can be found in the Appendix A.2.2 and .

All Simulations were done for a standard λCDM cosmology, with $\Omega_0 = 0.3$,$\Omega_\Lambda = 0.7$ and $\Omega_{Baryon} = 0.04$ in a cubic box with an edge length of $240\,\mathrm{Mpc}$ using periodic boundary conditions. There was a total of 108201923 particles in the box: 50730389 dark matter, 50730389 gas and 6741145 disc particles. The magnetic field was smoothed

[1] For this in the smoothing counter the MainTimestepCount has to be set manually

Parameter	Sim 1	Sim 2	Sim 3	Sim 4	Sim 5	Comment
Structure	Dipole	Dipole	Dipole	Quadrupole	Dipole	
B_{disc}	$30\,\mu$G	$3\,\mu$G	$0.3\,\mu$G	$30\,\mu$G	$3\,\mu$G	Disc Field
B_0	$50\,\mu$G	$5\,\mu$G	$0.5\,\mu$G	$50\,\mu$G	$5\,\mu$G	Halo Field
r_z	0.4 kpc	0.4 kpc	0.4 kpc	0.4 kpc	0.4 kpc	Halo Size
Seeding time [z]	4.1	4.1	4.1	4.1	4.1 - 2.8	
# of Main Timesteps	-	-	-	-	4,8,13,21	Snapshots: 8, 10, 12, 14, 16

Table 5.1: Simulation Parameters, Simulation 5 is seeded 5 times at redshifts: $z \in \{4.6, 4.1, 3.6, 3.2, 2.8\}$

every 15 main timesteps with a fraction of 1, corresponding to $q = 1$ in 3.14. The output was done using a list of redshifts, which can be found in the Appendix A.2.3

5.2 Seeding Frequency And Mass Range

The implementation of the magnetic field in the haloes is not done on the fly, but by modifying an output file at a given redshift. Therefore the magnetic field generation is discrete in time. To achieve a high efficiency the time of seeding is important. Is has to balance the number of new haloes existing to seed homogeneous enough and the number of new haloes still to come, to allow for enough merger events. Figure 5.1 shows the number of new halos in the control run over redshift. From this we find a redshift of 4.1 $\Leftrightarrow$ Snapshot8 optimal. [KLH99] suggest $z = 10$ as the beginning of a continuous seeding process. We can not simulate exactly this behaviour, with the corresponding backreactions.

In the first 4 simulations, where seeding is applied only once, every halo below $M_{Halo} = 30010^{13}\,\mathrm{M}_{\odot}$ is seeded. Larger haloes are not considered, because their potential well is assumed large enough to prevent larger galactic outflows.

5.3 On Errors

Cosmological simulations, like the ones, that form the basis of this work, are very complex. They are highly optimised for efficiency, to solve the underlying theory, in this case magnetohydrodynamics and gravity in an expanding universe. These theories describe only limited parts of the complex cosmological effects.

If one asks for errors in this context, answers cannot easily be given by an error calculation. One has to considers two main points:

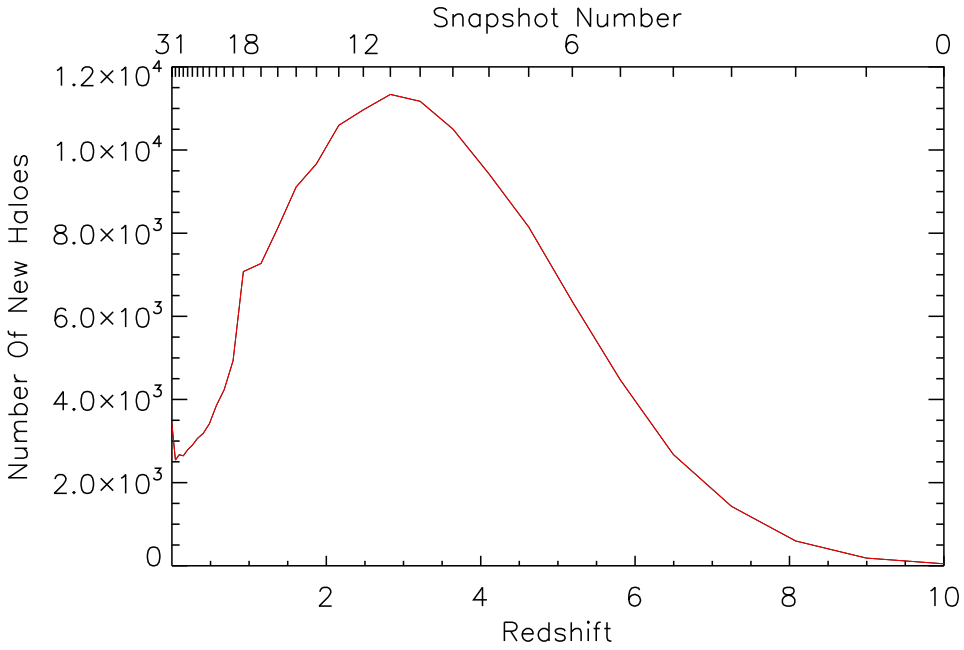

Figure 5.1: New haloes over redshift in the control simulation from [DGST05]

1. How well is nature represented by the theories used ?

2. Are those theories reproduced accurately during computation ?

As already indicated above, there is much more physics in cosmology than ideal MHD and gravity. Radiative cooling, stars, supernova feedback are only some effects missing in our theoretical description. Therefore, when simulating cosmic evolution, we must not forget that we might miss some important points. This work is an investigation of one of those missing components: the influence of supernova feedback on magnetic fields in galaxy clusters. While focussing on this point, others are neglected. Here lies the primary source of errors we make. This can neither be resolved with an error calculation nor even fully understood, without a simulation that covers all relevant effects at once and on the fly.

To clarify the latter point, testproblems like 3.1.3 are set up. Knowing the analytical solution, the comparison between model and numerical simulation can be tested. While a successfull shocktube or adiabatically collapsing sphere test shows code behaviour for simple setups, this not necessarily true anymore for cosmological setups. Several parameters have to be fine tuned and experience such kinds of simulations is needed. Still many successfull runs confirm the valid implementation of MHD and gravity in

GADGET-2.

6 Analysis And Results

We begin this chapter with a simple visualisation of the cosmological box. This rather crude inspection already shows, that with the physical model described in 4, reasonable fields in clusters are achieved at $z = 0$. If follows a "time resolved" analysis of our runs using histograms, where we analyse the evolution of the fields. The spatial distribution in the box is examined using the cumulative filling factor.
Magnetic fields on large scales are nearly always observed in clusters. Therefore we concentrate on a cluster based analysis, where we focus on the heaviest clusters of the simulations. We show the average field in the clusters over temperature and build synthetic RM and radio power maps, to investigate observable differences in the field structure.

6.1 Box Based Analysis

While an investigation of properties of a whole simulated box make the comparison between different runs easy, these properties not comparable to observations.

6.1.1 Visual Inspection

To get a feeling for the seeding process, we built images of the smoothed projections of magnetic field strength. For every pixel the integrated line of sight field strength was calculated from all contributing SPH particles. Figure 6.1.1 shows images centered on the simulation box. All show a 40 Mpc box at redshift $z = 4.1$. At $z = 0$ this includes the simulation. While the first image is taken from a simulation with constant field[1] at redshift $z = 4.1$, the second one is done after seeding every halo below $300 \times 10^{13}\,\mathrm{M}_\odot$ with a dipole structure for the first time. In the third image we show the magnetic field at redshift $z = 0$ for the constant seed field. The last image displays the final state of the simulation for a seed using the wind model.The high fields in the superclusters are clearly visible. It shows less filamentary structures than before as well.

[1] seeded at $z = 10$

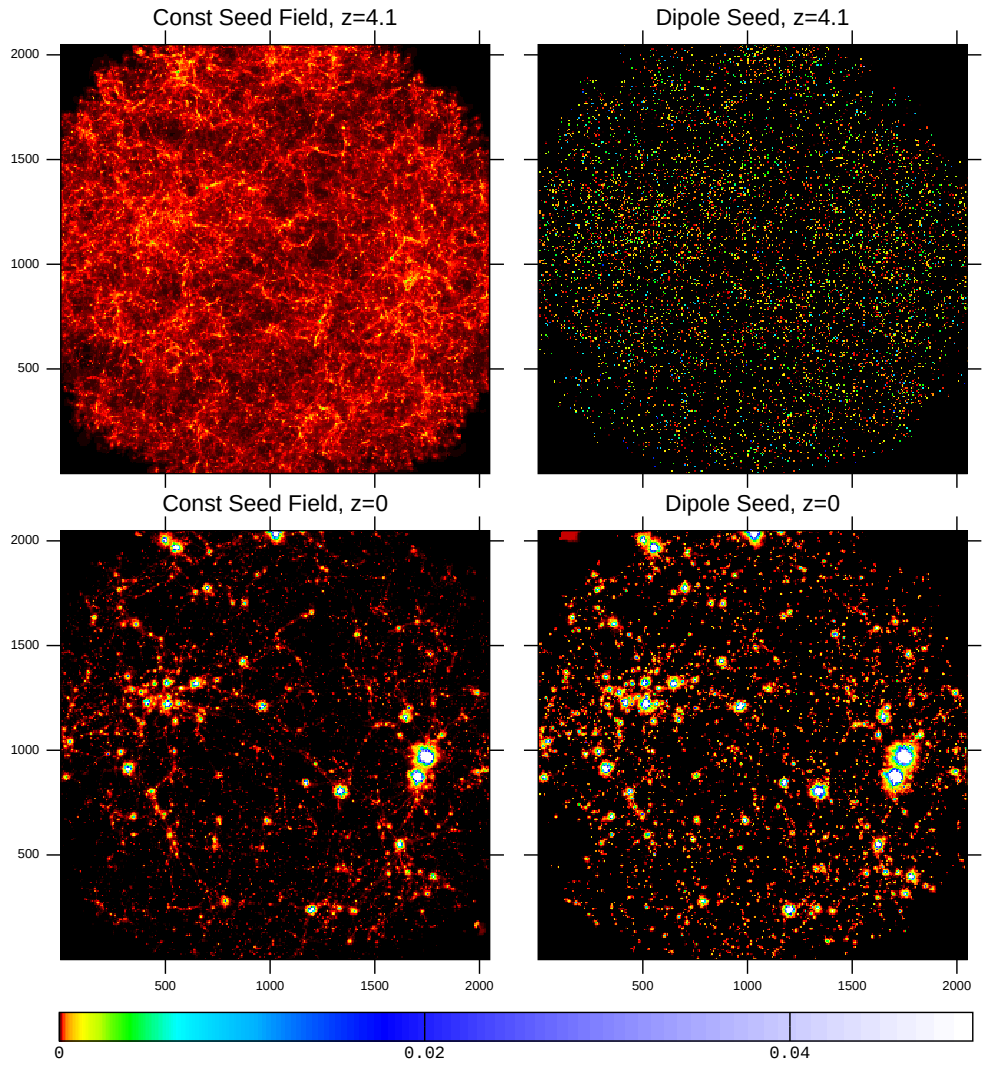

Figure 6.1: Visualisation of the magnetic field strength inside the simulated box. For a constant cosmological seed field, the structure is dominated by the dynamics induced by collapse (upper left panel). Seeding implements isolated fields in every halo (upper right panel). For todays redshift after structure formation, the seed fields are amplified in clusters (lower panels), but weak in voids. The left panel shows the evolved constant field, in the lower right the result from halo seeding can be seen. Because of the constrained initial conditions, the big clusters can be identified, Perseus (middle left), Virgo (top) and Centaurus (middle right).

6.1.2 Time Evolution of the Field

The time evolution of the field in the SPH particles shows the amplification of the collapsing structure. To shed light on the differences betweet runs, exspecially compared to the control run, we plot histograms, of the energy density of every SPH particle in our simulations. In all graphs, the control run is collored in black, the single dipole runs in red,green and magenta, the multiple seed dipole run in light blue and the quadrupole run in dark blue. Please note that this is a log-log plot using logarithmic binning for the histogram.

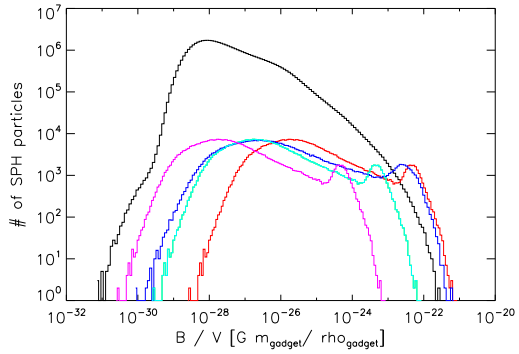

Figure 6.2: $z = 4.1$, Snapshot 8

The first histogram 6.2 shows all 6 simulations at redshift 4.1. As the control run seeds all particles in contrast to the seed runs, the integral of the histogram is much larger. The three dipole runs (red, green and magenta) have the same shape, but differ by a factor of 10 in energy, as expected. The quadrupole run shows a different shape and spans over a larger energy interval. Both runs seed the same particles and contain the same energy. As the strongest field occur in the middle of haloes, the difference between both runs is small here. But a particle far out contains much less field as the radial dependency of a quadrupole field is $\propto r^{-5}$ and falls of steeper than the dipole field $\propto r^{-3}$. The multiple seed run is indentical with the second dipole run here.

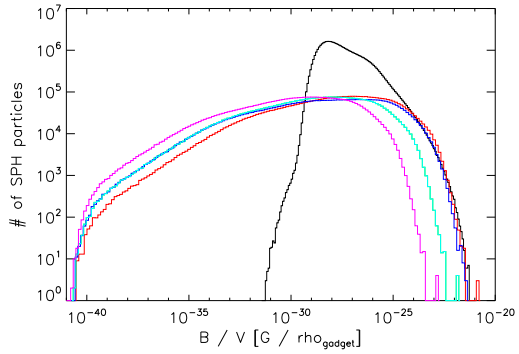

Figure 6.3: $z = 3.6$, Snapshot 9

Note that we changed the scale on the abscissa of the plot. This is necessary, because all seed runs contain now particles with very low magnetic field energies. A sneak peak into the log files reveals, that between snapshot 8 and 9 a smoothing[2] of the field was triggered. As the control run is already evolved, the smoothing does not change its shape in the histogram very much. But it smooths the field at the halo edges into the sourrounding particles. Still the number of magnetised particles is much lower than in the control run. At the high end of the field, the changes are minimal, because only little time elapsed. Again there is no difference in

[2]Please refer to 3.1.3 for a description of the process

multiple seed run and second dipole run.

In the 10th snapshot, the effect of the second seeding in the multiple seed run can be seen. At $B/V \approx 10^{-24}$ both runs differ significantly. The multiple seed run implants fields like this at 3 more snapshots to investigate the effect on the field evolution. The over all trend is not very exciting, with a slight amplification of all fields. At this time all particles contain a non-zero magnetic field in the control run, while in the seed runs approximately 30% are magnetised.

Again, we extended the x-axis range. At this point in the run, the last seed was done in the multiple seed run. Refering to image 5.1 the "hot phase of halo production" has ended so a further seeding wouldn't make sense. The differences in the green and light blue curve, corresponding to seeding once and 6 times are obvious. XXXX MORE HEREXXX

As the simulation runs the infall and aggregation of haloes amplifies the magnetic field, which can be seen here for all runs. Depending on the strength of the seed field, the maximum field is approximately several μG . XXX MORE HERE XXXX

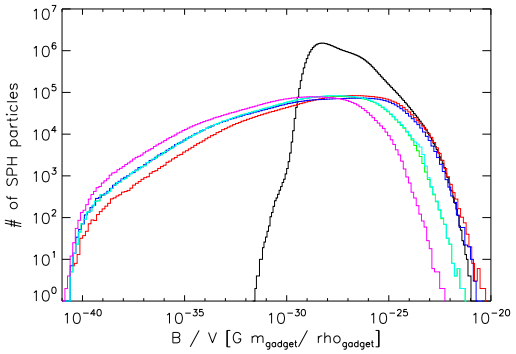

Figure 6.4: $z = 3.2$, Snapshot 10

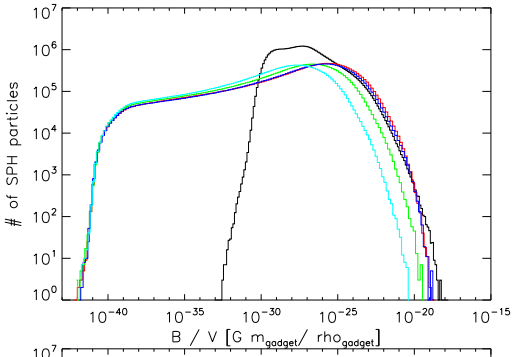

Figure 6.5: $z = 1.3$, Snapshot 16

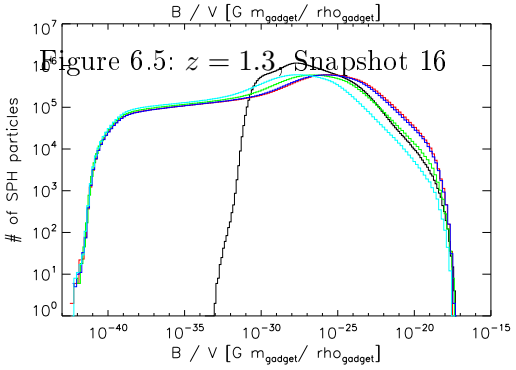

Figure 6.6: $z = 0.48$, Snapshot 22

Figure 6.7 shows the final histograms, found in our local universe box today. All seed runs show a quite similar distribution of the magnetic field. While the lower end is dominated by smoothing (in voids as we will later see) and the seed field respectively, the high fields saturate for all runs, except the smallest dipole. At this point, about 90% of all particles are magnetised. The similarity of the curves indicates that the distribution of the magnetic field strength XXX MORE HERE XXX

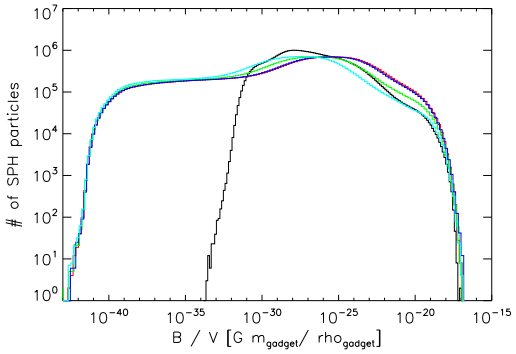

Figure 6.7: $z \approx 0$, Snapshot 30

6.1.3 Cumulative Filling Factor

So far, we looked at the field strength in the whole box. To shed light on the question, how the field is distributed spatially, it is helpful to plot the volume weighted cumulative filling factor of the magnetic field. This is done by imposing a threshold on the magnetic field and estimating the volume above and below it. That means, for a given value of B we plot the fraction of the box volume filled with field above and below it. Theefore the rising curve in image 6.1.3 corresponds to the volume fraction above the field value, the falling curve to the volume above it.

Because of the cosmological seeding, the control run (black curve) shows a minimum field of $\approx 10^{-11}$ G everywhere. The dipole and quadrupole runs (red and dark blue curve) give not only smaller fields, but end up at the same maximum field strengths. The differences between both runs are minimal for both pairs of curves. This implies, that the field geometry in the wind does not influence the field strength in observed clusters. Field structures entering the ICM at the seeding redshift of $z = 4.1$ do not change the strength of amplification, as expected.
The smaller dipole run (green curve) gives reasonably higher filling factors for medium thresholds, which implies smaller fields in voids. Since the magnetic field in voids is not observed, a possible cosmological field might be important and the role of AGN outflows is not considered in our simulations, it is not possible to constrain the wind model this way. XXX MORE HERE XXX

6.2 Cluster Based Analysis

For the section, we select the 16 largest clusters of the simulation and build artificial observables using widely accepted models (e.g. secondary models for CR energy density).

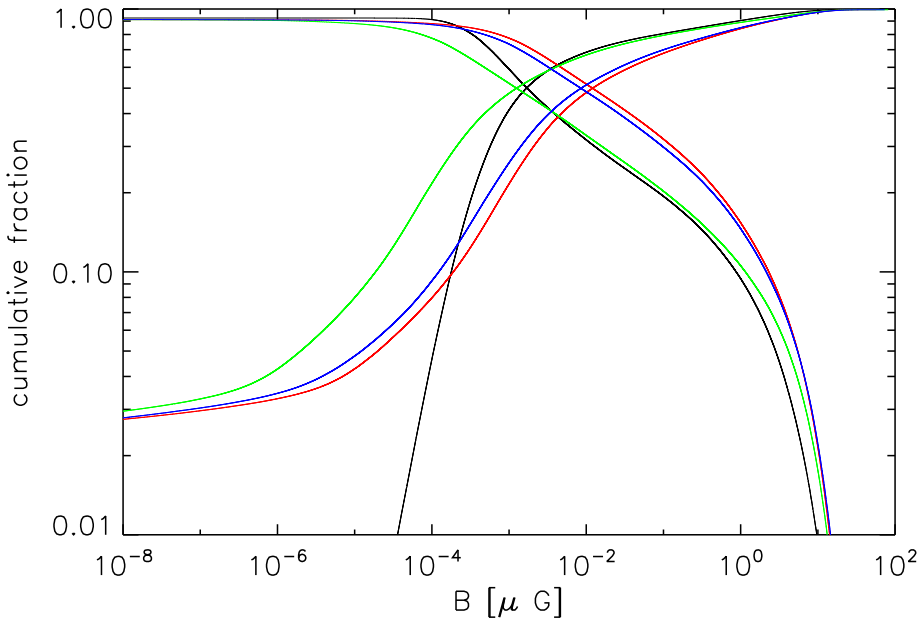

Figure 6.8: Volume weighted cumulative filling factor of the magnetic field in the whole cosmological box. Black - control run, red - dipole, green - $0.1 \cdot$ dipole, magenta - $0.01 \cdot$ dipole, lightblue - multiple seed dipole ,blue - quadrupole,

6.2.1 Cluster Profiles In ρ, T and $|B|$

Before we start with a detailed comparision of our runs in terms of synthetic observations, we want to show, that the selected clusters actually show reasonable shapes[3] in terms of density, temperature and magnetic field strength over radius. This is important, because when one constraines magnetic fields from the observation of synchrotron haloes and rotation measurements, the typical length scale for field reversals is a free parameter. The density profiles shown in figure 6.2.1 are all compatible with a the canonical β model[4] and similar not only to each other, but to the control run. Our model neither constrains the length scale nor motivates any change in it. The clusters do not show any significant difference in temperature, density and field strength from the ones before.

[3] spherically averaged

[4] $n_{gas}(r) = n(r_c)\left(1 - \frac{r^2}{r_c^2}\right)^{-3\beta/2}$

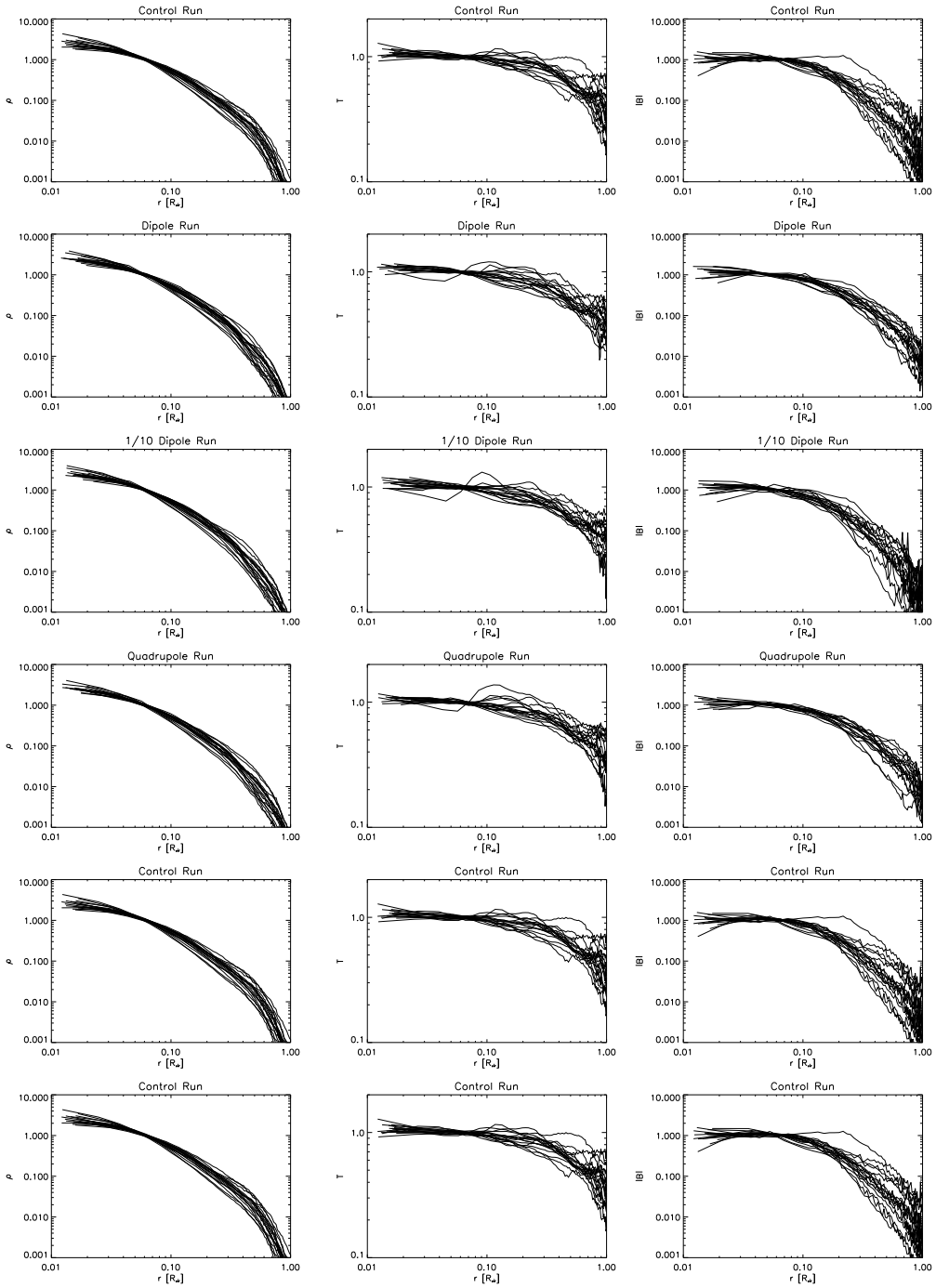

Figure 6.9: Density, Temperature and magnetic field strength radial profiles for the largest 16 clusters. The profiles are scaled to R_{vir} and normalised to the same mean value in $0.1 \times R_{vir}$

6.2.2 Average Field Strength in Clusters

The amplification of magnetic fields in clusters is not only from adiabatic compression of the collapsing structures, but also from induction during mergers. Plotting the average magnetic field in $0.1 \times R_{vir}$ of the clusters over its temperature shows the domination of the latter effect. There is a clear correlation between Temperature (corresponding to size and number of merger event) and field strength. This was shown by [DGST05].

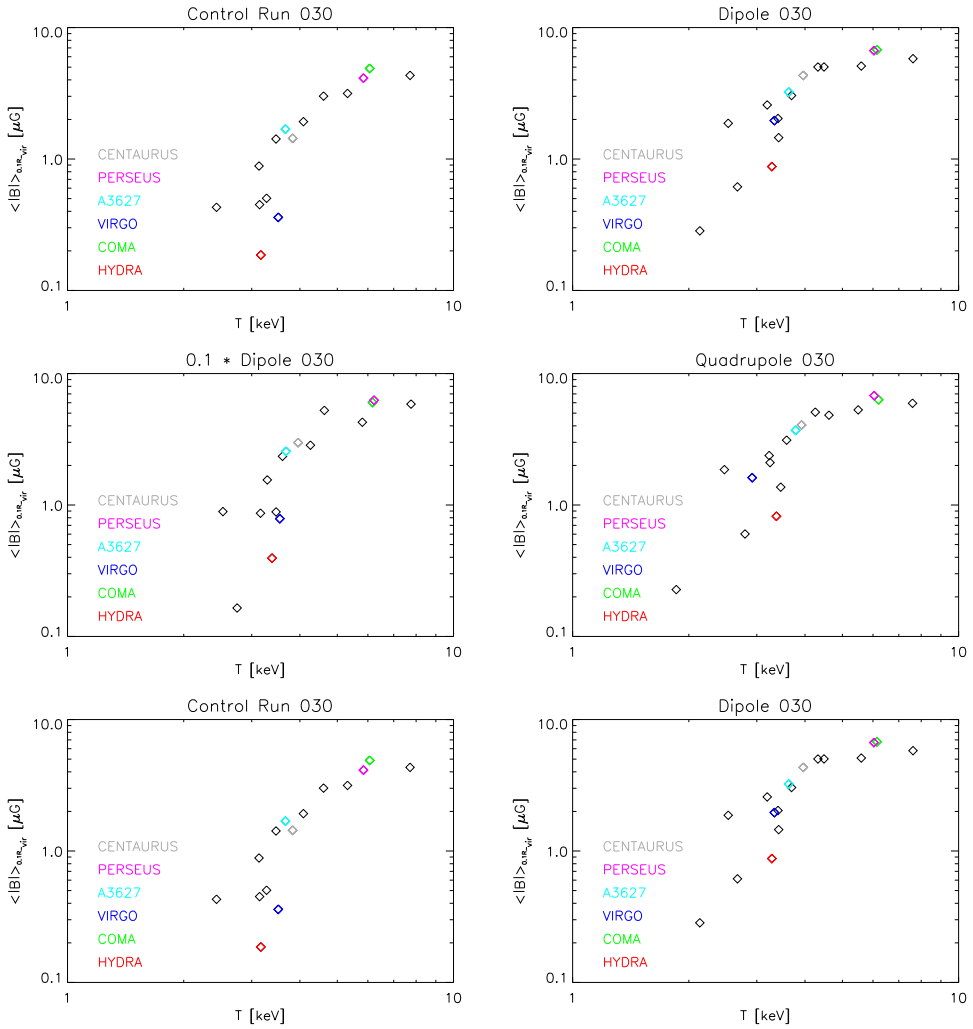

Figure 6.10: Averaged magnetic field strength inside 1/10 of the virial radius for the largest clusters in all our simulations.

As cluster magnetic fields are observable, we can make predictions for them. In figure

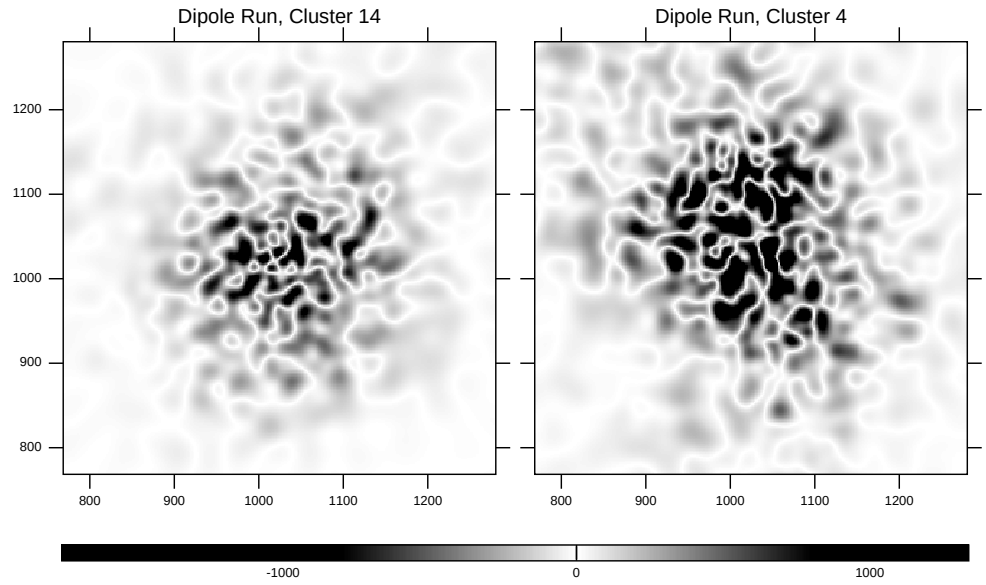

Figure 6.11: Synthetic Faraday rotation maps from dipole run at $z = 0$ for the two largest clusters.

6.2.2 we plot $< B >_{0.1R_{vir}}$ over T for the largest clusters. Due to the constrained initial conditions, it is possible to identify several clusters with their real counterparts.
All runs show the expected domination of induction in the generation of the field. In addition, a comparsion between the two dipole, the quadrupole and the multiple seed run yields that the largest clusters saturate in average magnetic field strength. The average field strength in the large clusters like Perseus (purple) and Coma (green) is comparable, although the initial energy in for the seed was reduced by a factor of ten or the symmetry of the seeded structure was changed respectively. The contribution from galactic winds to the generation of magnetic fields in galaxy clusters is relatively unsensitive to the field strength in the seeding galaxies and winds and to the symmetry properties of the field.

Note that the normalisation of the average magnetic field strength might be sensitive to the resolution of the simulation. If the powerspectrum of the field had a lot of power on scales, below the numerical resolution, it it is not resolved in the simulation and the corresponding SPH particles contained only an averaged value.

6.2.3 Synthetic Faraday Rotation

To get our hands on the structure of the magnetic field in the clusters, we build artificial Faraday rotation maps. Figure 6.2.3 gives an impression on, how these maps can be

visualised. Rotation maps are particulary interesting in terms of the field structure, i.e. the observed number or length scale of field reversals. We build radial profiles from the maps and calculated the structure function.

Radial RM-Profiles

To inspect how the found differences in field strength between run effect synthetic observations, we plot radial profiles of the cluster rotation measurements. We bin the maps radially and plot the median of all pixels from all clusters in a bin. Overploted are observations of rotation measurements from point like sources in Abell Clusters ([CKB01] and [KKT91]). Because the selection function of these clusters is ill defined, we also show the plots for clusters with mass above $3 \cdot 10^{14}\,\mathrm{M}_\odot$ and above $5 \cdot 10^{14}\,\mathrm{M}_\odot$. As the Abell observations are quite old, is is reasonable to believe, that the data is based on a rather heavy selection.

A comparison of the three selections in 6.2.3 shows that our model give comparable RM in the large clusters, but predicts larger rotation measurements in the center of smaller clusters. The mass scaling of the average RM profiles in the center of clusters changes. XXX MORE HERE XXX

Projected Structure Functions

A statistical way to analyse and quantify the field structures in clusters is, to build the 2D structure function of a RM map of the cluster.

$$S(dx, dy) = \langle |RM(x, y) - RM(x + dx, y + dy)| \rangle$$

This was done for, e.g. A 119 by [MGF+04]. We plot the structure function of our biggest 3 clusters 0, 4 and 13. The curves are clearly limited by the resolution of 10 kpc when compared to figure 6.2.3, where the solid line marks the observed structure function in A119. The structure does not change much throughout the runs. Cluster 0 has less power on small scales using a cosmological seed field, when the cluster is similar using any of the halo seed models.

As the RM measure does not change with model, especially, when comparing dipole and quadrupole seeded structure functions, this parameter does not influence the synthetic observations. If follows, that the structure of magnetic fields in galaxy clusters today is not correlated with the field structure of eventual seeding outflows at $z \approx 4$.

6.2.4 Radio Halo Power

xxxxx

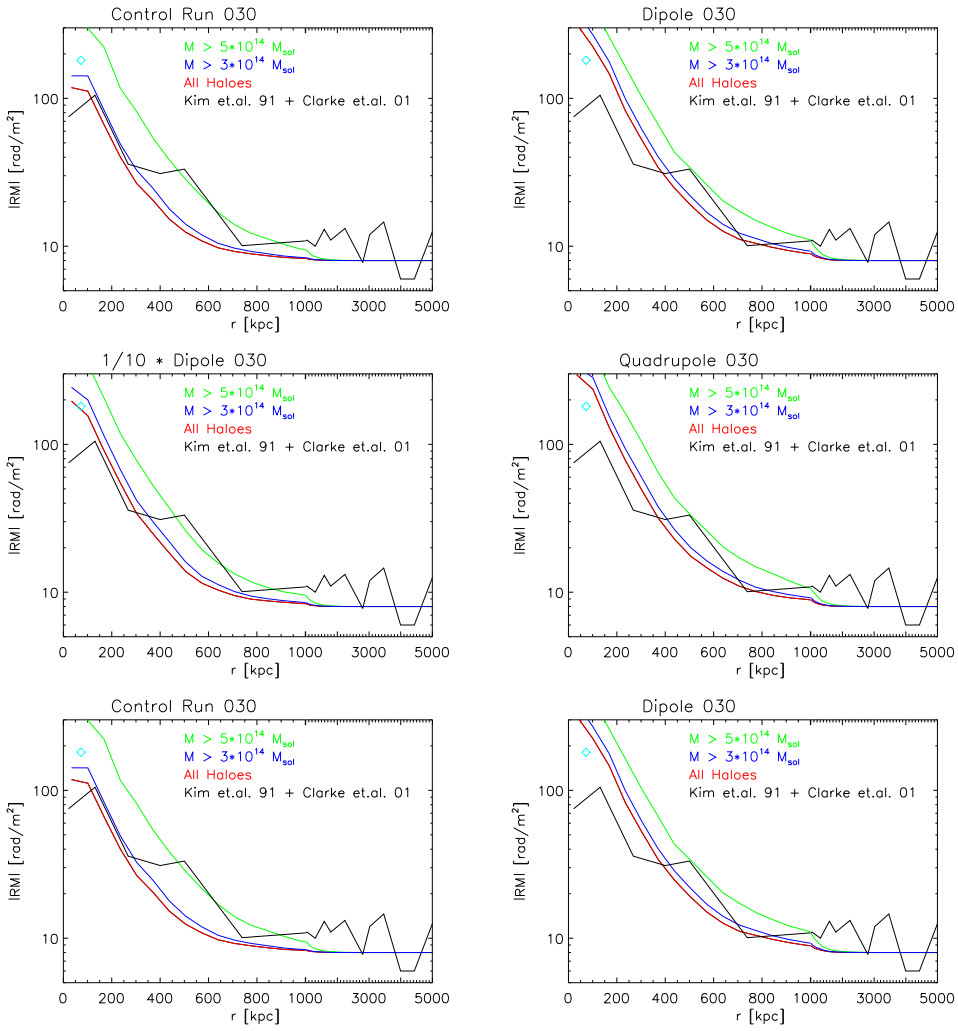

Figure 6.12: Radial profiles averaged over all clusters in comparison to observations for all runs. Observations are plotted black, a selection of all clusters red, and two heavier selections in green and purple.

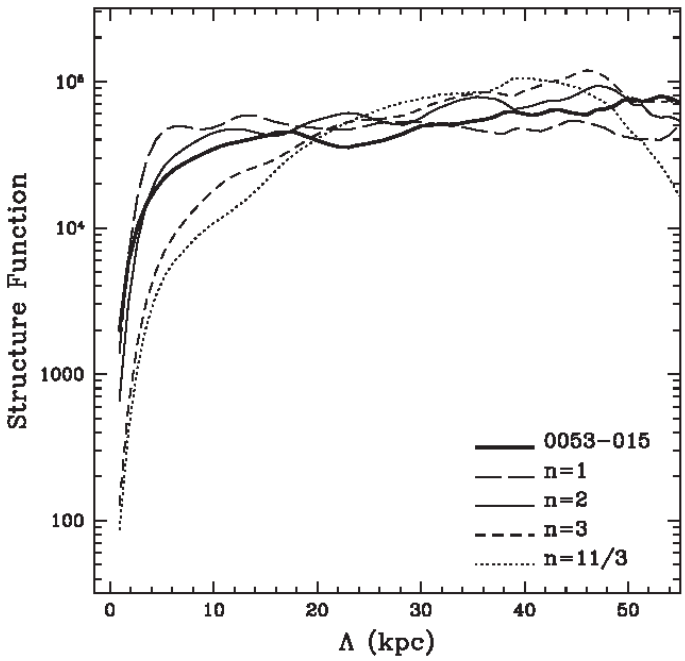

Figure 6.13: Observed (solid line, A119) and simulated structure function from [MGF+04].

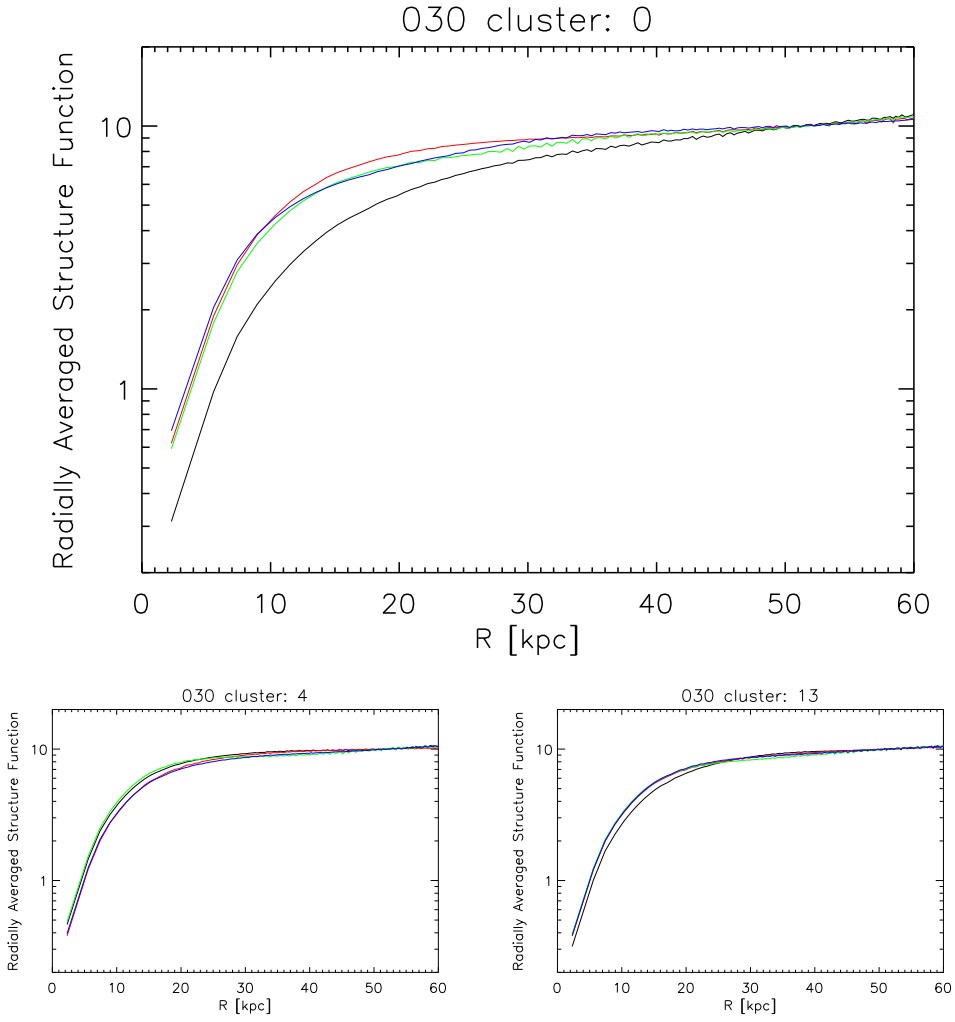

Figure 6.14: Structure function of 3 big clusters for all simulations. Control Run in black, dipole in red, blue and purple, quadrupole in dark blue and multi seed run in light blue. The function is normed to be 10@ 50 kpc

7 Summary

7.1 Prospects

A Code Documentation

A.1 Seed.pro

The procedure of seeding magnetic fields to a GADGET2 snapshot is done by an IDL program and several subroutines. Figure A.1 at the end of the chapter shows an overview of the program.

It accepts as input parameters: the snapshot number `snapnum` to be read from, the disc `BD` and halo magnetic field `B0` for the wind model in Gauss, and the wind size `rz` in kpc. `kill` removes existing field from the snapshot, before writing. If `vmax` is set, not new haloes, but every haloes with vmax below this value is seeded. `Type` set to either D or Q sets the field structure and `qdist` the distance parameter for the quadrupole.
The program then reads all needed information from the snapshot, the subfind data and the merger tree into an array of structures, where every structure corresponds one halo. The field is then found after solving the wind model for every specific halo, and converting its energy to a magnetic moment. In the case of the quadrupole, a particle at $\vec{x} = \vec{0}$ would get a zero field. To avoid that behaviour (its unphysical) the particle is displaced by a random value smaller than the softening ϵ. If the Q is chosen,i.e. the wind structure is a quadrupole, the correction gamma is calculated in `BUILD_CORR_TABLE()` and saved for later used. It calculates the integral for several outer radii and interpolates with an cubic spline.
The output is then written to `start_\$snapnum`.

A.1.1 Quadrupole Implementation

While the implentation of the windmodel and the dipole is straight forward, it is helpfull to describe the way the quadrupole is implemented.
The magnetic quadrupole moment is calculated from 4.9.

```
function mm_quad, E_B, eps, radius, d,debug=debug
   return, sqrt(E_B)*(1./(24.*!pi^2.)*(1./eps^(3.)-1./    $
             (eps^3.+radius^3.))-1./(!pi^(2.)*16.) *  $
             quad_corr(epsilon=eps, rmax=radius, qdist=d) )^(-0.5)
end
```

The corresponding correction $\gamma(\epsilon, qdist)$ is calculated once for a pair of $\epsilon, qdist$ and then saved for faster used. The integral is interpolated by a cubic spline up to a maximum

halo size of 1000.

```
pro Build_Corr_Table, epsilon,  qdist, Nstep, debug

    table =  make_array(50, /double)
    FOR maxR=0,49 DO BEGIN
        step = maxR / Nstep

        tmp  = Make_array(Nstep,/double)
        zarr = Make_array(Nstep,/double)
        rarr = Lindgen(Nstep)*step
        FOR i=0L,Nstep-1 DO BEGIN
            zstep = SQRT(maxR^2. - (i*step)^2.) / Nstep
             zarr[*] = indgen(Nstep)*zstep
            tmp2  = quad_gamma(rarr[i],zarr,qdist=qdist,epsilon=epsilon)
            tmp[i]    = zstep * (TOTAL(tmp2) - (tmp2[0]+tmp2[nstep-1])/2. )
        END
        table[maxR] = (TOTAL(tmp) - (tmp[0]+tmp[nstep-1])/2.)*step
    END
    print, '... First 50 done ...'
    Nstep = Nstep*2.
    FOR maxR=50,1000,50 DO BEGIN
        step = maxR / Nstep

        tmp  = Make_array(Nstep,/double)
        zarr = Make_array(Nstep,/double)
        rarr = Lindgen(Nstep)*step

        FOR i=0L,Nstep-1 DO BEGIN
            zstep = SQRT(maxR^2. - (i*step)^2.) / Nstep
               zarr[*]  = indgen(Nstep)*zstep
            tmp2  = quad_gamma(rarr[i],zarr,qdist=qdist,epsilon=epsilon)
            tmp[i]    = zstep * (TOTAL(tmp2) - (tmp2[0]+tmp2[nstep-1])/2. )
        END
        table = [table,(TOTAL(tmp) - (tmp[0]+tmp[nstep-1])/2.)*step]
    END

    name = 'gamma_table-'+strn(fix(epsilon))+'_'+strn(fix(qdist))+'.sav'
    save, table, filename=name
end

function quad_gamma, r, Z,qdist=qdist,epsilon=epsilon

    d=qdist/2.
    spin    = [0.,1.]

    Rp = sqrt(r^2. + (z-d)^2.)
```

```
7     Rm = sqrt(r^2. + (z+d)^2.)

      rpe = rp+epsilon
      rme = rm+epsilon

12    return, r *  (9.* (r^2. + z^2. + d^2. ) * (z^2. + d^2.)  $
                    /( rpe*rme )^2.      $
                  -3.*((z+d)^2./(rme)^2.)  $
                     -3.*((z-d)^2./(rpe)^2.)  $
                  +1.)                    $
17          / ( (rp^3.+epsilon^3.)        $
              * (rm^3.+epsilon^3.) )
```

end

A.2 GADGET-2 Parameters and Tests

A.2.1 Makefile Options

```
OPT   +=  -DPERIODIC
OPT   +=  -DUNEQUALSOFTENINGS
OPT   +=  -DPMGRID=512
OPT   +=  -DPLACEHIGHRESREGION=3
OPT   +=  -DENLARGEREGION=1.2
OPT   +=  -DDOUBLEPRECISION_FFTW
OPT   +=  -DMOREPARAMS
OPT   +=  -DPEANOHILBERT
OPT   +=  -DWALLCLOCK
OPT   +=  -DALLOWEXTRAPARAMS
OPT   +=  -DAUTO_SWAP_ENDIAN_READIC
OPT   +=  -DMAGNETIC
OPT   +=  -DMAGFORCE
OPT   +=  -DMAGNETIC_SIGNALVEL
OPT   +=  -DCORRECTDB
OPT   +=  -DDIVBFORCE
OPT   +=  -DCORRECTBFRC
OPT   +=  -DBSMOOTH
OPT   +=  -DSET_FULL_STEPCOUNT
```

A.2.2 Parameter File

```
InitCondFile                /ptmp/jdonnert/Seeed/Seed_11/start_016
OutputDir                   /ptmp/jdonnert/Seeed/Seed_11
SnapshotFileBase            snap
EnergyFile                  energy.txt
```

```
InfoFile                        info.txt
TimingsFile                     timings.txt
CpuFile                         cpu.txt
RestartFile                     restart
TimeLimitCPU                    43200
ResubmitOn                      1
ResubmitCommand                 /ptmp/jdonnert/Seeed/contrun
ICFormat                        2
ComovingIntegrationOn           1
NumFilesPerSnapshot             8
NumFilesWrittenInParallel       8
SnapFormat                      2
CoolingOn                       0
TimeBegin                       0.015489947
;TimeMax                        0.27    ;Snapshot 12
;TimeMax                        0.32    ;Snapshot 14
;TimeMax                        0.39    ;Snapshot 16
TimeMax                         1.0
Omega0                          0.3
OmegaLambda                     0.7
OmegaBaryon                     0.04
HubbleParam                     0.7
BoxSize                         240000.0
PeriodicBoundariesOn            1
OutputListFilename              outputs_selection.txt
OutputListOn                    1
TimeBetSnapshot                 1.04912649189365
TimeOfFirstSnapshot             0.090909091
CpuTimeBetRestartFile           10000
TimeBetStatistics               0.02
TypeOfTimestepCriterion         0
ErrTolIntAccuracy               0.05
MaxSizeTimestep                 0.05
MinSizeTimestep                 0
MaxRMSDisplacementFac           0.5
ErrTolTheta                     0.45
TypeOfOpeningCriterion          1
ErrTolForceAcc                  0.005
TreeDomainUpdateFrequency       0.025
DesNumNgb                       64
MaxNumNgbDeviation              3
ArtBulkViscConst                0.75
InitGasTemp                     176.243
MinGasTemp                      100.
CourantFac                      0.2
PartAllocFactor                 2.0
```

```
TreeAllocFactor             0.8
BufferSize                  200
UnitLength_in_cm            3.085678e21
UnitMass_in_g               1.989e43
UnitVelocity_in_cm_per_s    1e5
GravityConstantInternal     0
MinGasHsmlFractional        0.5
SofteningGas                10.0
SofteningHalo               10.0
SofteningDisk               50.0
SofteningBulge              0
SofteningStars              0
SofteningBndry              0
SofteningGasMaxPhys         10.0
SofteningHaloMaxPhys        10.0
SofteningDiskMaxPhys        50.0
SofteningBulgeMaxPhys       0
SofteningStarsMaxPhys       0
SofteningBndryMaxPhys       0
StarformationOn             0
CritPhysDensity         0.25
MaxSfrTimescale         2.0
CritOverDensity             57.7
TempSupernova               2.0e8
TempClouds                  8000.0
FactorSN                    0.1
FactorEVP                   100.0
WindEfficiency      2.0
WindFreeTravelLength        10.0
WindEnergyFraction      0.25
WindFreeTravelDensFac       0.1
BiniX                   0.0
BiniY                   0.0
BiniZ                   1.0e-8
BSmoothInt              15
BSmoothFrac             1.0
MainTimestepCounts          21
```

A.2.3 Output List

The following table shows the physical times in terms of redshift and scale parameter, when an output of GADGET was triggered.

Snapshot	Scale Parameter (a)	Redshift (z)
0	0.090909	10.00
1	0.100061	8.99395
2	0.110133	8.07990
3	0.121220	7.24946
4	0.133423	6.49497
5	0.146854	5.80948
6	0.161637	5.18669
7	0.177909	4.62086
8	0.195818	4.10678
9	0.215530	3.63972
10	0.237227	3.21537
11	0.261108	2.82983
12	0.287393	2.47956
13	0.316324	2.16132
14	0.348167	1.87219
15	0.383215	1.60950
16	0.421792	1.37084
17	0.464253	1.15400
18	0.519373	0.92540
19	0.557942	0.79230
20	0.596267	0.67710
21	0.634598	0.57580
22	0.673083	0.48570
23	0.711845	0.40480
24	0.751033	0.33150
25	0.790639	0.26480
26	0.830910	0.20350
27	0.871840	0.14700
28	0.913668	0.0944901
29	0.956334	0.04566
30	0.999969	$3.05176 \cdot 10^{-5}$

A.2.4 Shock Tube Test Results

This shows density and velocity for the shocktube described in Chapter 3.1.3. Again the particles were binned by the half of the maximum smoothing length and the error bar resemble the 1σ standard deviation. For a more detailed investigation of the code, look forward to a paper by K.Dolag and F.Stasyszyn, to be published in the near future.

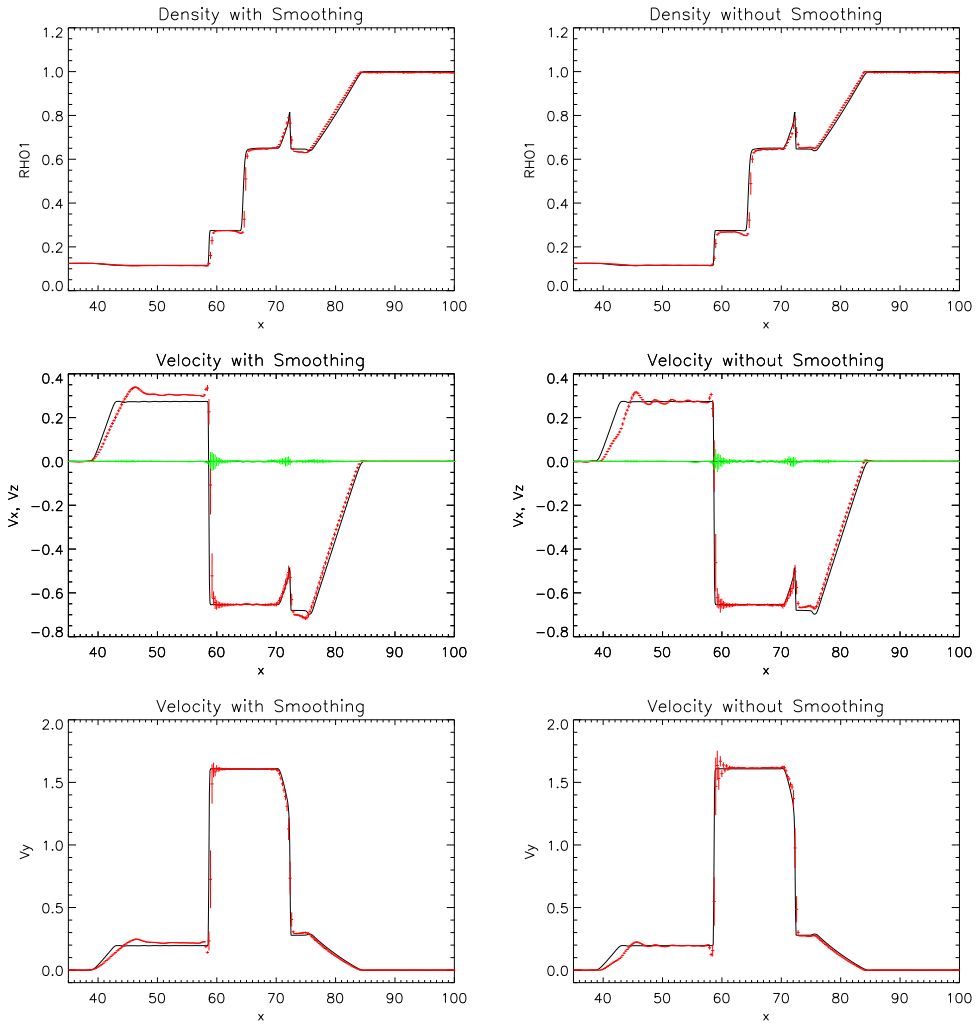

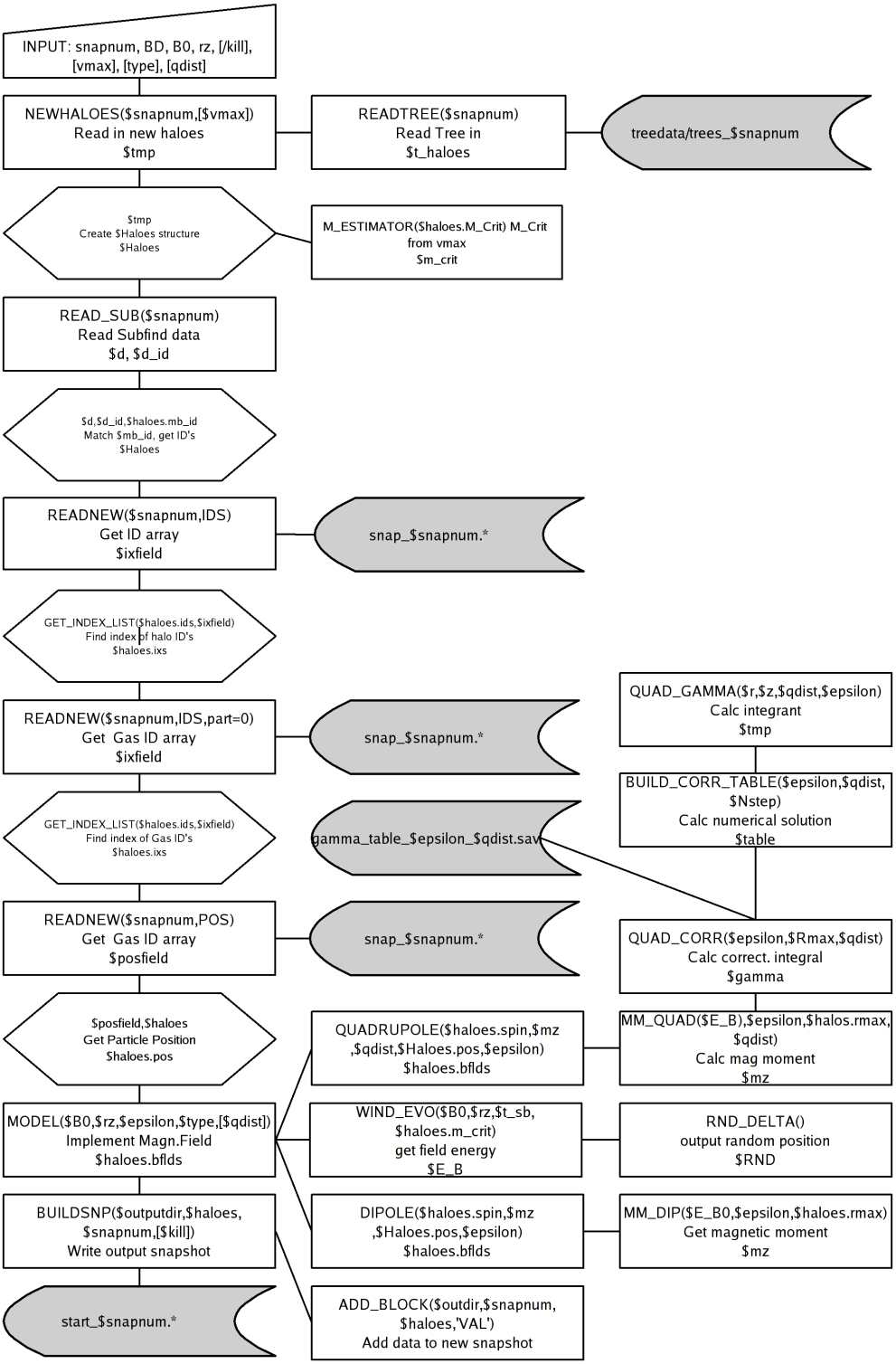

Figure A.1: Seed.pro program scheme flowchart

B Wind Model Calculations

B.1 Dipole Energy

$$E_B = \frac{1}{8\pi} \int \vec{B}^2 dV \qquad \vec{B} = \frac{1}{4\pi} \frac{3\vec{n}\,(\vec{n}\cdot\vec{m}) - \vec{m}}{|\vec{r}|} \tag{B.1}$$

To calculate the magnetic moment $\vec{m}$ of a dipole, with magnetic energy E_B, one assumes for simplicity, that $\vec{m}||\vec{e}_z$, as the moment can be aligned into any other direction by a simple rotation of the coordinate system. The unit vector $\vec{n}$ then becomes $z/|z|$ As the field $\vec{B}$ diverges for $r \to 0$ we use a softening length of $\epsilon = 10$, which corresponds to the SPH smoothing length. The outer boundary R_{max} takes the finite size of the halo

into account. With $\mu_0 = 1$ it follows:

$$
\begin{aligned}
E_B &= \frac{1}{8\pi} \int \frac{1}{(4\pi)^2} \frac{\left(3\vec{n}\left(\vec{n}\cdot\vec{m}\right) - \vec{m}\right)^2}{\left(|\vec{r}|^3 + \epsilon^3\right)^2} dV \\
&= \frac{1}{8\pi} \int \frac{1}{(4\pi)^2} \frac{1}{\left(|\vec{r}|^3 + \epsilon^3\right)^2} \cdot \left(9\vec{n}^2\left(\vec{n}\cdot\vec{m}\right)^2 - 6\vec{n}\left(\vec{n}\cdot\vec{m}\right)\vec{m} + \vec{m}^2\right) dV \\
&= \frac{1}{8\pi} \int \frac{1}{(4\pi)^2} \frac{1}{\left(|\vec{r}|^3 + \epsilon^3\right)^2} \cdot \left(3\left(\frac{z}{|\vec{r}|} m_z\right)^2 + m_z^2\right) dV \\
&= \frac{1}{8\pi\,(4\pi)^2} \iiint\limits_V \frac{r^2 \sin\phi}{\left(r^3 + \epsilon^3\right)^2} \left(3\left(\frac{r\,\cos\phi}{r} m_z\right)^2 + m_z^2\right) dr d\theta d\phi \\
&= \frac{m_z^2}{8\pi\,(4\pi)^2} \int_0^{R_{max}} \int_0^{2\pi} \int_0^{\pi} \left(\frac{3r^2 \sin\phi\,\cos^2\phi}{\left(r^3 + \epsilon^3\right)^2} + \frac{r^2 \sin\phi}{\left(r^3 + \epsilon^3\right)^2}\right) dr d\theta d\phi \\
&= \frac{m_z^2}{4\,(4\pi)^2} \cdot \left(\int_0^{R_{max}} \int_0^{\pi} \frac{3r^2}{\left(r^3 + \epsilon^3\right)^2} \cdot \sin\phi\,\cos^2\phi\, dr\, d\phi + \int_0^{R_{max}} \int_0^{\pi} \frac{r^2}{\left(r^3 + \epsilon^3\right)^2} \cdot \sin\phi\, dr\, d\phi\right) \\
&= \frac{m_z^2}{4\,(4\pi)^2} \left(\int_0^{R_{max}} \frac{3r^2}{\left(r^3 + \epsilon^3\right)^2} \cdot \left(-\frac{\cos\phi}{4} - \frac{\cos 3\phi}{12}\right)\Bigg|_0^{\pi} dr + \int_0^{R_{max}} \frac{r^2}{\left(r^3 + \epsilon^3\right)^2} \left(-\cos\phi\right)\Bigg|_0^{\pi} dr\right) \\
&= \frac{4m_z^2}{4\,(4\pi)^2} \int_0^{R_{max}} \frac{r^2}{\left(r^3 + \epsilon^3\right)^2} dr \qquad \text{with } \xi = r^3 + \epsilon^3 \Rightarrow \frac{d\xi}{dr} = 3r^2 \\
&= \frac{m_z^2}{(4\pi)^2} \int_{\epsilon^3}^{R_{max}^3 + \epsilon^3} \frac{r^2}{3r^2} \frac{1}{\xi^2} d\xi \\
&= -\frac{m_z^2}{3\,(4\pi)^2} \cdot \frac{1}{\xi}\Bigg|_{\epsilon^3}^{R_{max}^3 + \epsilon^3} \\
&= \frac{m_z^2}{3\,(4\pi)^2} \cdot \left(\frac{1}{\epsilon^3} - \frac{1}{R_{max}^3 + \epsilon^3}\right)
\end{aligned}
$$

where i used spherical coordinates in step 3. It follows:

$$
\boxed{m_z = \sqrt{48\pi^2 E_B \cdot \left(\frac{1}{\epsilon^3} - \frac{1}{R_{max}^3 + \epsilon^3}\right)^{-1}}} \tag{B.2}
$$

B.2 Quadrupole Energy

Canonically a quadrupole is parametrised by the quadrupole tensor, which in the case of magnetic field consists of 3 trace-free, symmetric 3x3 Matrizes. The tensor itself is defined by the current density $\vec{j}$, which in our case are two ring current 'around' the spin axis. This would lead to 15 components for tensor, while for this case of high symmetry 4 parameters are enough. An other way is to constitute the quadrupole by superposition of 2 dipols at a distance d, with dipole moments $\vec{m}_1 = m_z\vec{s}$ and $\vec{m}_2 = m_z\,(-\vec{s})$, 'pointing' to opposite directions. Introducing a softening length ϵ the field is given by :

$$\vec{B} = \vec{B}_+^{DIP} + \vec{B}_-^{DIP} \tag{B.3}$$

According to B.1 it follows for the field energy, as the direction of the dipol moment $\vec{m}$ is not relevant for the energy contain in its field :

$$\begin{aligned} E_B &= \frac{1}{8\pi}\int \vec{B}^2\,dV = \frac{1}{8\pi}\int \left(\vec{B}_+^{DIP} + \vec{B}_-^{DIP}\right)^2 dV \\ &= \frac{1}{8\pi}\int \vec{B}_+^2\,dV + \frac{1}{8\pi}\int \vec{B}_-^2\,dV + \frac{2}{8\pi}\int \vec{B}_+\vec{B}_-\,dV \\ &= \frac{2}{8\pi}\int \vec{B}^2\,dV + \frac{2}{8\pi}\int \vec{B}_+\vec{B}_-\,dV \end{aligned}$$

We define :

$$\vec{r}_\pm = \vec{r} \mp \frac{d}{2}\,\vec{s} \qquad r_\pm = |\vec{r}_\pm| \qquad \vec{n}_\pm = \frac{\vec{r}_\pm}{r_\pm}$$
$$n_\pm^z = \vec{n}_\pm \cdot \vec{e}_z \qquad \vec{m}_\pm = \pm m_z\vec{s}$$

In the further considerations, I assume $\vec{s} \parallel \vec{e}_z$ for simplicity. As the dipole field energy is known to be 4.6 this leaves us with calculating the mixed term :

$$\begin{aligned} E_B &= \frac{2m_z^2}{48\pi^2}\left(\frac{1}{\epsilon^3} - \frac{1}{R_{max}^3 + \epsilon^3}\right) + \frac{-2m_z^2}{8\pi(4\pi)^2}\cdot\int dV\,\frac{3\vec{n}_+\,(\vec{n}_+\vec{e}_z) - \vec{e}_z}{r_+^3 + \epsilon^3}\cdot\frac{3\vec{n}_-\,(\vec{n}_-\vec{e}_z) - \vec{e}_z}{r_-^3 + \epsilon^3} \\ &= \frac{2m_z^2}{48\pi^2}\alpha + \frac{-2m_z^2}{8\pi(4\pi)^2}\cdot\gamma \end{aligned}$$

where the magnetic moment was allready pulled out of the integral[1]. Multiplying the fractions :

$$\gamma = \int \frac{9\,(\vec{n}_+\vec{n}_-)\,n_+^z n_-^z - 3(\vec{n}_+^z)^2 - 3(\vec{n}_-^z)^2 + 1}{\left(r_+^3 + \epsilon^3\right)\left(r_-^3 + \epsilon^3\right)}\,dV$$

[1] Note that we pulled out m_z from the $+$ and $-m_z$ from the - term

The quadrupole field shows rotational symmetry around the z-axis, so one integral can easily be done, transforming to cylindrical coordinates. Further the current configuration is symmetric for positive and negative z values. We integrate over a sphere, so i set $\delta = \sqrt{R_{max}^2 - r^2}$:

$$\begin{aligned}
\gamma &= \int_0^{\delta} dz \int_0^{2\pi} d\phi \int_{-R_{max}}^{R_{max}} r\,dr\, \frac{9\left(r^2+z^2+d^2\right)\frac{(z-d)(z+d)}{(r_+ +\epsilon)^2(r_- +\epsilon)^2}}{\left(r_+^3+\epsilon^3\right)\left(r_-^3+\epsilon^3\right)} \\
&+ \int_0^{\delta} dz \int_0^{2\pi} d\phi \int_{-R_{max}}^{R_{max}} r\,dr\, \frac{-3\frac{(z-d)^2}{(r_+ +\epsilon)^2} - 3\frac{(z-d)^2}{(r_+ +\epsilon)^2} + 1}{\left(r_+^3+\epsilon^3\right)\left(r_-^3+\epsilon^3\right)} \\
&= 4\pi \cdot \int_0^{\delta} dz \int_0^{R_{max}} r dr\, \frac{9\left(r^2+z^2+d^2\right)\frac{z^2+d^2}{(r_+ +\epsilon)^2(r_- +\epsilon)^2}}{\left(r_+^3+\epsilon^3\right)\left(r_-^3+\epsilon^3\right)} \\
&+ 4\pi \cdot \int_0^{\delta} dz \int_0^{R_{max}} r dr\, \frac{-3\frac{(z-d)^2}{(r_+ +\epsilon)^2} - 3\frac{(z-d)^2}{(r_+ +\epsilon)^2} + 1}{\left(r_+^3+\epsilon^3\right)\left(r_-^3+\epsilon^3\right)}
\end{aligned}$$

This becomes equal to 4.6 for $d \to 0$ and $\epsilon \to 0$, which is expected: The magnetic moment should diverge for non-zero field energy, as there is no current and therefore no field for a distance of zero. For a finite softening length, this isn't true anymore, still the value should reach its maximum value for $d = 0$.
For $d \to \infty$ the moments are not interacting at all, so the moments are the same as for the dipol case, except a factor of 0.5.

As this integral is solved numerically, the solution needs to show the behaviour described above, which is indeed the case. I used a trapezium rule for integration, the behaviour of the solution with respect to d is shown in B.2. Besides a plot of the integrant , which is strongly peaked at the position of the moment and smeared out by epsilon, is shown.

B.3 Solution of the Wind Equation

The differential equation to solve given from [BVE06] is:

$$\frac{d}{dt}E_B(t) = \dot{E}_{B_{in}} - \frac{1}{3}\frac{\dot{V}_W(t)}{V_W(t)}E_B(t) \tag{B.4}$$

The volume of an expanding sphere gives the time dependence :

$$V_W = \frac{4\pi}{3} \cdot R(t)^3 = \frac{4\pi}{3} v_W^3 \cdot t^3$$
$$\Rightarrow \dot{V}_W = \frac{4\pi}{3} \cdot v_W^3 t^2$$

It follows:

$$\frac{d}{dt} E_B(t) = \dot{E}_{B_{in}} - \frac{1}{t} E_B$$

which can be solved by using the standard formula for inhomogeneous, ordinatry differential equation of first order:

$$E(t) = \exp(-\ln t) \left[\int \dot{E}_{B_{in}} \exp(\ln t) + E(0) \right] \tag{B.5}$$
$$= \frac{1}{t} \left[\frac{t^2}{2} \dot{E}_{B_{in}} + E(0) \right] \tag{B.6}$$
$$= \frac{t}{2} \dot{E}_{B_{in}} + \frac{1}{t} E(0) \tag{B.7}$$

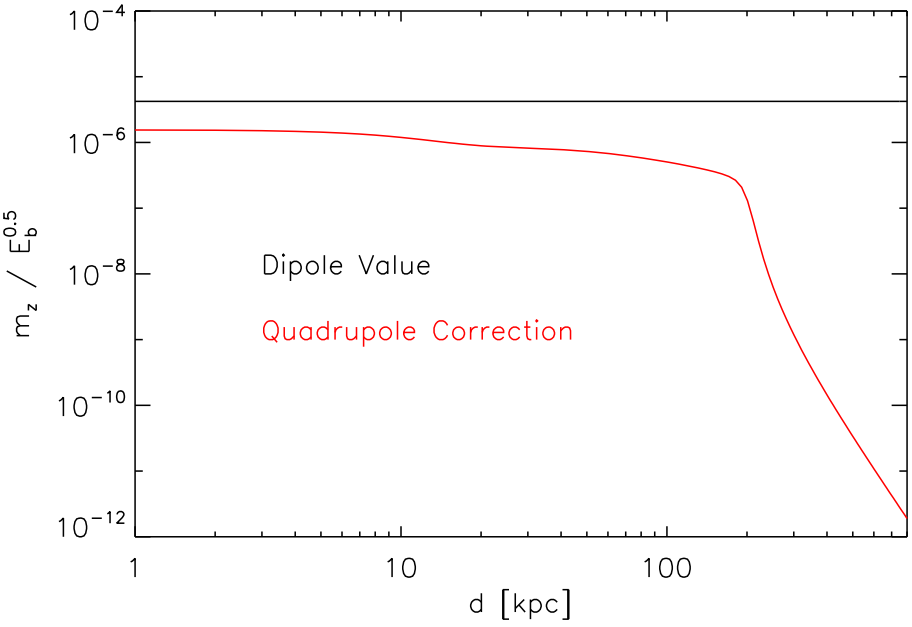

Figure B.1: γ,i.e. quadrupole correction over distance of the dipole moments

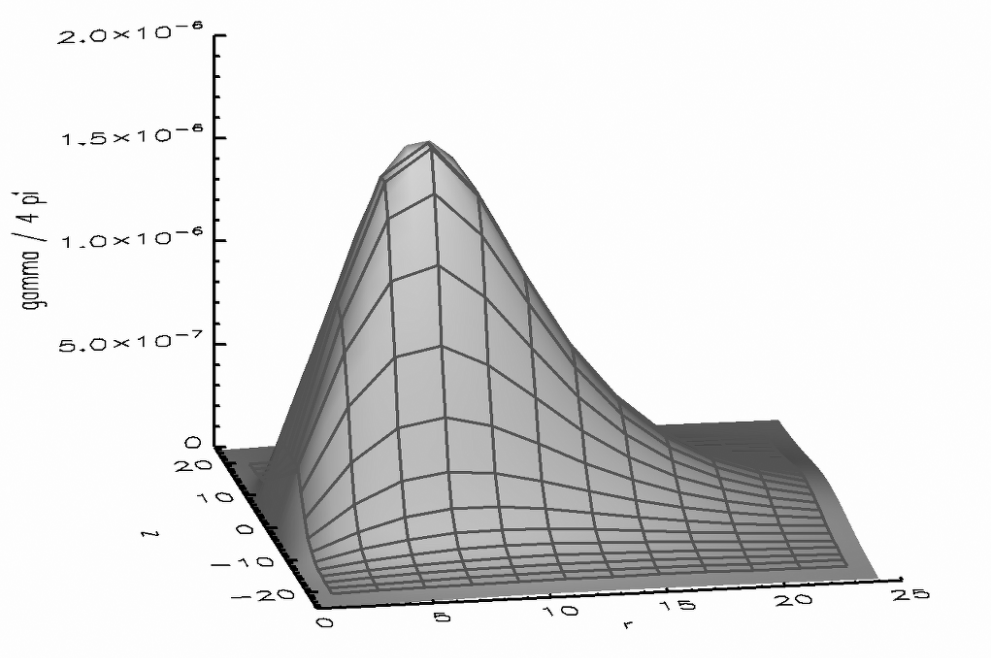

Figure B.2: Integrant plotted for $\epsilon = d = 10$, Note that the individual moments are smoothed out be ϵ

C Additional Physics Of Interest

C.1 Cosmic Rays In Galaxy Clusters

In several places in this work, we make use of the fact, that many galaxy(clusters) like M87 (Coma) contain radio haloes, with non thermal spectrum. In 2.4.1 we describe how the magnetic field in the IGM / ICM can be measured with a relativistic population of electrons, assuming a powerlaw spectrum in energy distribution. In 6.2.4 we show how our simulated clusters would look like, assuming they were radio loud clusters with an population of relativistic particles from secondary models.

It is believed, that several sources contribute to the origin of ICM electrons. AGN are an obvious source of relativistic particles, as well as supernova winds. The superbubbles formed from their ejecta will not only seed magnetic fields in to the cluster, but cosmic rays as well. Shocks from cluster mergers play an important as well: they reaccelerate CRs locally by Fermi acceleration to form radio relics, widely observed.

The origin of diffuse radio haloes in clusters is still under debate. The problem emerges, when one compares the CR lifetime with their crossing time in those clusters. As aboves sources produces relativistic particles only locally, a diffuse halo, requires the lifetime to be significantly larger than the crossing time. But due to synchroton losses and scattering, the lifetime of CR electrons is much smaller than their crossing time. To produce a diffuse radio haloes, the electron must be reaccelerated/produced continuously/locally.

As the lifetime of CR protons is about a Hubble time in clusters, one way to solve this problem is the production of pions in collisions of relativistic protons with termal nuclei. $\pi^{\pm}$ decay to $\mu^{\pm}$ which end up in $e^{\pm}$ This model predicts, that every cluster should have a radio halo, which is not observed [PE04].
Another possiblity around the problem might be MHD turbulence from diffuse shocks. Small scale turbulence might reaccelerate the electrons on a global scale, dependend on the merger history of the cluster.

C.2 Faraday Rotation

When electromagnetic radiation passes a medium containing free charges, the interaction between those charges and the wave results in a change of permeability ϵ. In the case of

the Faraday effect, the material constants depend on the phase direction of the waves amplitude, e.g. they become complex.

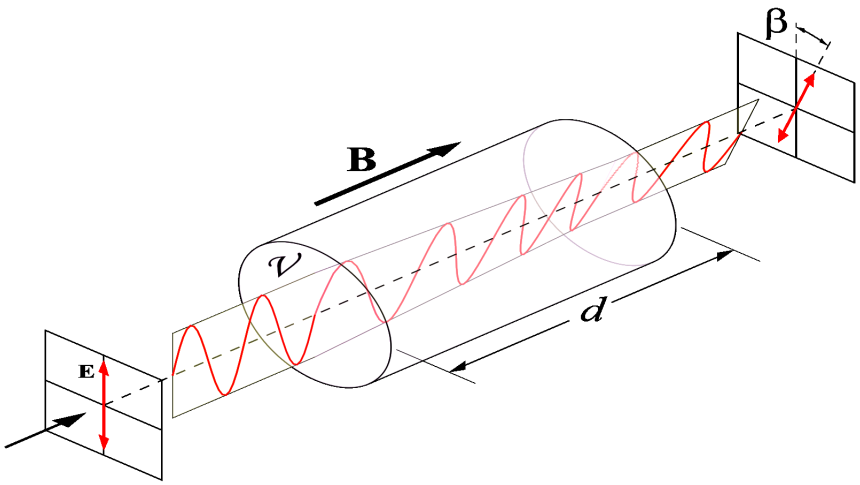

Figure C.1: About Faraday Rotation [Wik07a]

To explain this behaviour it is necessary to look at the interaction of the electric/-magnetic field of the wave and the free charges, in our case electrons. Considering a classical approach with magnetic field $\vec{B}_0$ and E-M wave in z direction, the equation of motion for an electron reads:

$$m_e \frac{\mathrm{d}\vec{r}}{\mathrm{dt}} = -e\left(\vec{E} + \vec{v} \times \vec{B}_0\right) \tag{C.1}$$

where the first term on the right hand side, describes the interaction between wave and electron. The last term resembles the lorentz force from the constant magnetic field acting on the electron. The electromagnetic wave follows the usual wave equation :

$$\nabla^2 \vec{E} + \epsilon\mu \frac{\partial^2}{\partial t^2} \vec{E} = 0 \tag{C.2}$$

with $\vec{E} \perp B_0$. The same accounts for the B field component of the radiation, which i don't treat here seperately[1].

To study the electrons response to an infalling radiation field, i consider an infalling linear polarized electromagnetic wave with a frequency ω. This is commonly written as a superposition of two circular polarized waves, with opposite direction of rotation:

$$\begin{aligned} \vec{E} &= \vec{E}_{circ,+} + \vec{E}_{circ,-} \\ &= E_0 \left(\vec{e}_+ \cdot e^{i(k_+ z - \omega t)} + \vec{e}_- \cdot e^{i(k_- z - \omega t)}\right) \end{aligned}$$

[1] Because of : $\vec{B} = \sqrt{\mu\epsilon}\frac{\vec{k}\times\vec{E}}{k}$

with $\vec{e}_\pm = \frac{1}{2}(\vec{e}_x \pm i\vec{e}_y)$ defining the direction of rotation, $k_\pm$ the wave vector, and E_0 the common amplitude of both waves.
From the interaction with the infalling wave, the electrons will be pertubed from their trajectory and be forced on circular motion around the fieldlines. The pertubation acts in the x-y plane, proportional to the infalling wave amplitude $\delta r \propto \binom{x}{y} e^{i\omega t}$. It follows for C.1:

$$m_e\omega^2 x = e\,(E_x - i\omega B_0 y) \tag{C.3}$$
$$m_e\omega^2 y = e\,(E_y - i\omega B_0 x) \tag{C.4}$$

As we treat the wave amplitude complex, we write the pertubation vector as a complex number $d_\pm = x \pm iy$. The two different amplitudes correspond to different directions of circular motion of the electrons:

$$\vec{\delta r} = d_+\vec{e}_+ \cdot e^{i(k_+ z - \omega t)} + d_-\vec{e}_- \cdot e^{i(k_- z - \omega t)}$$

And we obtain for the equation of motion of the electrons :

$$d_\pm = \frac{eE_\pm}{m_e\omega\,(\omega \pm \Omega)}$$

where $\Omega = \frac{eB_0}{m_e}$ is the cyclotron frequency, the caracteristic frequency, electrons oscillate around the fieldline with.

The motion of the electron leads to an effective dipole moment, as a charge displacement in an otherwise homogeneous, uncharged medium takes place. In first order, the polarisation is defined as the sum of all dipole moments in a dielectric medium and is connected to the electric field by

$$\vec{P} = \epsilon_0\,(\epsilon - 1)\,\vec{E}$$

Inducing dipole moments in a medium, therefore leads to a change in the dielectric constant. Naively spoken, the absorption and reemitation of the E-M wave takes time, and therefore changes the speed of the wave in the medium. Similar to the Lorentz oscillator model for dielectric media, the changed dielectric constant is :

$$\epsilon_\pm = 1 - \frac{\omega_p}{\omega\,(\omega \pm \Omega)}$$

with $\omega_p = \frac{n_e e^2}{\epsilon_0 m_e}$ being the plasma frequency. With the wave equation C.2 the dispersion relation for the wave becomes :

$$k_\pm^2 c^2 = \omega^2 \cdot \left(1 - \frac{w_p^2}{\omega\,(\omega \pm \Omega)}\right)$$

which in the limit of $\omega \ll \omega_p, \Omega$ means : $k_\pm \approx k \pm \Delta k$ with $k = \omega - \frac{\omega_p^2 \omega}{2\omega}$ and $\Delta k = \frac{\omega_p}{2\omega^2} \cdot \frac{\Omega}{c}$ This can be understood by considering, that the forced motion on the electron by the infalling wave acts either in the direction or against the direction of the 'natural motion' of the electrons around the magnetic field lines. The dispersion relation / light speed / permittivity / wave vector is therefore depending on the helicity of the infalling wave.

For a linear polarized wave, which is constituated by two circular polarized waves rotating in opposite directions, the slowing of one phase and acceleration of the other phase results in a shift in polarization angle. The magnetic field breaks the symmetry of the system, prefering one orientation over the other.

With $k_\pm \approx k \pm \Delta k$ the real part of the electric field, representing the actual measured field strength, can be written as[2]:

$$\vec{E} = E_0 \begin{pmatrix} \cos(kz - \omega t)\cos(\Delta k z) \\ \cos(kz - \omega t)\sin(\Delta k z) \\ 0 \end{pmatrix}$$

Refering to Figure C.1, the angle of rotation can then be calculated :

$$\begin{aligned} \beta &= \tan^{-1}\left(\frac{E_x}{E_y}\right) \\ &= \Delta k z \end{aligned}$$

For a column of plasma of length d, with electron number density n_e we have to integrate $\frac{d\beta}{dz} = \Delta k$:

$$\begin{aligned} \beta &= \int_0^d \Delta k dz \\ &= \int_0^d \frac{\omega_p \Omega}{2\omega^2 c} dz = \frac{e^3}{2\epsilon_0 m_e^2} \frac{1}{\omega^2} \int_0^d n_e B(z)\, dz \end{aligned}$$

[2] using: $\sin\alpha \sin\beta = \frac{1}{2}[\cos(\alpha-\beta) - \cos(\alpha+\beta)]$ and $\cos\alpha\cos\beta = \frac{1}{2}[\cos(\alpha-\beta) + \cos(\alpha+\beta)]$

Bibliography

[Bec02] R. Beck. *in The astrophysics of galactic cosmic rays (Proceedings) (Space sciences series of ISSI, vol. 13)*. Kluwer, Dortrecht, The Netherlands, 2002.

[BHH+03] C. L. Bennett, M. Halpern, G. Hinshaw, N. Jarosik, A. Kogut, M. Limon, S. S. Meyer, L. Page, D. N. Spergel, G. S. Tucker, E. Wollack, E. L. Wright, C. Barnes, M. R. Greason, R. S. Hill, E. Komatsu, M. R. Nolta, N. Odegard, H. V. Peiris, L. Verde, and J. L. Weiland. First-Year Wilkinson Microwave Anisotropy Probe (WMAP) Observations: Preliminary Maps and Basic Results. ApJS, 148:1–27, September 2003.

[BK05] R. Beck and M. Krause. Revised equipartition and minimum energy formula for magnetic field strength estimates from radio synchrotron observations. *Astronomische Nachrichten*, 326:414–427, July 2005.

[BL00] E. Battaner and H. Lesch. On the Physics of Primordial Magnetic Fields. *ArXiv Astrophysics e-prints*, March 2000.

[BVE06] S. Bertone, C. Vogt, and T. Enßlin. Magnetic field seeding by galactic winds. MNRAS, 370:319–330, July 2006.

[BWLK00] G. T. Birk, H. Wiechen, H. Lesch, and P. P. Kronberg. The role of Kelvin-Helmholtz modes in superwinds of primeval galaxies for the magnetization of the intergalactic medium. A&A, 353:108–116, January 2000.

[BWO99] G. T. Birk, H. Wiechen, and A. Otto. Magnetic Field Amplification in M82 Winds Caused by Kelvin-Helmholtz Modes. ApJ, 518:177–182, June 1999.

[CB04] K. T. Chyzy and R. Beck. Magnetic Fields in Strongly Interacting Galaxy Systems. In P.-A. Duc, J. Braine, and E. Brinks, editors, *Recycling Intergalactic and Interstellar Matter*, volume 217 of *IAU Symposium*, pages 436–+, June 2004.

[CBG+06] D. Clowe, M. Bradač, A. H. Gonzalez, M. Markevitch, S. W. Randall, C. Jones, and D. Zaritsky. A Direct Empirical Proof of the Existence of Dark Matter. ApJ, 648:L109–L113, September 2006.

[CKB01] T. E. Clarke, P. P. Kronberg, and H. Böhringer. A New Radio-X-Ray Probe of Galaxy Cluster Magnetic Fields. ApJ, 547:L111–L114, February 2001.

[CT02] C. L. Carilli and G. B. Taylor. Cluster Magnetic Fields. ARA&A, 40:319–348, 2002.

[Dat07] NASA Extragalactic Database. The extragalactic database, 2007.

[de 01] R. de Grijs. Star formation time-scales in the nearby, prototype starburst galaxy M82. *ArXiv Astrophysics e-prints*, June 2001.

[DGST05] K. Dolag, D. Grasso, V. Springel, and I. Tkachev. Constrained simulations of the magnetic field in the local Universe and the propagation of ultrahigh energy cosmic rays. *Journal of Cosmology and Astro-Particle Physics*, 1:9–+, January 2005.

[DS84] J. M. Dickey and E. E. Salpeter. 1.4 GHz continuum sources in the Hercules cluster. ApJ, 284:461–470, September 1984.

[FA93] A. J. Fitt and P. Alexander. Magnetic fields in late-type galaxies. MNRAS, 261:445–452, March 1993.

[Fer92] K. Ferriere. Effect of the explosion of supernovae and superbubbles on the Galactic dynamo. ApJ, 391:188–198, May 1992.

[FHS+95] K. B. Fisher, J. P. Huchra, M. A. Strauss, M. Davis, A. Yahil, and D. Schlegel. The IRAS 1.2 Jy Survey: Redshift Data. ApJS, 100:69–+, September 1995.

[FL01] S. R. Furlanetto and A. Loeb. Intergalactic Magnetic Fields from Quasar Outflows. ApJ, 556:619–634, August 2001.

[GM77] R. A. Gingold and J. J. Monaghan. Smoothed particle hydrodynamics - Theory and application to non-spherical stars. MNRAS, 181:375–389, November 1977.

[Goo03] M. Goossens. *An Introduction to Plasma Astrophysics and Magnetohydrodynamics*. Kluwer Academic Publishers, 2003.

[Gre97] E. K. Grebel. Old Stellar Populations in Local Group Dwarf Galaxies. In *Bulletin of the American Astronomical Society*, volume 29 of *Bulletin of the American Astronomical Society*, pages 825–+, May 1997.

[GS65] V. L. Ginzburg and S. I. Syrovatskii. Cosmic Magnetobremsstrahlung (synchrotron Radiation). ARA&A, 3:297–+, 1965.

[HBD91] E. Hummel, R. Beck, and M. Dahlem. The magnetic field structure in the radio halos of NGC 891 and NGC 4631. A&A, 248:23–29, August 1991.

[HD02] W. Hu and S. Dodelson. Cosmic Microwave Background Anisotropies. ARA&A, 40:171–216, 2002.

[HK97] A. M. Howard and R. M. Kulsrud. The Evolution of a Primordial Galactic Magnetic Field. ApJ, 483:648–+, July 1997.

[HM05] W. Hillebrandt and Muller.E. Hydrodynamik: Grundlagen und numerische Verfahren. June 2005.

[Hub29] E. Hubble. A Relation between Distance and Radial Velocity among Extra-Galactic Nebulae. *Proceedings of the National Academy of Science*, 15:168–173, March 1929.

[Jon00] T. J. Jones. The Magnetic Field Geometry in M82 and Centaurus A. AJ, 120:2920–2927, December 2000.

[Jon07] T. W. Jones. The Role of MHD in the ICM and its Interactions with AGN Outflows. *ArXiv e-prints*, 708, August 2007.

[KCOR97] R. M. Kulsrud, R. Cen, J. P. Ostriker, and D. Ryu. The Protogalactic Origin for Cosmic Magnetic Fields. ApJ, 480:481–+, May 1997.

[KKT91] K.-T. Kim, P. P. Kronberg, and P. C. Tribble. Detection of excess rotation measure due to intracluster magnetic fields in clusters of galaxies. ApJ, 379:80–88, September 1991.

[KLH99] P. P. Kronberg, H. Lesch, and U. Hopp. Magnetization of the Intergalactic Medium by Primeval Galaxies. ApJ, 511:56–64, January 1999.

[KWM88] U. Klein, R. Wielebinski, and H. W. Morsi. Radio continuum observations of M82. A&A, 190:41–46, January 1988.

[KZ07] R. M. Kulsrud and E. G. Zweibel. The Origin of Astrophysical Magnetic Fields. *ArXiv e-prints*, 707, July 2007.

[MCC+94] J. C. Mather, E. S. Cheng, D. A. Cottingham, R. E. Eplee, Jr., D. J. Fixsen, T. Hewagama, R. B. Isaacman, K. A. Jensen, S. S. Meyer, P. D. Noerdlinger, S. M. Read, L. P. Rosen, R. A. Shafer, E. L. Wright, C. L. Bennett, N. W. Boggess, M. G. Hauser, T. Kelsall, S. H. Moseley, Jr., R. F. Silverberg, G. F. Smoot, R. Weiss, and D. T. Wilkinson. Measurement of the cosmic microwave background spectrum by the COBE FIRAS instrument. ApJ, 420:439–444, January 1994.

[MGF+04] M. Murgia, F. Govoni, L. Feretti, G. Giovannini, D. Dallacasa, R. Fanti, G. B. Taylor, and K. Dolag. Magnetic fields and Faraday rotation in clusters of galaxies. A&A, 424:429–446, September 2004.

[MLS+02] H. Mathis, G. Lemson, V. Springel, G. Kauffmann, S. D. M. White, A. Eldar, and A. Dekel. Simulating the formation of the local galaxy population. MNRAS, 333:739–762, July 2002.

[NFW96] J. F. Navarro, C. S. Frenk, and S. D. M. White. The Structure of Cold Dark Matter Halos. ApJ, 462:563–+, May 1996.

[PE04] C. Pfrommer and T. A. Enßlin. Constraining the population of cosmic ray protons in cooling flow clusters with γ-ray and radio observations: Are radio mini-halos of hadronic origin? A&A, 413:17–36, January 2004.

[PS03] S. Perlmutter and B. P. Schmidt. Measuring Cosmology with Supernovae. In K. Weiler, editor, *Supernovae and Gamma-Ray Bursters*, volume 598 of *Lecture Notes in Physics, Berlin Springer Verlag*, pages 195–217, 2003.

[RFC+98] A. G. Riess, A. V. Filippenko, P. Challis, A. Clocchiatti, A. Diercks, P. M. Garnavich, R. L. Gilliland, C. J. Hogan, S. Jha, R. P. Kirshner, B. Leibundgut, M. M. Phillips, D. Reiss, B. P. Schmidt, R. A. Schommer, R. C. Smith, J. Spyromilio, C. Stubbs, N. B. Suntzeff, and J. Tonry. Observational Evidence from Supernovae for an Accelerating Universe and a Cosmological Constant. AJ, 116:1009–1038, September 1998.

[RJ95] D. Ryu and T. W. Jones. Numerical magetohydrodynamics in astrophysics: Algorithm and tests for one-dimensional flow‘. ApJ, 442:228–258, March 1995.

[RKL+92] H.-P. Reuter, U. Klein, H. Lesch, R. Wielebinski, and P. P. Kronberg. Gaps and filaments in the synchrotron halo of M82 - Evidence for poloidal magnetic fields. A&A, 256:10–18, March 1992.

[RKL+94] H.-P. Reuter, U. Klein, H. Lesch, R. Wielebinski, and P. P. Kronberg. The magnetic field in the halo of M 82. Polarized radio emission at lambda-lambda(6.2) and 3.6 CM. A&A, 282:724–730, February 1994.

[RW75] M. S. Roberts and R. N. Whitehurst. The rotation curve and geometry of M31 at large galactocentric distances. ApJ, 201:327–346, October 1975.

[Sah05] V. Sahni. Dark Matter and Dark Energy. In K. Tamvakis, editor, *The Physics of the Early Universe*, volume 653 of *Lecture Notes in Physics, Berlin Springer Verlag*, pages 141–+, 2005.

[SH02] V. Springel and L. Hernquist. Cosmological smoothed particle hydrodynamics simulations: the entropy equation. MNRAS, 333:649–664, July 2002.

[SMS05] C.-G. Shu, H.-J. Mo, and Shu-DeMao. An Analytic Model of Galactic Winds and Mass Outflows. *Chinese Journal of Astronomy and Astrophysics*, 5:327–346, August 2005.

[Spr05] V. Springel. The cosmological simulation code GADGET-2. MNRAS, 364:1105–1134, December 2005.

[SUB+01] M. Soida, M. Urbanik, R. Beck, R. Wielebinski, and C. Balkowski. Unusual magnetic fields in the interacting spiral NGC 3627. A&A, 378:40–50, October 2001.

[SVP+03] D. N. Spergel, L. Verde, H. V. Peiris, E. Komatsu, M. R. Nolta, C. L. Bennett, M. Halpern, G. Hinshaw, N. Jarosik, A. Kogut, M. Limon, S. S. Meyer, L. Page, G. S. Tucker, J. L. Weiland, E. Wollack, and E. L. Wright. First-Year Wilkinson Microwave Anisotropy Probe (WMAP) Observations: Determination of Cosmological Parameters. ApJS, 148:175–194, September 2003.

[SWTK01] V. Springel, S. D. M. White, G. Tormen, and G. Kauffmann. Populating a cluster of galaxies - I. Results at [formmu2]z=0. MNRAS, 328:726–750, December 2001.

[SYW01] V. Springel, N. Yoshida, and S. D. M. White. GADGET: a code for collisionless and gasdynamical cosmological simulations. *New Astronomy*, 6:79–117, April 2001.

[TBS+04] M. Tegmark, M. R. Blanton, M. A. Strauss, F. Hoyle, D. Schlegel, R. Scoccimarro, M. S. Vogeley, D. H. Weinberg, I. Zehavi, A. Berlind, T. Budavari, A. Connolly, D. J. Eisenstein, D. Finkbeiner, J. A. Frieman, J. E. Gunn, A. J. S. Hamilton, L. Hui, B. Jain, D. Johnston, S. Kent, H. Lin, R. Nakajima, R. C. Nichol, J. P. Ostriker, A. Pope, R. Scranton, U. Seljak, R. K. Sheth, A. Stebbins, A. S. Szalay, I. Szapudi, L. Verde, Y. Xu, J. Annis, N. A. Bahcall, J. Brinkmann, S. Burles, F. J. Castander, I. Csabai, J. Loveday, M. Doi, M. Fukugita, J. R. I. Gott, G. Hennessy, D. W. Hogg, Ž. Ivezić, G. R. Knapp, D. Q. Lamb, B. C. Lee, R. H. Lupton, T. A. McKay, P. Kunszt, J. A. Munn, L. O'Connell, J. Peoples, J. R. Pier, M. Richmond, C. Rockosi, D. P. Schneider, C. Stoughton, D. L. Tucker, D. E. Vanden Berk, B. Yanny, and D. G. York. The Three-Dimensional Power Spectrum of Galaxies from the Sloan Digital Sky Survey. ApJ, 606:702–740, May 2004.

[TDS+00] R. Tüllmann, R.-J. Dettmar, M. Soida, M. Urbanik, and J. Rossa. The thermal and non-thermal gaseous halo of NGC 5775. A&A, 364:L36–L41, December 2000.

[TFB96] D. Tytler, X.-M. Fan, and S. Burles. Cosmological baryon density derived from the deuterium abundance at redshift z = 3.57. Nature, 381:207–209, May 1996.

[TKW03] M. Thierbach, U. Klein, and R. Wielebinski. The diffuse radio emission from the Coma cluster at 2.675 GHz and 4.85 GHz. A&A, 397:53–61, January 2003.

[VE05] C. Vogt and T. A. Enßlin. A Bayesian view on Faraday rotation maps Seeing the magnetic power spectra in galaxy clusters. A&A, 434:67–76, April 2005.

[Wid02] L. M. Widrow. Origin of galactic and extragalactic magnetic fields. *Reviews of Modern Physics*, 74:775–823, 2002.

[Wik07a] Wikipedia. Faraday rotation — Wikipedia, the free encyclopedia, 2007. [Online; accessed 02-May-2007].

[Wik07b] Wikipedia. Shape of the universe — wikipedia, the free encyclopedia, 2007. [Online; accessed 19-July-2007].

[Zwi33] F. Zwicky. Die Rotverschiebung von extragalaktischen Nebeln. *Helvetica Physica Acta*, 6:110–127, 1933.